NASA TECHNICAL MEMORANDUM

NASA TM 75,023

INVESTIGATIONS OF PRIMARY AND SECONDARY IMPACT STRUCTURES ON THE MOON AND LABORATORY EXPERIMENTS TO STUDY THE EJECTA OF SECONDARY PARTICLES

Beate König

Translation of "Untersuchung von Primaren und Sekundären Einschlagstrukturen auf dem Mond und Laborexperimente zum Studium des Auswurfs von Sekundärteilchen", PHD Doctoral Dissertation, Ruprecht Karl University, Heidelberg, West Germany, Published by Beate Koenig, Potsdam, 1977, 88 pages.

(NASA-TM-75023) INVESTIGATIONS OF PRIMARY AND SECONDARY IMPACT STRUCTURES ON THE MOON AND LABORATORY EXPERIMENTS TO STUDY THE EJECTA OF SECONDARY PARTICLES Ph.D. Thesis - Ruprecht Karl (Scientific Translation

N77-29042

HC A06/MF A01

Unclas

G3/91 36808

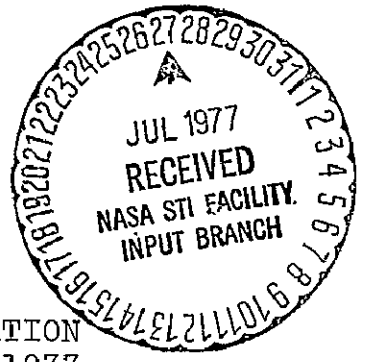

NATIONAL AERONAUTICS AND SPACE ADMINISTRATION
WASHINGTON, D.C. 20546

JULY 1977

STANDARD TITLE PAGE

1. Report No. NASA TM 75,023	2. Government Accession No.	3. Recipient's Catalog No.
4. Title and Subtitle INVESTIGATIONS OF PRIMARY AND SECONDARY IMPACT STRUCTURES ON THE MOON AND LABORATORY EXPERIMENTS TO STUDY THE EJECTA OF SECONDARY PARTICLES		5. Report Date July 1977 6. Performing Organization Code
7. Author(s) Beate König		8. Performing Organization Report No. 10. Work Unit No.
9. Performing Organization Name and Address SCITRAN Box 5456 Santa Barbara, CA 93108		11. Contract or Grant No. NASw-2791 13. Type of Report and Period Covered Translation
12. Sponsoring Agency Name and Address National Aeronautics and Space Administration Washington, D.C. 20546		14. Sponsoring Agency Code

15. Supplementary Notes

Translation of "Untersuchung von Primaren und Sekundären Einschlag-strukturen auf dem Mond und Laborexperimente zum Studium des Auswurfs von Sekündärteilchen", PHD Doctoral Dissertation, Ruprecht Karl University, Heidelberg, West Germany, Published by Beate Koenig, Potsdam, 1977, 88 pages.

16. Abstract

Young lunar impact structures were investigated by using lunar orbiter, Apollo Metric and panorama photographs. Measurements on particularly homogeneous areas low in secondary craters made possible an expansion of primary crater distribution to small diameters. This is now sure for a range between $20m \leq D \leq 20km$ and this indicates that the size and velocity distribution of the impacting bodies in the last 3×10^9 years has been constant. A numerical approximation in the form of a 7th degree polynomial was obtained for the distribution.

17. Key Words (Selected by Author(s))	18. Distribution Statement
	Unclassified - Unlimited

19. Security Classif. (of this report)	20. Security Classif. (of this page)	21. No. of Pages	22.
Unclassified	Unclassified	114	

TABLE OF CONTENTS

INVESTIGATIONS OF PRIMARY AND SDCONDARY IMPACT STRUCTURES ON THE M0ON AND LABORATORY EXPERIMENTS TO STUDY THE EJECTA OF SECONDARY PARTICLES

Beate König

/1*

I. INTRODUCTION

For billions of years, the surfaces of the planets and their moons have been exposed to constant bombardment by meteorites, comets and interplanetary dust. If their impact velocities are great enough, these bodies produce characteristic impact craters whose size distributions represent a measure of the size and velocity distributions of the impacting particles, especially for heavenly bodies without any significant atmosphere.

The craters on the Moon have been investigated very intensively in the last ten years. It is no longer argued — even Gilbert guessed this in 1893 — that most lunar craters are impact structures (Opic, 1936; Baldwin, 1949 and 1963; Urey, 1952; Kuiper, 1954). The Ranger, Surveyor, Luna and Lunar Orbiter Missions made possible the examination of impact structures up to the meter range. Due to the Apollo missions, impact craters down to the µm range were finally discovered and examined and absolute dating was begun on a large number of rock samples (see for example Turner, 1971; Eberhardt, et al., 1973; Stettler, et al., 1973; Albee, et al., 1974; Jessberger, et al., 1974; Kirsten and Horn, 1974; Tera, et al., 1974).

By connecting such radiometric dating with crater frequency distribution we are now in the position to determine the absolute

* Numbers in margin indicate pagination in original foreign text.

age of lunar regions (Baldwin, 1971; Block, et al., 1972; Hartmann, 1972; Soderblom and Lebofsky, 1972; Neukum, et al., 1975a). It is not only possible to establish an absolute chronology for the development of the lunar surface, but one can make statements about the time course of the flux of meteorites in space near the Earth.

With increasing precision of investigations of lunar crater populations and formations, the influence on impact craters of the structure produced by ejecta, in particular of secondary craters, has been recognized (Shoemaker, 1965; Lucchitta, 1975; Neukum, et al., 1975b; Oberback, et al., 1975). Secondary craters are very difficult to distinguish from primary impact craters if they cannot be recognized on the basis of morphologic criteria (elliptical shape, appearance in clusters) (Oberbeck and Morrison, 1973). Many publications begin from the crater size distributions which contain a generally unknown percentage of secondary craters. The study of size distribution of secondary craters thus makes possible a quantitative estimation of the contamination of the size distribution of primary craters by secondary craters. Besides these important problems for the preparation of a lunar flux chronology, investigations of secondary craters are of interest because they contribute to a better understanding of the crater formation process together with the study of artificially produced impact and explosion craters /2 (Shoemaker, 1960; Gault and Heitowit, 1963; Gault, et al., 1963; Carlson and Roberts, 1963; Carlson and Jones, 1975; Schneider, 1975; Moore, 1976).

The size distribution function of primary impact craters in the diameter range (0.3 km $\leq$ D $\leq$ 20 km) is well known (see Neukum, et al., 1975b). In this work, the distribution curves will be determined in the small diameter range in order to be able to date young lunar structures. The study of secondary craters, in particular their size distribution and influence on

primary crater populations; was connected with this. To examine crater ejecta and their dynamics, secondary particles were produced in laboratory experiments by impacts of mm-sized projectiles. Their size, mass and angular distribution was determined. Similar experiments were conducted by Gault, et al., (1963). Gault and Heitowit (1963) and Schneider (1975). Using these phenomenological studies we attempt to determine how much the ejecta processes show characteristic uniformities in the formation of very different sized craters.

II. THE SIZE DISTRIBUTION OF LUNAR PRIMARY IMPACT CRATERS IN THE DIAMETER RANGE FROM 20 M to 20 KM / 3

Young lunar areas of ages $\leq 3 \times 10^9$ years (ejecta may cover larger more recent impact craters) have only a limited surface area and the number of superimposed craters on these areas (with diameters in the kilometer range) is small. Craters in the diameter range of 100 meters and less are statistically significant. Therefore, for an examination of these young regions, the size distribution of primary impact craters on the Moon (for a diameter range 0.3 km $\leq$ D $\leq$ 20 km see, for example, Neukum, et al., 1975b) must be expanded to smaller diameters in the range of 0.3 km $\leq$ D $\leq$ 0.8 km and determined more precisely than before (see Neukum and König, 1976). In order to prevent falsification of the distribution by secondary crater contamination, diligent selection of the test areas is necessary.

II. 1 Measurement methods and evaluation procedures

a) Photographic material

Photographs from the Lunar Orbiter 4 and 5 as well as those of Apollo mapping and panorama cameras which were obtained from the Goddard Space Flight Center (Greenbelt, USA) were used for the

measurements. Their selection was performed with the aid of the Guide to Lunar Orbiter Photographs (Hansen, 1970) and the Apollo 15, 16 and 17 Lunar Photography Index Maps. The resolution of the photographs used was 2-60 m for the Lunar Orbiter photographs depending on the altitude of the satellite (teleobjective; high resolution), or 17-40 m (wide angle objective; average resolution); for the Apollo mapping photographs, about 27 m (Doyle, 1972) and for the Apollo panorama photographs about 2 m (Doyle, 1972).

Transparent positives were prepared from the photographs. In the case of Lunar Orbiter photographs, we are dealing with a seven-fold enlargement. The Apollo photos were contact copies taken from the negative film rolls which were enlarged only in individual cases up to 2.5 times.

b) Measurement principle and equipment

The photographs selected for the measurements were first studied with a magnifying glass or a reflecting stereoscope. Finally, the measurement surfaces were established and the measurement area was delineated with polygon lines.

Two pieces of equipment were used for the measurement, an (x,y)-coordinate measuring device (for greatly enlarged photographs) and a stereo-comparator (type PSK2 of Zeiss Company), which was of primary use. In both cases, the data were automatically entered on punched cards on performance of the measurement. In the monoscopic measurements, the crater diameter was usually measured in the East-West direction from its inner to its outer shadow range. This occurred with the (x,y) unit by applying an ≈0.1 mm thick stadia line. Only craters were evaluated whose diameters appeared greater than 2 mm on the measurement photographs. The measurement error caused by the stadia line thickness is thus ≤5% of the crater diameter. /4

The crater diameters could be determined directly when using steroscopic photograph pairs, whereby the test mark was set at the highest points of the crater edge. If measurement was impeded by difficult terrain, angle of the Sun, or other reasons (e.g., non-circular craters) or if monoscopic pictures were used, then the four points were measured along the crater circumference (usually East-West, North-South). A circle was formed in the course of the evaluation by using these measurement points and an average crater diameter was calculated. The measurement precision was 5 µm on the measurement photographs; most were usually greater than 200 µm. The inaccuracy in the determination of crater diameter was <5 or <2.5%.

c) Data reduction

The photographic direction for most pictures used deviated by less than 8.6 degrees from the vertical direction. Since the dispersion error in the length determination is much less than the empirical error, these photographs can be considered to be vertical photographs. At greater inclined angles — in the case of panoramic photographs (angle of inclination: 12.5 degrees) — a correction of distortion was performed.

The scales of the measurement photographs were calculated from the known data of the camera photographs and the focal lengths of the camera lenses as well as from the NASA-NSSDC catalog and the Apollo 15, 16 and 17 "Index of Mapping Camera and Panorama Camera Photographs"; moreover the local relief of the lunar surface was considered (altitude correction), for which the height profiles determined by laser measurements were included. For the lunar orbiter photographs which did have photographic errors and for the panorama photographs, additional lunar topographic and photomaps were used for calibration of the photograph scale; these are cited in the literature section.

The surface area of the measurement region limited by the polygon was calculated manually in the evaluation by an (x,y)-unit. When using the stereocomparator, the calibration points were measured directly and the surface area was calculated automatically.

The panorama photographs were only evaluated in the middle of the picture. The following corrections served for picture correction of the crater diameter; D (corrected) = D (measured) / cos δ, where δ is the angle off the vertical of the camera axis. In the calculation of the measurement surface, the picture distortions were considered accordingly.

The measured crater diameters were arranged according to /5
their size in 108 intervals between 1 m and 100 km. The intervals had about the same logarithmic width. Differential frequencies were determined for the intervals and integral crater frequencies were calculated from this, i.e., the number of craters having diameters greater than or equal to the lower interval limit. The statistic error was used for citing deviations, i.e, the square root of the integral frequency. These values were standardized to the surface area, expressed and plotted.

Computer programs were prepared so that the evaluation of the rather extensive measurements (with a few exceptions) could occur by the computer of the institute.

II. 2. Areas examined

a) Selection

To determine the size distribution of the primary craters, measurements had to be performed on areas which had undisturbed primary crater populations. For their selection we used different

criteria (see Neukum, et al., 1975b; Neukum and Horn, 1976; Neukum and König, 1976).

- The areas to be examined should be free of secondary craters if possible, i.e., larger craters must not be located in the vicinity of the stray fields. The best areas are those located on the lee side of larger rises, i.e., generally screened from ejecta.

- The craters should not be flooded with lava.

- They should be flat since erosion is particularly heavy on greatly inclined slopes.

- Their crater populations should be located in the examined diameter range (i.e., every impact should not lead to the destruction of already present craters). Otherwise the crater population is near equilibrium where the size distribution is generally independent of the size distribution of primary craters and follows the law $N \sim D^{-2}$ (Trask, 1966; Gault, 1970; Neukum and Dietzel, 1971).

- They may not be located in volcanic regions to avoid mixing of endogenic craters (König, 1974).

It proved to be extremely difficult to find regions which met all these criteria. The condition of minimal secondary crater mixing restricted the selection of suitable surfaces very much; there are almost no larger areas where no secondary craters are contained in the crater diameter range under consideration (see Section IV 3). As a consequence of the high crater densities, older areas ($t_i \geq 3.5 \times 10^9$ years) are excluded in advance; on the one hand because they have a high percentage of secondary craters in proportion to the primary crater density, and because /6

their crater populations in the interesting regions D < 300 m does not exhibit a production but rather a saturation distribution (see Neukum, et al., 1975b). For areas having lower crater densities — younger formations — the criteria are easier to meet. Here one can eliminate secondary craters provided they show those characteristics, i.e., formed in clusters or in V-shapes or in elipses (Oberbeck and Morrison, 1973; Section IV 2). Unfortunately, the surface area of the suitable young regions is small. Therefore, the size distribution of the crater can only be determined in a limited diameter range: restrictions to the smaller crater sizes resulted for example, from the texture of the measurement surface or the quality of the photographic material, whereas statistics sets a limit to the use of larger crater diameters.

b) Measurement regions and results

The regions and the measured crater size distributions used for the determinations are discussed below.

One of the two Mare areas investigated lies in the Mare Imbrium in the West of the Delisle β rise (Figure 1a). It is shielded against ejecta by the craters Delisle and Diophantus. Other dispersion fields of younger craters are so far away that contamination of the measured craters by secondary craters is considered minimal. A smaller flooding zone appears to cross the entire surface but causes only a slight modification of the crater size distribution (Figure 2). The measurement therefore occurred in two steps: only the larter craters were measured over the entire region and the smaller craters were measured on a homogeneous subregion.

The second Mare region (Figure 1b) lies at the Western edge of the Serenitatis basin to the southeast of the Sulpicius Gallus

crater. It is shielded against ejecta from a westerly direction by the edge of the basin. Possible sources of secondary craters which could influence the measurements are the craters Sulpicius Gallus, Menelaus and Bessel. For the following reasons these craters probably do not contribute significantly to the secondary craters on the measurement range:

- The Apollo photographic material has shown that the dispersion field of Sulpicius Gallus is flooded (König and Neukum, 1977). Therefore, this crater is older than the measurement region which lies nearby. /7

- As one can see from the ray system of the young Copernicus-like crater Menelaus (Carr, 1966), the measurement area does not lie in a main direction of ejecta.

- The Bessel crater lies at a distance of 12 crater-radii from the measurement area. As detailed investigations by Neukum, et al., (1975b) show, at a distance of about 7 crater radii, the contribution of secondary craters (having diameters of about 1 km) can be neglected.

The validity of the assumptions is confirmed by the consistency shown by the distribution determined for diameter ranges from 0.4 - 0.9 km compared to other craters.

The structures belonging to young craters are particularly suitable for studying the size distribution of impact craters since the crater populations superimposed on them are less exposed than older structures to the highly exogenic processes because of the low age of the target. For young regions like North Ray, Tycho and Aristarchus, the potential contamination of their superimposed impact craters by secondary craters is minimal (Hartmann, 1968), because there are no other larger young craters in their vicinity whose secondary craters could falsify the

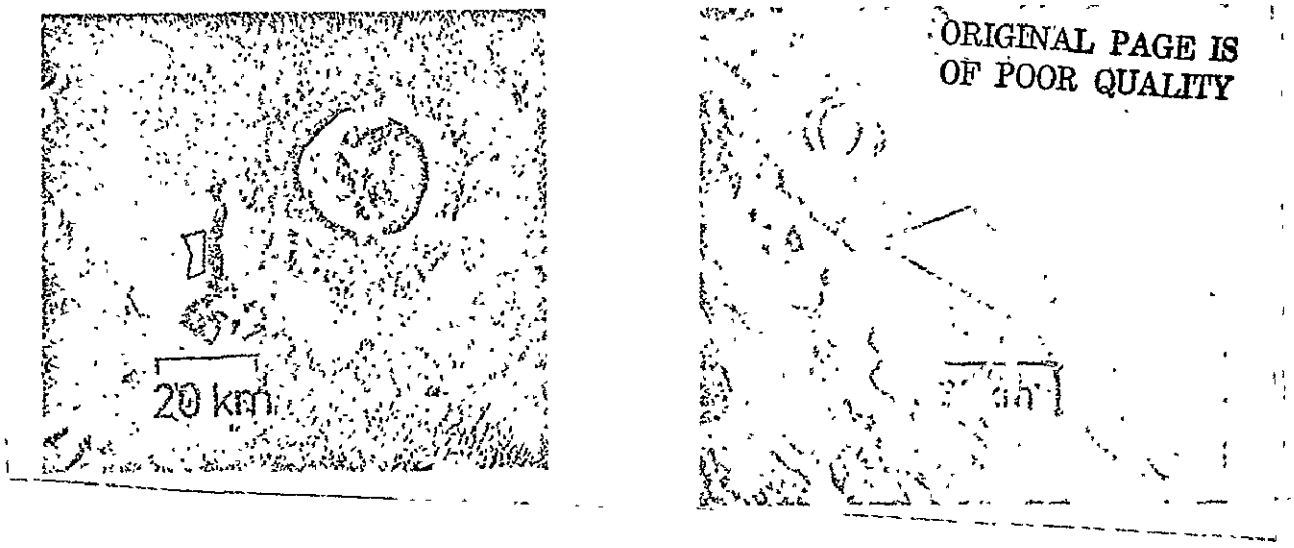

Figure 1. Measurement region on the Mare plane.

a) In the West: The Delisle crater in the Mare Imbrium (AS15-2333)

b) Southeast of the Sulpicius Gallus crater in the Mare Serenitatis (AS17-807).

distribution. The measurements at North Ray, Tycho and Aristarchus provide a series of size distributions which extend over a relatively large diameter range. These measurements will be discussed in connection with the dating of these craters in Chapter 3.

/ 8

In the Taurus Littrow valley at the Apotto 17 landing site, crater diameters in the range of 25 m $\leq$ D $\leq$ 110 m were measured on the younger structures of the light mantle and the central cluster region. The relationship of these regions with the Tycho crater is discussed in Section III 2b. The measured distribution is not completely undisturbed in the D < 50 meter range (erosion, intermingling of secondary craters), however, it does make possible the adaptation of North Ray data for 20 m $\leq$ D $\leq$ 40 m.

Another region which was used for expanding the distribution curve lies on the continuous ejecta cover of the Theophilus crater. Here we referred back to keasurements which had already been published (Neukum and König, 1976). In this respect the good

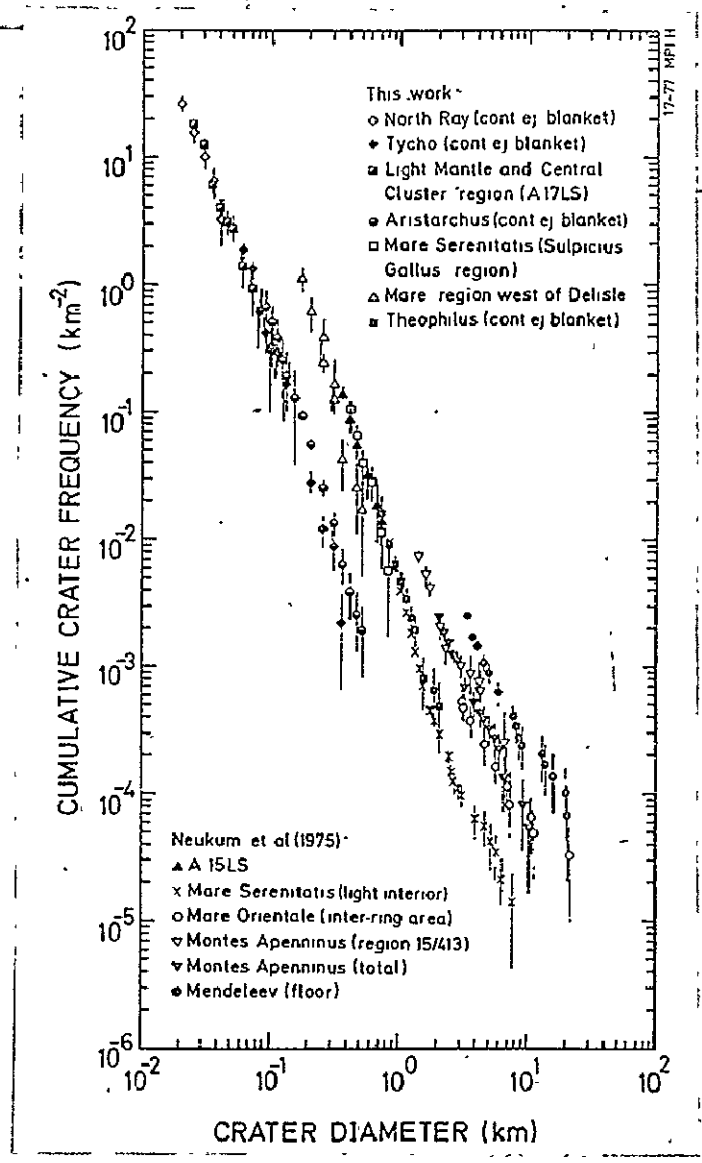

Figure 2. Integral size distributions which were used to redetermine the crater size distribution function.

correlation of empirical distributions in the inner and on the continuous ejecta blanket of the crater was shown; consequently, no significant contamination by dispersion fields of other large craters occurred. The data extend over the diameter range of 0.7 km $\leq D \leq$ 2 km and connect with the Serenitatis measurements of Neukum, et al. (1975b). A series of crater size distributions were taken from Neukum, et al. (1975b). These measurements were performed in the inner ring of the Mendeleev

crater, on the inner ring region of the orignetal basin and at the Apollo 15 landing site. The data of Greeley and Gault (1970) were not used in this study. /9

All measured distributions are summarized in Table 2 and they form the basis of the expanded size distribution curves.

c) Standardization of measured distributions

The results obtained show that the crater size distribution can be determined for the various regions only in a limited diameter range. Therefore, it is necessary to determine the total distribution by suitable standardization or correlation of the individual distributions.

The integral crater size distribution can be described by

$$N(D,t_i) = \int_D^{\infty} \int_{t_i}^{0} g(D',t)\, f(t)\, dD'\, dt$$

where g is the size and time dependence of the size distribution, f(t) is the general time dependence of the impact rate, N is the integral crater frequency for a diameter D and t_i is the time of crater accumulation (see also Neukum, et al., 1975b). If the crater size distribution is independent of time, the simplified expression

$$N(D,t_i) = \int_D^{\infty} g(D')\, dD'\, F(t_i),$$

$$F(t_i) = \int_{t_i}^{0} f(t)\, dt$$

where results for the time integral of the flux. For two crater populations, N_1 and N_2, having ages t_1 and t_2 we have: $N(D,t_1)/N(D,t_2) = F(t_1)/F(t_2) = C$. This constant is not dependent on crater size but only on age. Therefore, one can standardize the crater frequencies of differently aged regions to each other if — as will be described below — the crater size distribution is constant in time for the considered diameter range.

The standardization of crater size distribution is done stepwise from regions of larger crater diameter to smaller diameters. Here the Mare Serenitatis (Light Interior) population serves as an initial distribution. The already standardized distribution of Mendeleev, Orientale, the Montes Appenninus and the Apollo 15 landing site were taken from Neukum, et al. (1975b). Correlation of the distributions was performed in the region with the best statistics and best overlapping. The Theophilus and the new Serenitatis measurements improved the statistics and plotting of the curve in the region between 0.4 km and 2 km which was covered only by the Apollo 15 landing site and the old Serenitatis /10 data. The Imbrium distribution could be easily adapted to this, likewise for the connecting Aristarchus measurements which extended up to 90 m. The Tycho measurements between 60 m and 350 m and the data obtained in the Taurus Littrow valley between 25 m and 100 m were standardized. Subsequent correlation of the North Ray data (20 m - 40 m) occurred without any difficulties.

In Figure 3 we see the empirical curves standardized on the Mare Serenitatis crater frequency. The investigated crater populations fall within the statistics of a general size distribution.

d) Numerical approximation of distribution

The known integral size distribution of the crater makes it possible to compare the measurements with each other over different diameter ranges. Here it is useful to relate comparisons to the same reference value. In the course of this work we selected $D_r = 1$ km as a reference value. In order to obtain sufficiently precise results for this procedure, a numerical expression was prepared for the distribution curve. It was adapted to a 7th degree polynomial by the standardized integral frequencies which is shown in Figure 3. It has the general form

$$\log N = a_o + a_1 \log D + a_2 (\log D)^2 + \ldots + a_7 (\log D)^7$$

Its coefficients are:

$a_o = -2.419$
$a_1 = -3.852$
$a_2 = 0.741$
$a_3 = 0.926$
$a_4 = -0.254$
$a_5 = -0.349$
$a_6 = 0.036$
$a_7 = 0.046$

The formula provides the integral crater frequencies per km^2, if one gives the diameter D in km.

The coefficients are valid for the range 20 m $\leq$ D $\leq$ 20 km but not for ranges greater than this. The determined size distribution curves represent the general distribution of lunar impact craters on regions with ages between 50 million years and more than 4×10^9 years. On the average the quality of the approximation in the diameter range 20 m $\leq$ D $\leq$ 20 km is about 60% (standard deviation). The size distribution curve between 0.8 km $\leq$ D $\leq$ 3 km is the best; it has an uncertainty of <25%. Because of the necessary successive standardization process for smaller crater diameters, the position of frequencies for D $\lesssim$ 100 m relative to D = 1 km is only determined to within ±50%. The comparison of diameter ranges of crater frequencies of smaller craters determined in similar diameter ranges results in smaller errors.

The distribution function agrees with the percentage function cited by Neukum, et al., (1975b) in the diameter range D > 300 m to within 20%.

ORIGINAL PAGE IS
OF POOR QUALITY

/11

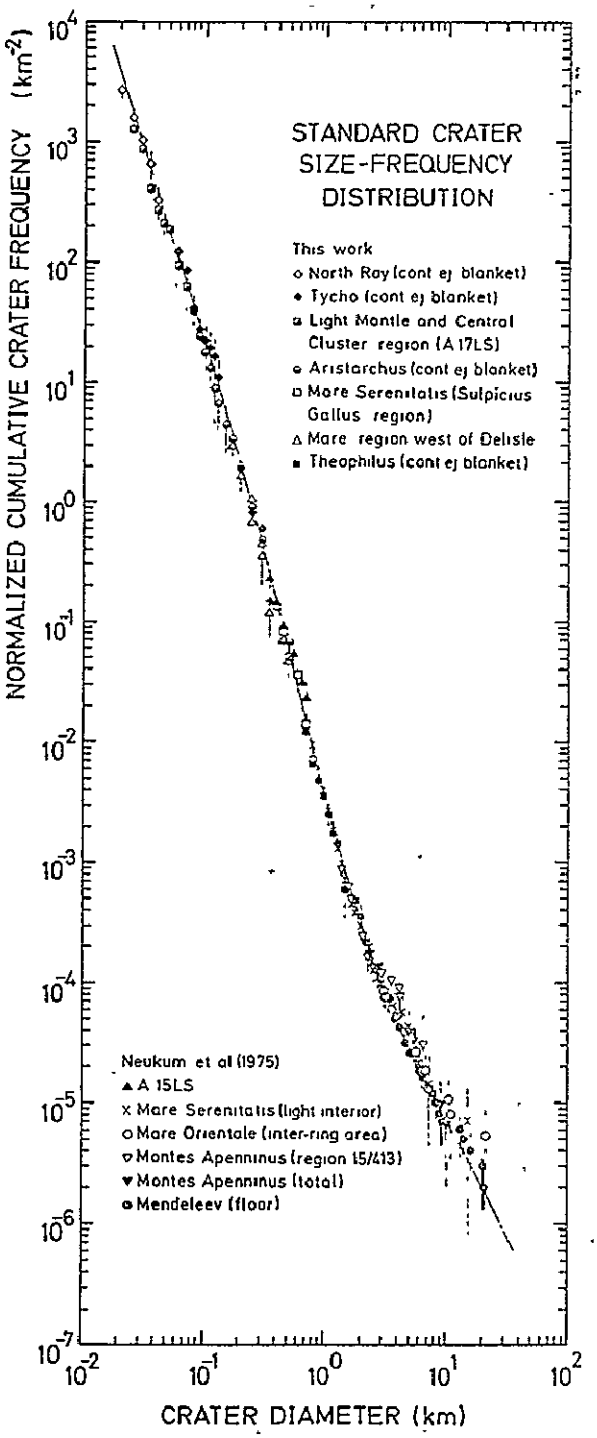

Figure 3. Integral size distributions of all crater populations investigated, standardized on the frequency of the Mare Serenitatis. The curve passing through the data represents a polynomial approximation.

In order to get a general mathematical expression for the integral distribution curve for a certain region, a term must be added to the polynomial formula which considers the age t_i of the region. $\log N = a_o + a_1 \log D + \ldots + a_7 (\log D)^7 + \log F(t_i)$, where $F(t_i)$ is the time integral of the meteorite flux to which the area has been exposed since its creation. For the numerical approximation of the Serenitatis distribution, $F(t_i)$ was arbitrarily set equal to 1. /12

e) Discussion

The crater diameter distributions in the range $0.8 \leq D \leq 10$ km which were measured for 3-4 billion year old regions agree with each other (Neukum, et al., 1975b). This work showed that the distributions in the range 20 m $\leq D \leq$ 2 km on (0.1-3) billion year old regions likewise agree with each other and that the total data can be combined to a total distribution. Even the facts that this is easily possible, i.e., that by successive standardizations of individual distributions to each other, a smooth, functional curve results and they indicate that the crater size distribution was not subjected to any significant variations. The above also governs the size and velocity distributions of the crater-producing bodies.

No information has yet been obtained for the size distribution of craters $D < 300$ m on old regions ($t_i > 3.5$ billion years), since in these cases saturation effects (i.e., the destruction of original craters by subsequent ones) do not permit any meaningful measurement. In the region of large craters, the statistics represent the limiting factor. This is especially true for young regions (i.e., regions of low crater density). In these regions, therefore, temporal variations in the crater size distribution cannot be excluded as a possibility.

The size distribution curve of the lunar impact craters reflects the mass/velocity distribution of the impacting bodies. It is therefore possible to draw conclusions about the origin of the impacting bodies from a comparison of size distributions of the impact craters with those of present asteroid groups as well as from considerations of the flux of the impact bodies (Neukum, et al., 1975a; Wetherill, 1976). The resulting conclusions make it possible to provide a flux curve of these particles in connection with the investigations of the flux of interplanetary bodies in recent times (see Section III 3b).

The distribution curve is derived from measurements on homogeneous areas and represents the standard size distribution of non-disturbed crater populations. Therefore, the deviation of /13
a major distribution from the standard means that the region concerned has experienced a disturbing process, like, for example ejecta coverings, floods, erosions, etc., in favorable cases the original age of the surface and the time of its modification can be obtained in addition to the general distribution curve (see Neukum, et al., 1975a).

The selection of regions occurs from the point of view that the crater population must be as free as possible from secondary craters. Nevertheless, a contamination can have occurred due to statistically distributed secondary craters which are not distinguishable from primary craters. But since secondary-crater sources are almost completely lacking for the youngest regions investigated (North Ray, Tycho, Aristarchus) and the corresponding measurement distributions agree with the age of the older objects (see Section II 2b), one can conclude that the measured size distributions are actually free from secondary effects. The distribution functions can be represented as $N \sim D^{\alpha(D)}$, where the exponent is a function of the crater diameter D. This expression differs from the special relations used in the older literature where α is assumed to be a constant (Shoemaker, 1970;

Baldwin, 1971; Hartmann and Wood, 1971). Formulas having constant exponents are therefore not valid over the entire diameter range and their use can lead to errors of up to a factor of 10 (Neukum, et al., 1975b). This fact is illustrated in Figure 4.

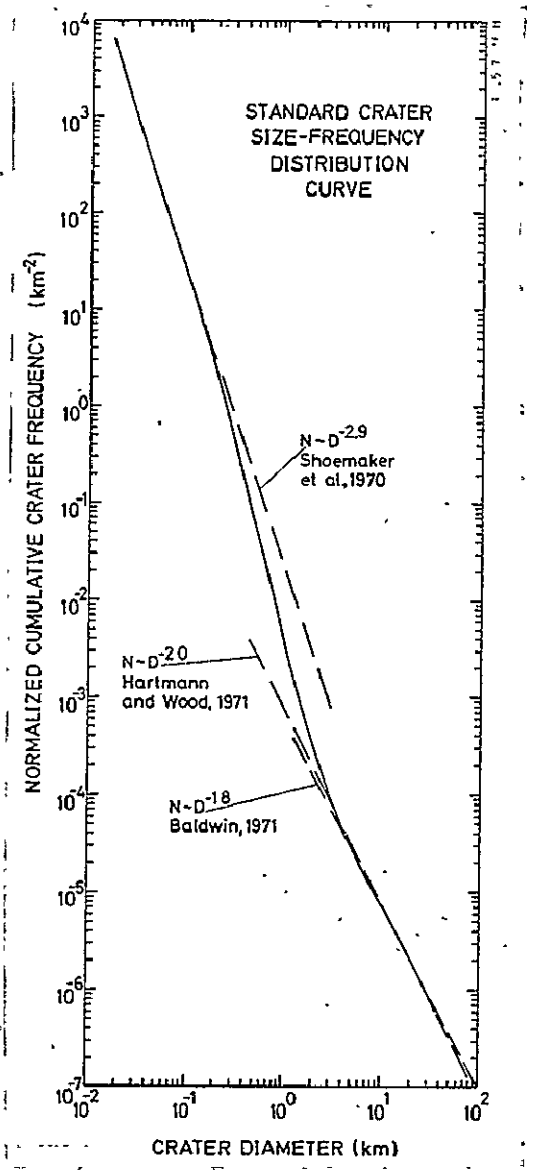

Figure 4. Comparison of the derived crater size distribution function with distributions cited in the literature. They have been suitably standardized and entered in the regions of their cited validity.

III. DATING OF YOUNGER IMPACT STRUCTURES ON THE MOON

The size distributions determined in the preceding chapter /14
make it possible to prepare a relative chronology of recent large impact craters (see Neukum and König, 1976). This is of particular interest since it is possible in many cases to move from a relative to an absolute determination of age by using additional data about the radiometric age of younger impact craters. On the basis of this information, conclusions can be drawn about the flux of impacting bodies and its chronology.

III.1 Impact craters

In the following, investigations are discussed which were performed on the structures of the craters Copernicus, Kepler, Aristarchus and Tycho. In order to restrict the discussions of the measurements to the various type terrains, first using Aristarchus as an example, we briefly discuss the general structure of one such crater. /15

Figure 5 shows a photo mosaic of the Aristarchus crater (D = 40 km) and its surroundings. The interior walls of the crater have step-like terraces and in its middle there rises a central mountain characteristic for craters having diameters of the size of about 15 km. The crater base itself is flat and covered with a layer of broken rocks (particles which fell back into the crater). On the basis of detailed investigations (Guest, 1973) it follows that this region was created almost simultaneously with the other crater structures. The outside crater wall is somewhat covered with flow structures consisting of rubble. The zone of continuous ejecta cover connects with this region. This zone extends from the crater edge out to a distance of about 1 crater radius. This is a layer of fragmented material. It was formed primarily by ejecta and by the addition of local material

ORIGINAL PAGE IS
OF POOR QUALITY

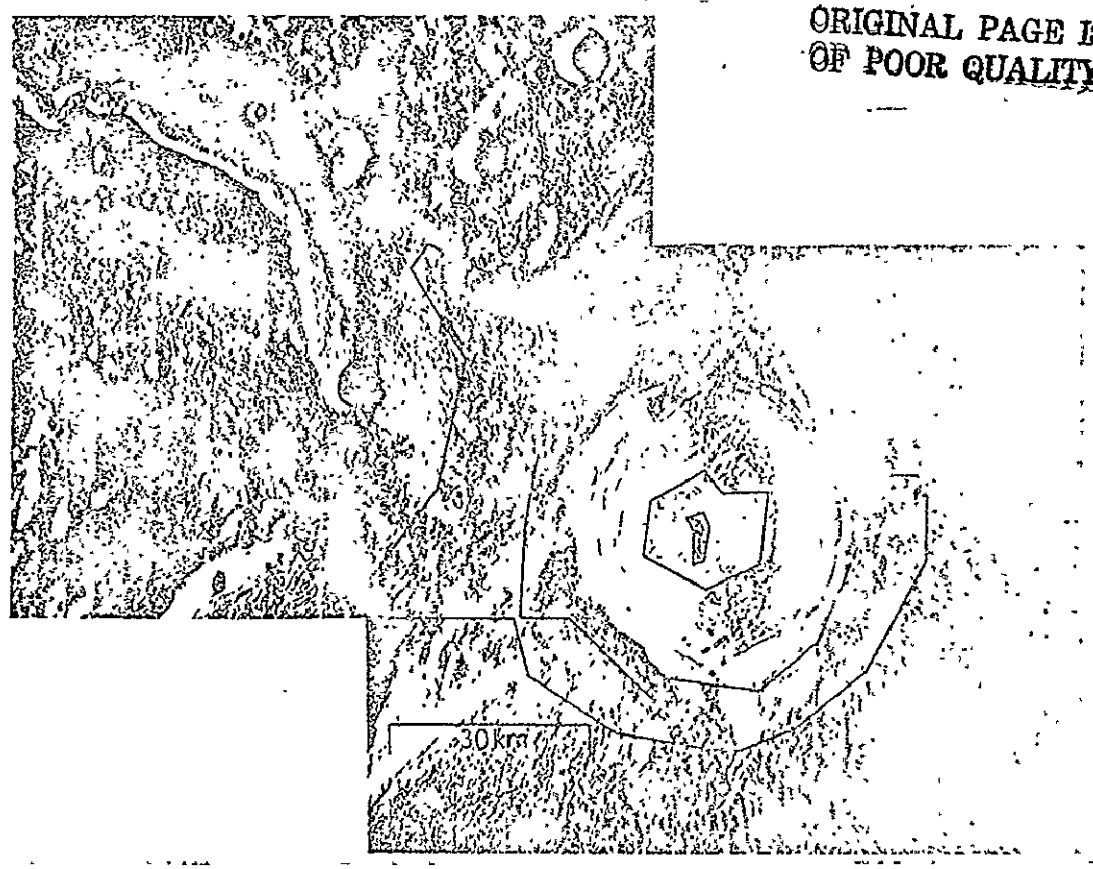

Figure 5. Aristarchus crater and surrounding area (Mosaic from the LO V 198 M and 202 M-photographs). The test regions on the continuous ejecta cover and in the crater interior are illustrated.

(Oberbeck, et al., 1975). The discontinuous ejecta region connects to this zone; the ejecta cover is thin or no longer cohesive here and individual secondary craters can be distinguished. Chains of eliptically-shaped secondary craters are situated radially to the Aristarchus crater which were caused by the impact of ejected materials (e.g., Guest, 1975).. These craters often show typical V-shaped structures whose peaks point to the primary crater (see also Figure 29b). The original mechanism of these structures was studied in detail by Oberbeck and Morrison (1973). In addition to these chains there are individual clusters of secondary craters. They were created by the impact of groups of ejected material.

The investigations described below were performed on these different type terrains of the craters Copernicus, Kepler, Aristarchus and Tycho. Additional measurements were performed on the ejecta covers of North Ray. As far as possible, measurements were performed on subdivided surfaces as long as the statistics made this seem useful, and if possible measurements were performed on different regions on one and the same type of terrain in order to exclude local effects which would jeopardize the measurements, like for example, erosion or contamination from secondary craters.

a) Copernicus

One of the best-known craters on the front side of the Moon is Copernicus. (D = 92 km), whose bright ray system can be easily seen with a telescope. The test regions lay in the inside of the crater (Figure 6) along the continuous ejecta cover (Figure 7) and on the discontinuous ejecta blanket (Figure 8). The base of the crater and the continuous ejecta cover are standard regions, so to speak, for the dating of large craters by means of frequencies of the craters superimposed on them. The measurements along the discontinuous ejecta cover were performed in order to check the possibility of dating this type of terrain.

The crater base of Copernicus has a coarse texture. However, there are a sufficient number of smaller craters for measurements to be performed in this region with sufficient statistics. The area of the dentral mountains was not included in the measurement surface and a cluster of secondary craters in the Northeast of the crater base was excluded from the measurements. The size distribution of the measured crater is shown in Figure 9.

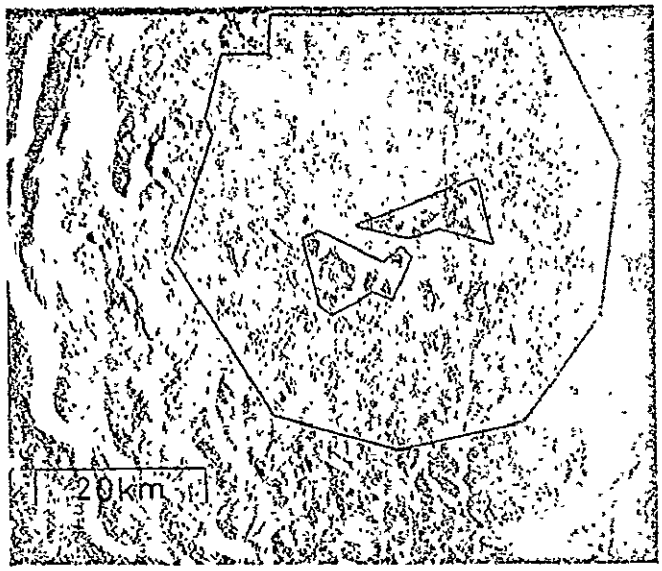

Figure 6. Measurement surface (without the area of the central mountain) in the interior of the Copernicus crater.

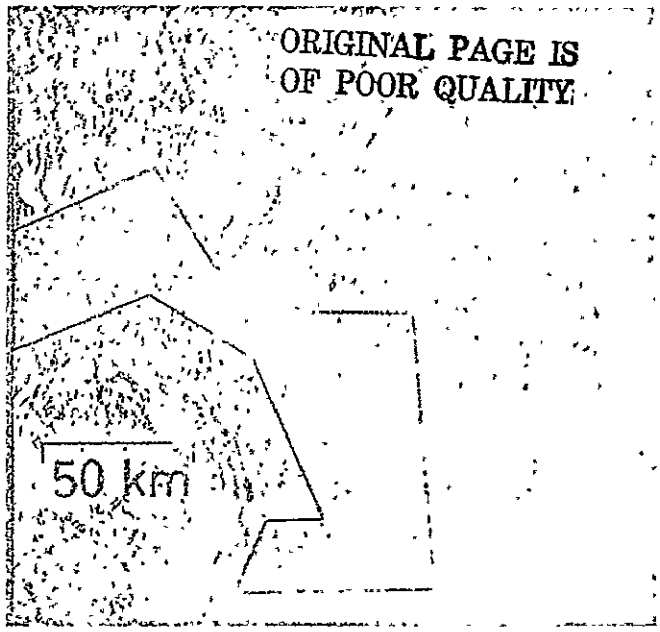

Figure 7. Measurement region on the continuous ejecta cover of the Copernicus crater.

Measurements on the continuous ejecta cover in the W est of the crater were problematic since secondary crater contamination occurs there. This is attributable to the younger craters Kepler and Aristarchus, but also possibly to the Copernicus ejecta itself. Therefore, as a test area we selected a surface in the East of Copernicus which is screened by the crater wall against flying ejecta at low angles from a westerly direction. As Figure 9 shows, a good correlation of test results was obtained with the data from the crater interior.

By using two consistent empirical curves, it was possible to stress the investigation of the discontinuous ejecta cover. Since the size of the ejecta cover decreases with increasing distance from the crater, a complete covering of the pre-Copernican terrain by ejecta must be considered. This region contains a number of secondary crater groups in addition to secondary

crater chains (see Chapter IV). In order to be able to perform measurements of the primary post-Copernican crater frequencies on this region, a thorough view of the terrain under question is necessary. It was determined here that the craters had been eroded more heavily on the discontinuous ejecta cover than on the continuous ejecta blanket in the crater interior. This is probably based on loose target material. In order to make quantitative measurements and to avoid possible secondary craters of Copernicus, the investigations were limited to crater diameters > 450 m. The results agree with the data which were obtained from other regions (see Figure 9). By using great care, the discontinuous ejecta cover can be applied to the dating of a crater. /17

The crater size distributions measured on the different regions of the Copernicus crater are shown in Figure 9. The general distribution curve was drawn through it, under consideration of the reliability of the data.

/18

For D = 1 km there results an integral crater frequency of $(1.0\pm0.3) \times 10^{-3}\,km^{-2}$.

In Figure 10 the empirical data of Hartmann (1968) and of Greeley and Gault (1971) are entered for comparison to the distribution curves obtained from our own empirical data. The data agree well in the region of greater crater diameters, only a measurement by Hartmann, which probably included secondary or pre-Copernican craters, deviates from this.

The integral distributions determined by Greeley and Gault for smaller crater diameters follow the slope -2, deviating from the general curve. These crater populations already appear to be at equilibrium.

ORIGINAL PAGE IS
OF POOR QUALITY

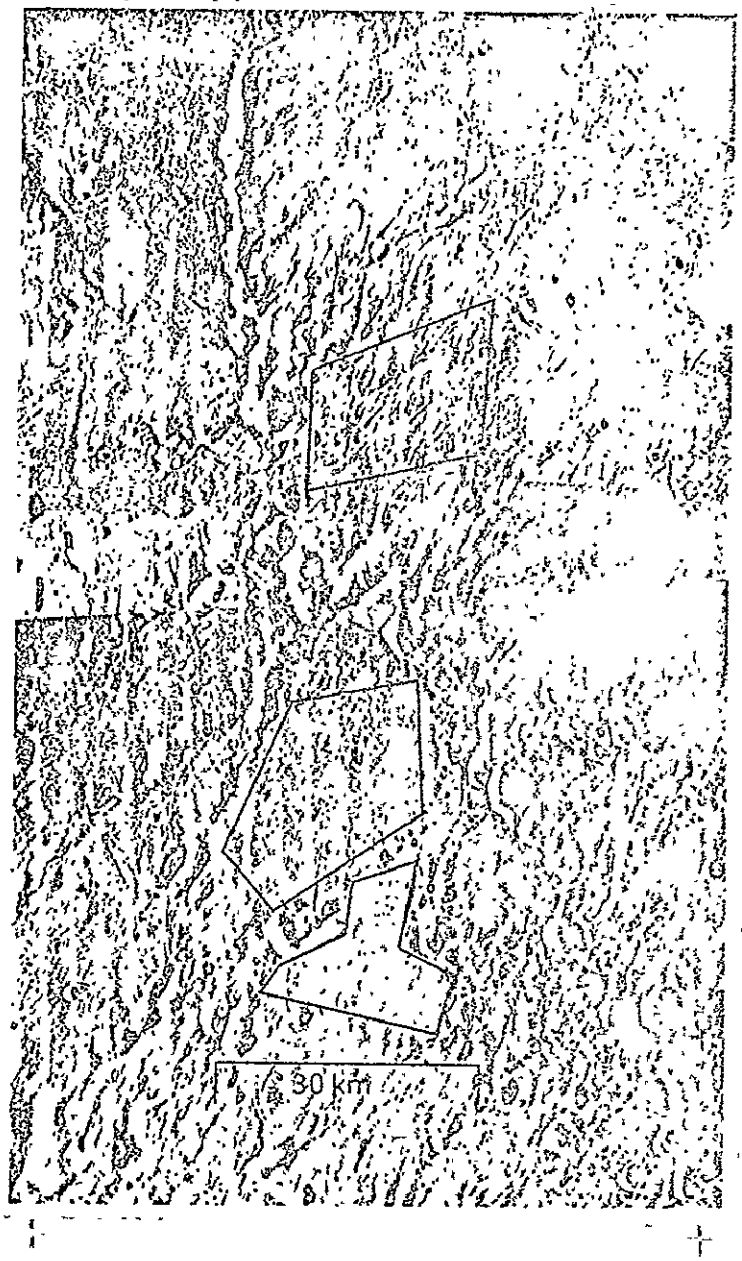

Figure 8. Test regions on the discontinuous ejecta cover of Copernicus (photo mosaic from LO V 142 M, 143 M and 144 M).

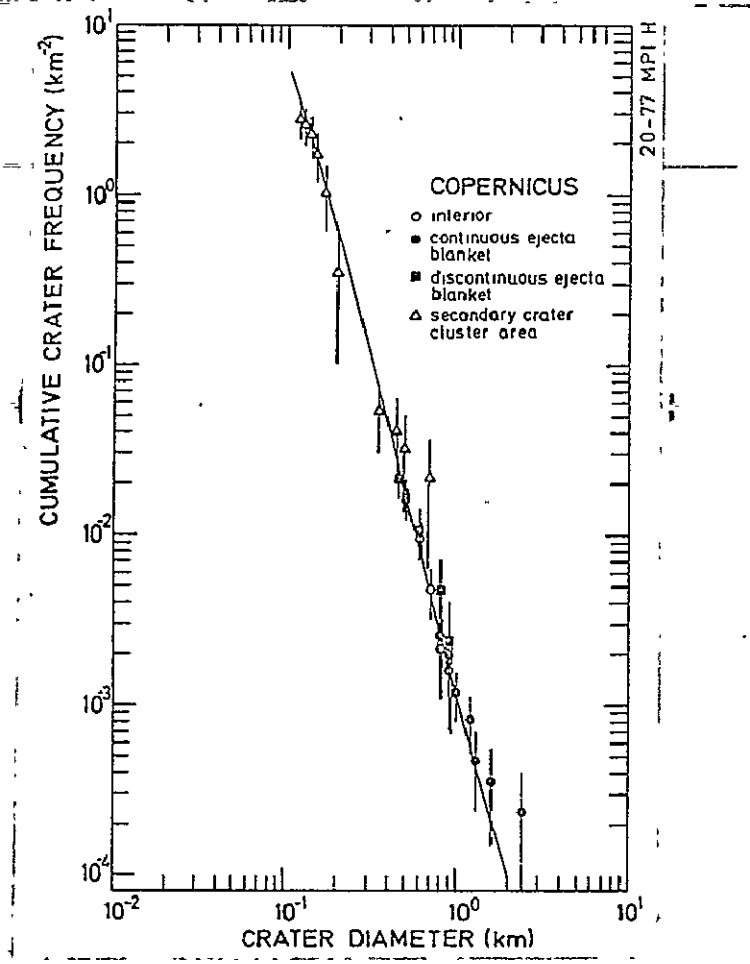

Figure 9.. Crater size distributions measured on the structures of Copernicus. The general size distribution curve is drawn through the measured points.

A telescopically observed ray of bright ejecta material from the Copernicus crater extends as far as the Apollo 12 landing site. Shoemaker, et al., (1970) interprets the bright, fine-grained material found under the surface as ray material. Samples taken there were examined by various methods (U-Th-Pb, $^{39}Ar/^{40}Ar$, K/Ar) (Silver, 1971; Eberhardt, et al., 1973; Alexander, et al., 1976) and a great heating millions of years ago (850 ± 100) was determined. On the basis of this dating. Copernicus was assigned a radiometric age of 850 ± 100 million years.

b) Kepler

The dating method used in this work has not been previously applied to the Kepler impact crater (D = 32 km) which exhibits a striking ray system. Until now it has been investigated only by morphologic-stratographic methods (see Section 3a) and classed as a recent crater. Kepler was dated because the age of the primary crater should be known for the study of the state of erosion or of the morphology of secondary crater structures (see Chapter IV).

The pictures available for the measurement (Figure 11) were of only average quality so that the investigations proved to be difficult. The only region measured was the ejecta cover, /19
which was measured at four individual surfaces in order to be able to determine possible, locally-caused deviations in the measured crater frequencies. The superimposed craters were barely discernable and thus the diameter could not be determined precisely. Consequently, there resulted a data dispersion in the four regions which, however, was small enough so that three craters in the Northeast were excluded. These were already noted during the measurements as not definitely belonging to the crater population examined (pre-Kepler or secondary). The summarized measurements are entered in Figure 12 and produce an integral crater frequency of $(7.5 \pm 2.5) \times 10^{-4}$ km^{-2}. Thus Kepler is clearly older than Aristarchus. Its secondary craters appear fresher than those of Copernicus (see Chapter IV) and thus one could conclude with relative certainty that Kepler and Copernicus are of a similar age.

c) Aristarchus

In the interior of the Aristarchus crater (D = 40 km) measurements were taken using average and high-resolution photographs (Figures 5 and 13). Since the crater floor is very uneven, only craters having diameters > 140 m could be quantitatively

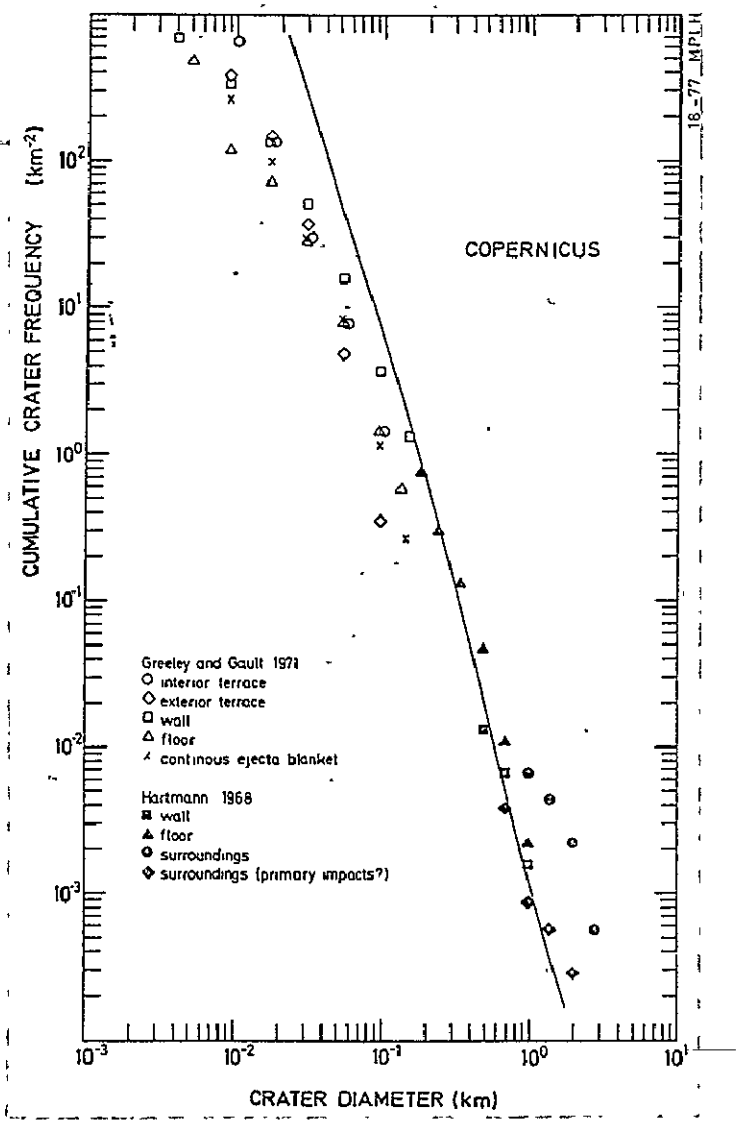

Figure 10. Measurements on structures of the Copernicus crater. Comparison of results of this work (solid line) with results of other authors.

recognized and measured. Consequently the resulting statistics are not very satisfactory.

A much greater number of craters of diameters of between 4.0 m and 500 m were measured on different regions of the continuous ejecta cover (Figures 5 and 14 a,b). Within the statistical uncertainties the data obtained in the crater interiors and on the

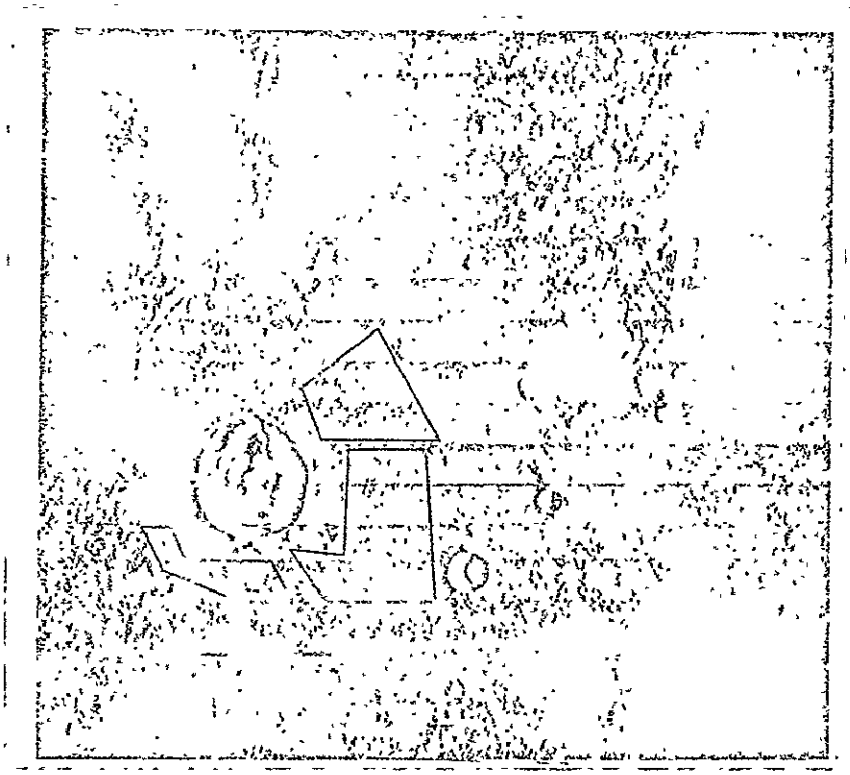

ORIGINAL PAGE IS
OF POOR QUALITY

Figure 11. Kepler crater and surroundings. (Photomosaic from LO IV-138H1 and 138H2) measurement areas are shown.

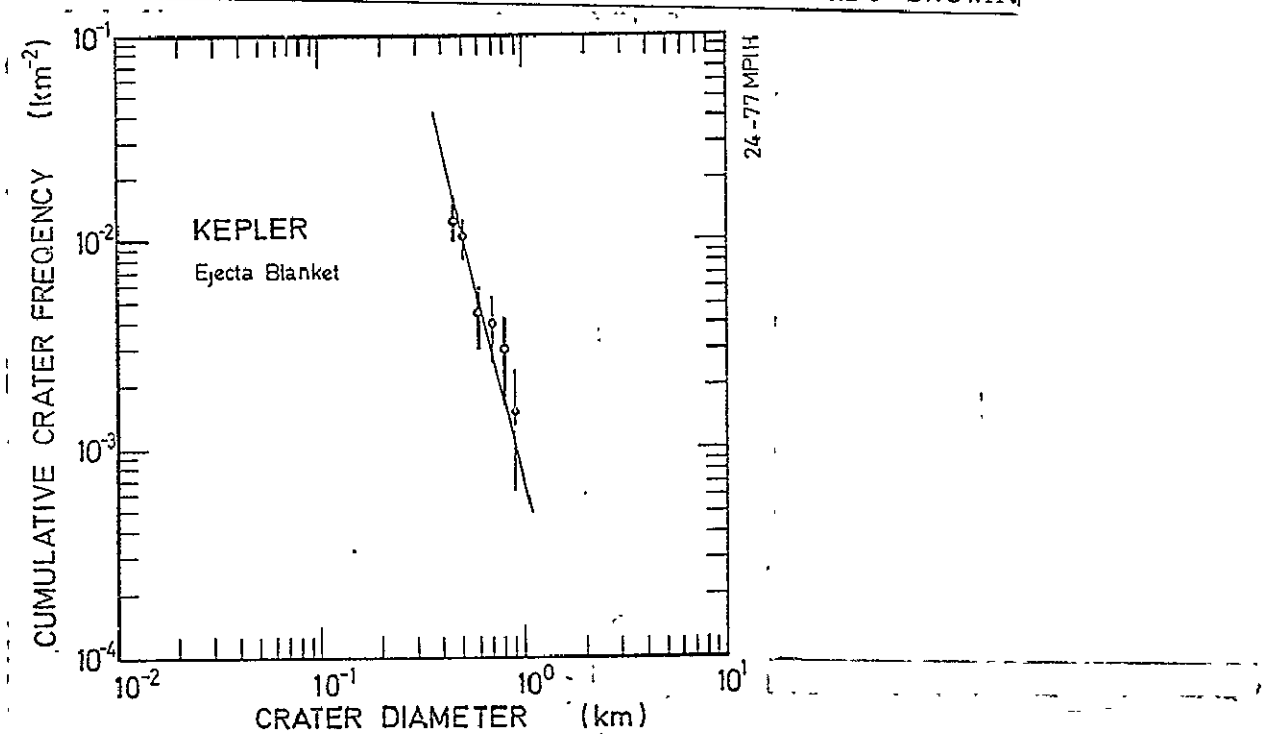

Figure 12. Crater size distribution measured on ejecta cover.

ejecta cover agrees well with that obtained from other craters.

This can be seen in Figure 15. The general crater size distribution curve was drawn through the measured crater size distributions and there resulted for D = 1 kilometer an integral frequency of $(1.2 \pm 0.2) \times 10^{-4}$ km^{-2}.

ORIGINAL PAGE IS
OF POOR QUALITY

Figure 13. Measurement area in the interior of the Aristarchus crater (photomosaic from LO V 198 H2 and 199 H2).

ORIGINAL PAGE IS
OF POOR QUALITY

a) LO V 196H3

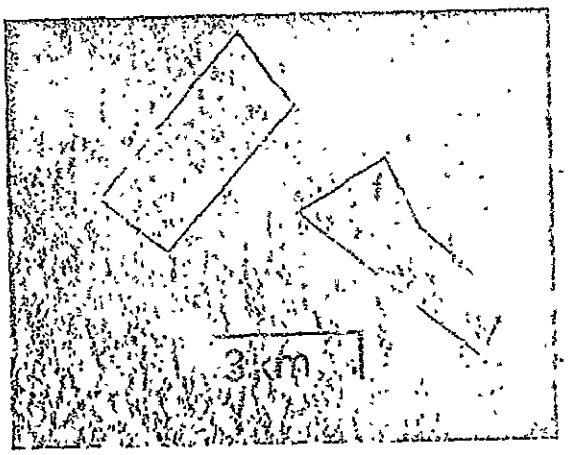

b) LO V 201H2

/21

Figures 14a and b. Measurement regions on the continuous ejecta cover of the Aristarchus crater.

In Figure 16 the data of Hartmann (1968) and Greeley and Gault (1971) are entered for comparison. The results of Greeley and Gault agree with those of this work in the region of small crater diameter. For larger diameters, the crater frequencies are superelavated; possibly these authors also measured pre-Aristarchus or secondary craters. The points measured by Hartmann for larger crater diameters bend down at smaller diameters. This bending down of crater size distribution is probably attributable to the fact that small craters can no longer be quantitatively recognized because of roughness of the crater base.

/23

d) Tycho

The crater Tycho (D = 85 km) is younger than Aristarchus as morphologic investigations, radar studies and thermal anomalies show (e.g., Hartman, 1968; Pettengill and Thompson, 1968; Allen, 1971). There are only a few larger craters in the interior. Since the bottom is very uneven, the measurements there (Figure 17) were limited to a few craters (see Figure 20).

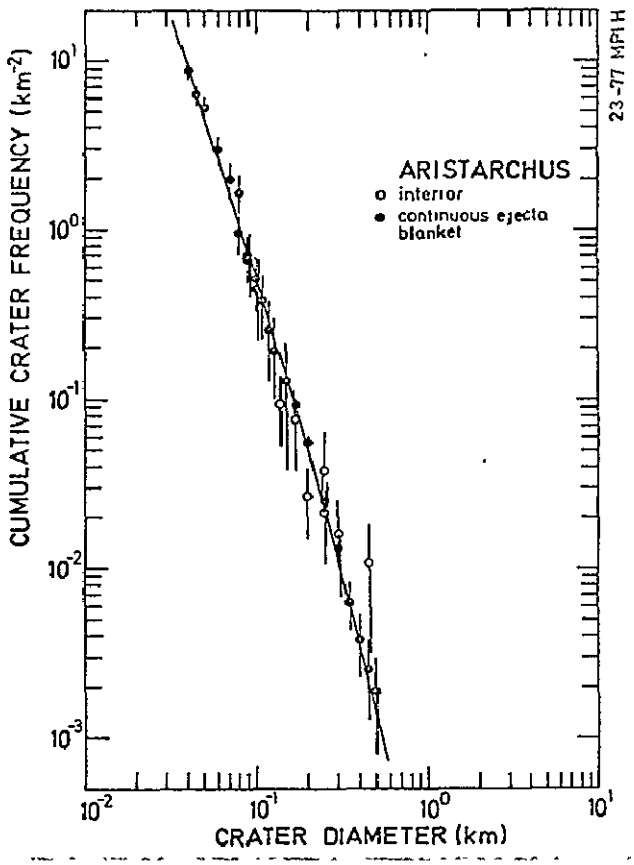

Figure 15. Crater size distributions measured in the interior and on the continuous ejecta cover of the Aristarchus crater. The general crater size distribution curve is drawn through the measurement data.

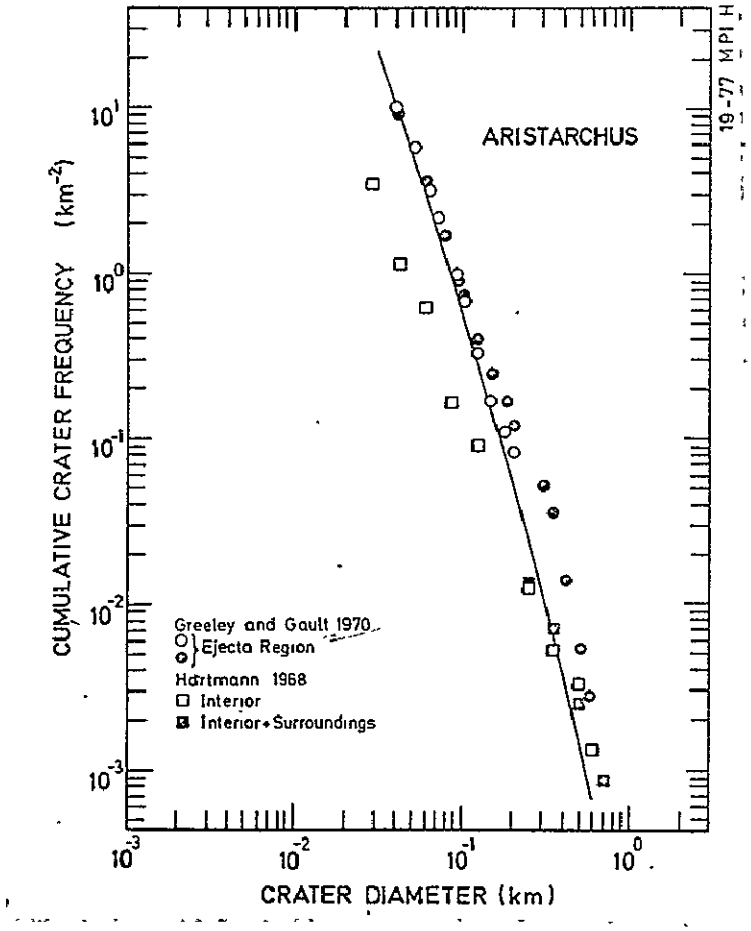

Figure 16. Measurements on structures of the Aristarchus crater: Comparison of the results of this work (solid curve) with the results of other authors.

ORIGINAL PAGE IS
OF POOR QUALITY

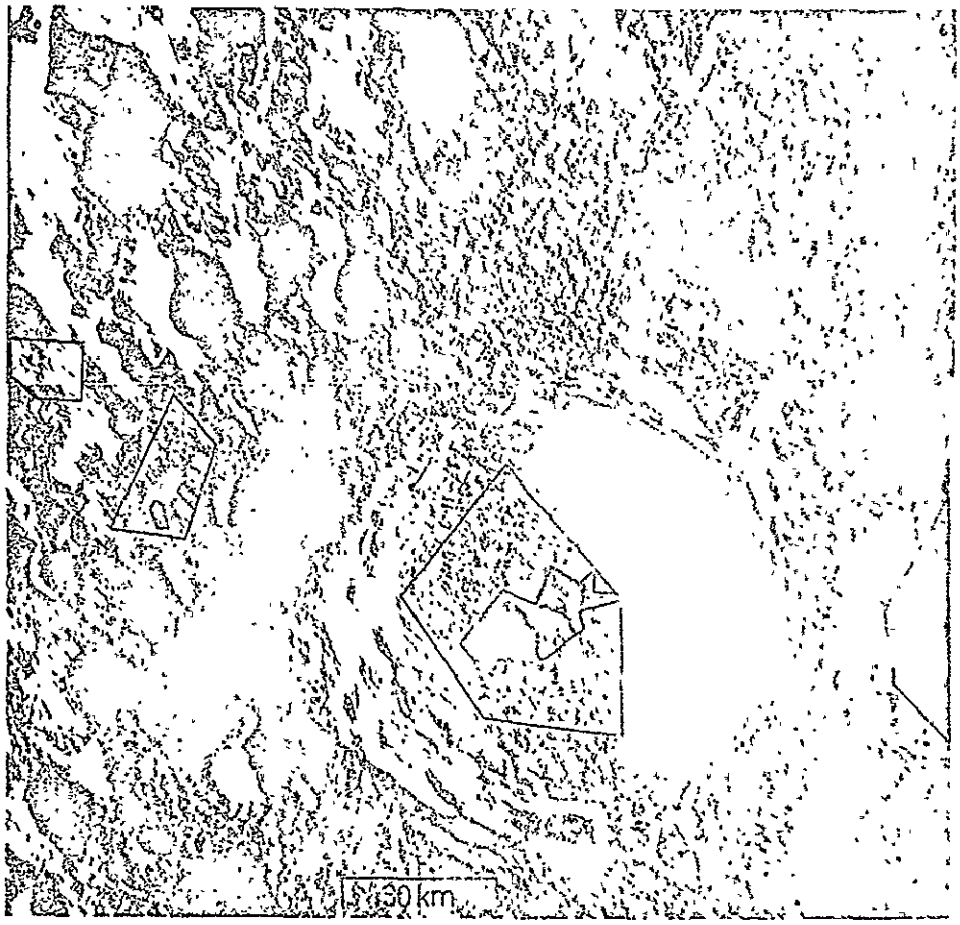

Figure 17. Measurement regions in the interior and on the continuous ejecta cover of the crater Tycho (photomosaic from LO V 125 M and 128 M).

A series of measurements was performed on the continuous ejecta cover. On the one hand, a sufficient number of craters had to be measured, yet on the other hand, the regions had to be as homogeneous as possible. Therefore, measurements could not be performed on the flow structures which originated from rubble streams (Strom and Fielder, 1968). The test regions selected according to these criteria are shown in Figures 17, 18a and b. In order to determine crater frequencies as precisely as possible, numerous shaded zones distinguished by a coarse relief from the overall surface were used. / 24

An additional measurement was performed (Figure 19) on the discontinuous ejecta cover which (in spite of a large statistical error) nevertheless agreed with the crater size distribution determined for the continuous ejecta cover, just as does the data from the crater interior. This is shown in Figure 20. There, the distribution measured on the structures of Tycho can be seen where D = 1 kilometer, an integral crater frequency of $(6.0 \pm 1.7) \times 10^{-5}$ km^{-2} results. Overall the crater size distribution could be measured over the diameter range of more than one order of magnitude.

In Figure 21 the empirical data of Strom and Fielder (1968) and Hartmann (1968) are entered. For comparison, the distribution curve which was derived from the empirical distributions determined in this work (see Figure 20) is entered. Although the data of Strom and Fielder shows good correlation with our own measurements, the measurements of Hartmann deviate; this author probably also measured pre-Tycho or secondary craters.

e) North-Ray

North Ray (D ≈ 900 m), which is shown in Figure 22, is a more recent crater which is in the vicinity of the Apollo 16 landing site. It was thus dated very precisely and provides important data for the determination of the chronology of the flux of

impact bodies in recent times. Investigations of rock samples taken from there showed radiation ages of ≈ 49 million years (Marti, et al., 1973; Drozd, et al., 1974). Superimposed craters were measured on the ejecta cover of North Ray. In Figure 23, the empirical data and, for comparison, the data of Boyce (1976) are entered on crater size distributions determined from rectified panorama photographs. A correlation within the limits of error results. For D = 1 km the integral crater frequency is $(3.9 \pm 1.0) \times 10^{-5} km^{-2}$.

/25

ORIGINAL PAGE IS
OF POOR QUALITY

...AL PAGE IS
OF POOR QUALITY

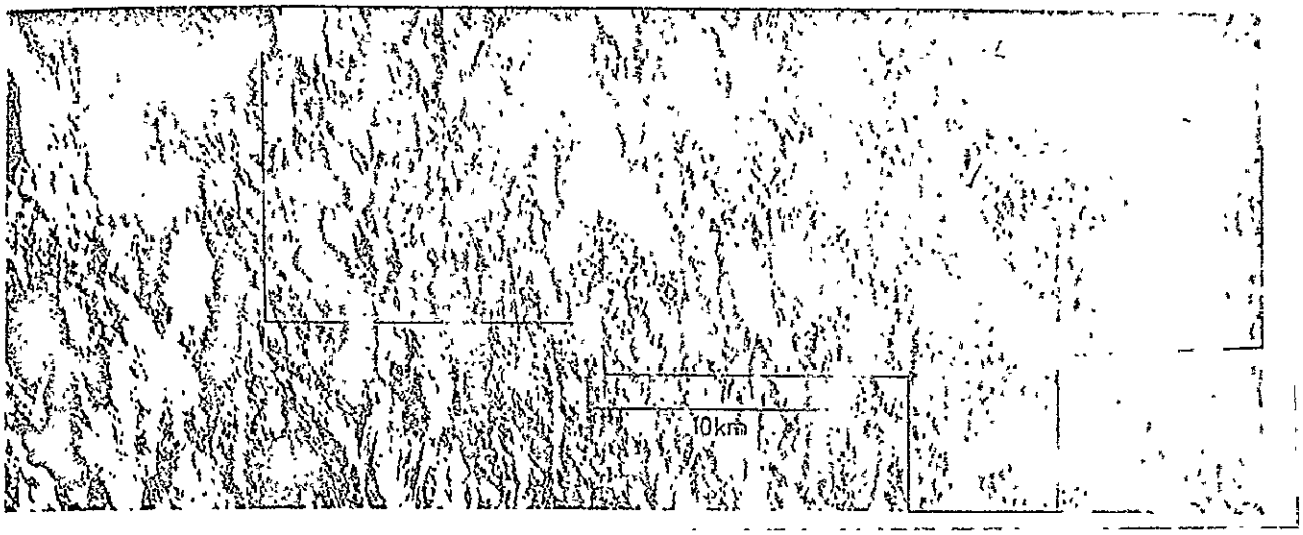

Figures 18a and b. Measured regions of the continuous ejecta cover of the Tycho crater.

a) Photomosaic from LO V 128 H1 and 128 H2.

b) Photomosaic from LO V 128 H1.

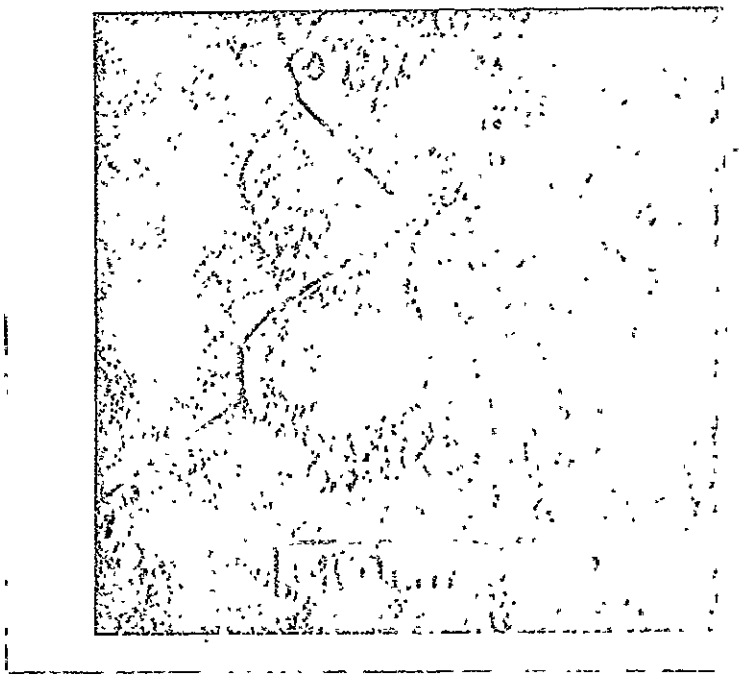

Figure 19. Measurement region on the discontinuous ejecta cover of the crater Tycho (LO V 112 H2).

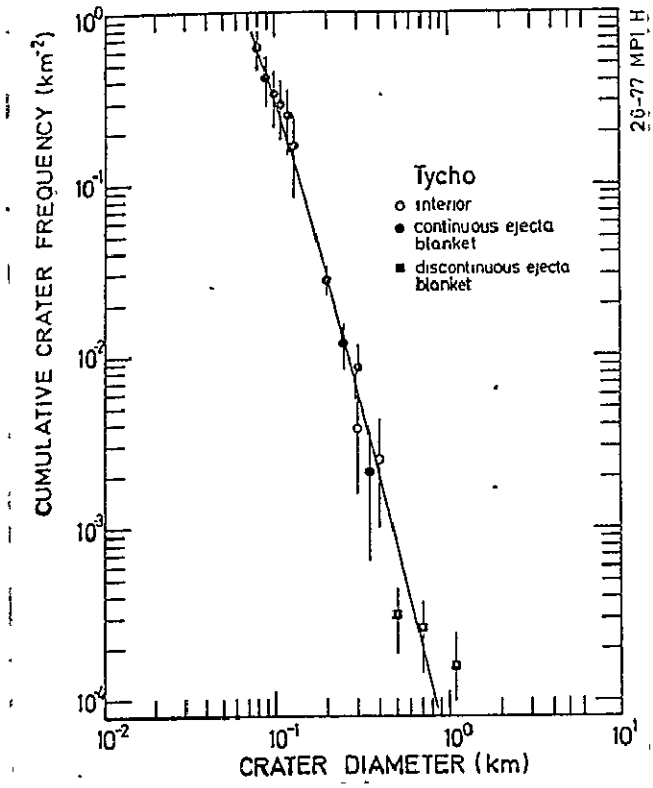

ORIGINAL PAGE IS
OF POOR QUALITY

Figure 20. Crater size distributions measured on the crater interior on the continuous and discontinuous ejecta blanket of Tycho.

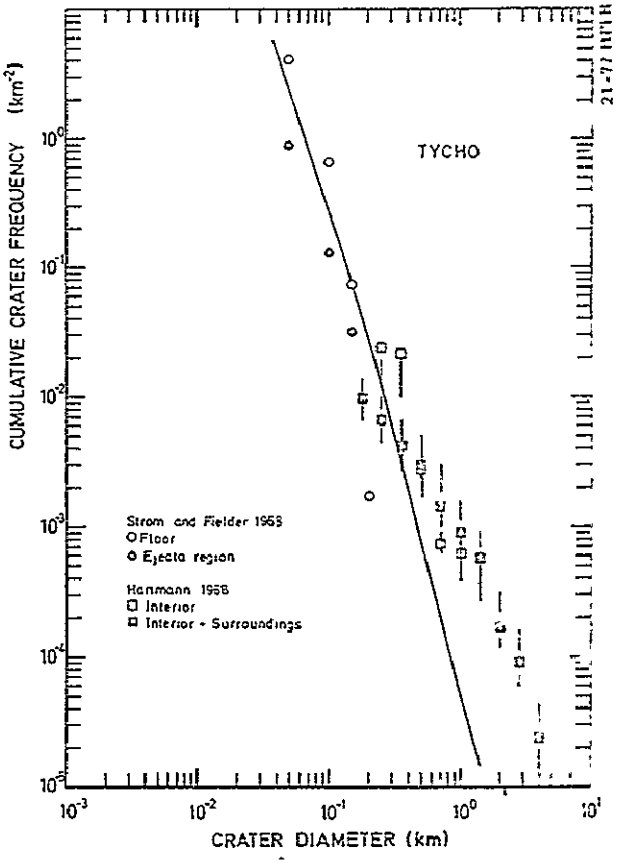

Figure 21. Measurements on structures of the crater Tycho. Comparison of the results of this work (solid curve) with the results of other authors.

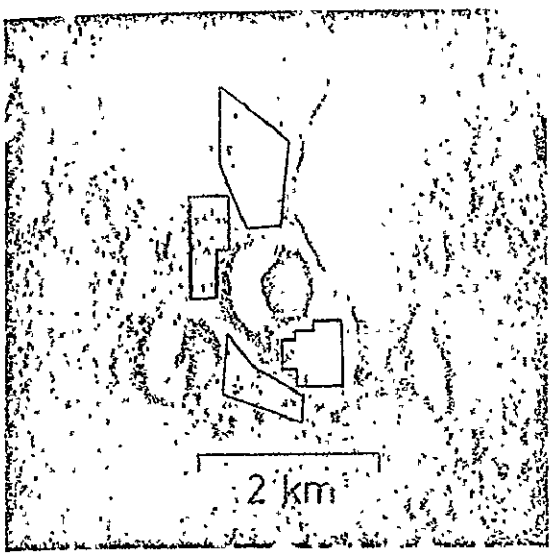

Figure 22. Test regions on the ejecta covers of the North Ray crater (P16-4558).

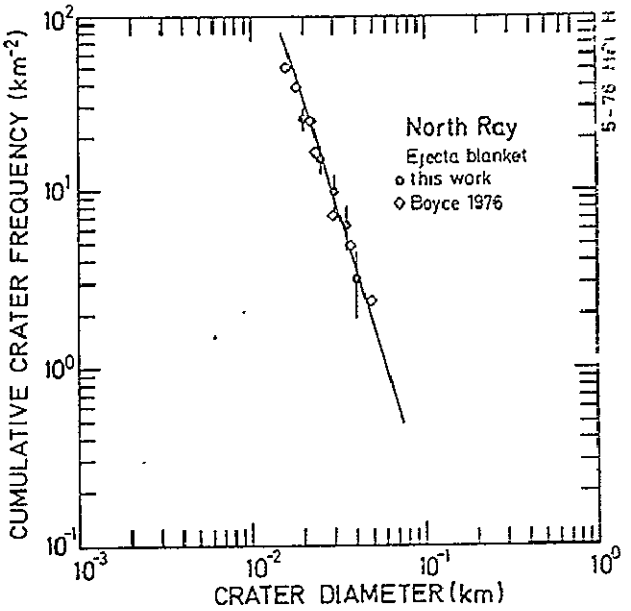

Figure 23. Crater size distribution measured on the ejecta cover of North Ray. The general crater size distribution curve is drawn through the data and the empirical values of Boyce (1976) are entered for comparison.

ORIGINAL PAGE IS
OF POOR QUALITY

III.-2.-Structures produced by ejecta /27

It is interesting to assign the secondary structures formed by ejecta to the corresponding primary craters. This is the case for example, for the light mantle and the central cluster regions in the Taurus Littrow valley. Their relationship with Tycho is discussed in Section b.

A criteria which permits the assignment of secondary crater groups to their primary crater is the finding that the often typical V-shaped structures for secondary craters point to the primary craters (Oberbeck and Morrison, 1973). If the clusters are a great distance away, identification of the primary crater is often not possible. Then, morphological and erosion criteria can be considered (see for example, Arvidson, et al., 1976). Below we will illustrate a method which permits reliable assignment to primary craters when used together with other criteria. In this, we begin from the fact that the regions of an impact crater and its secondary structures have been exposed equally long to the bombardment of meteorites and thus the same number of craters per surface unit have originated since their formation (statistically). /28

The frequencies standardized for the surface of the primary craters with superimposed secondary structures should therefore approximately agree with the crater densities in the regions of the impact crater. Thereupon, dating of a secondary structure by the frequency method provides an age for the primary crater itself.

a) Secondary crater cluster of Copernicus

First we shall test whether the method can be utilized for practical dating of secondary structures. For this, a crater cluster was selected which lies in the vicinity of Copernicus CD

and which was definitely formed by ejecta from Copernicus.

Using pictures of average and high resolution, measurements were performed on a series of surfaces which lay on the ejecta plane produced by these secondary craters (Figures 24 a, b). The craters on this type of terrain proved to be very heavily eroded and thus their measurements had to be performed with great care. Otherwise, we have a result of too few crater frequencies. Therefore, it is advantageous to use only the largest craters for dating since these have been less influenced by erosion effects. Figure 9 shows that within the range of validity, the distribution on the cluster terrain agrees with that obtained for structures of Copernicus.

b) Central cluster and light mantle region for the Apollo 17 landing site.

In the vicinity of the Apollo 17 landing site there are structures — the light mantle and the central cluster region (see Figure 25) — whose origin is attributed to the secondary impact of Tycho ejecta (Howard, 1973; Muehlberger, et al., 1973; Lucchitta, 1975; Wolfe, et al., 1975; Arvidson, et al., 1976).

Investigations previously performed were based primarily on the study of V-formations, the comparison with known secondary structures of Tycho, and morphologic criteria.

The assignment of these regions to the crater Tycho was checked in this work by using the crater frequency dating method (see also Section a). Craters superimposed on the light mantle and the central cluster region were measured. It turned out, just as for the cluster region of Copernicus, that the erosion of this target material is greater than on other regions (see Lucchitta and Sanchez, 1975). On the basis of the high quality

photographic material and the young test surface, sufficiently reliable measurements were performed which yielded identical crater frequencies for both regions, Light Mantle and Central Cluster. In the comparison of these data with Tycho values, the empirical results of the two regions were summarized. The resulting test distributions of the Apollo 17 measurements is illustrated in Figure 26 together with the data from Tycho. Where $D < 50$ m, variations appear in the crater frequency distribution. These are attributable to the fact that on the one hand, not all small craters in the measurement region were detected (erosion) and on the other hand, for craters of diameter $D < 30$ m, contamination by secondary craters seems to play a role (see Figure 35). -As Figure 26 shows, the measured distributions of regions in the Taurus Littrow valley agree with the overlapping diameter /29
range of Tycho. Under consideration of the experimental test results discussed in Section a, we can proceed from the fact /30
that the Light Mantle region and the Central Cluster region very probably occurred due to Tycho ejecta. Neukum and König (1976) arrived at a similar result on the basis of previous investigations. /31
Detailed examinations of the radiation age of Apollo 17 samples (Arvidson, et al., 1976) produced a value of 96 ± 5 million years for the Light Mantle and the Central Cluster region. This can therefore be considered the absolute age of the Tycho crater. In addition, one can determine the absolute age of Tycho by another method. Here we begin from the relative integral crater frequencies of Tycho and North Ray, their radiometric dating, and the flux of impact bodies. Under the assumption of constant flow (see Section III. 3b) there results a value of about 75 million years for its age. Since the determination of crater frequency and even the flux of meteorites are full of uncertainties, this result is compatible with the radiometric age.

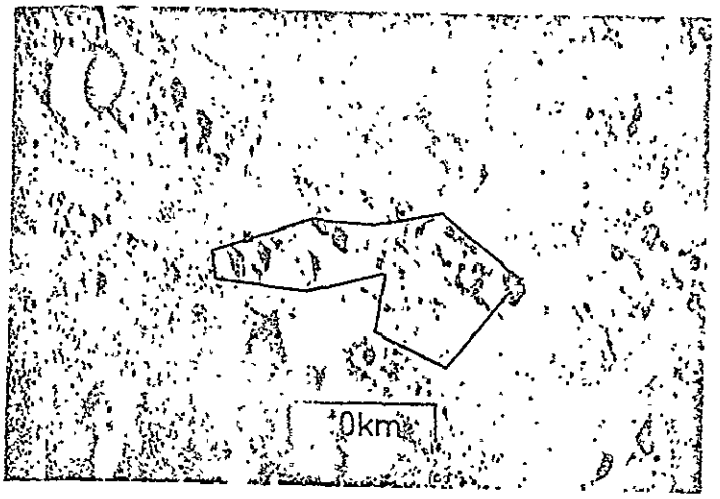

ORIGINAL PAGE IS
OF POOR QUALITY

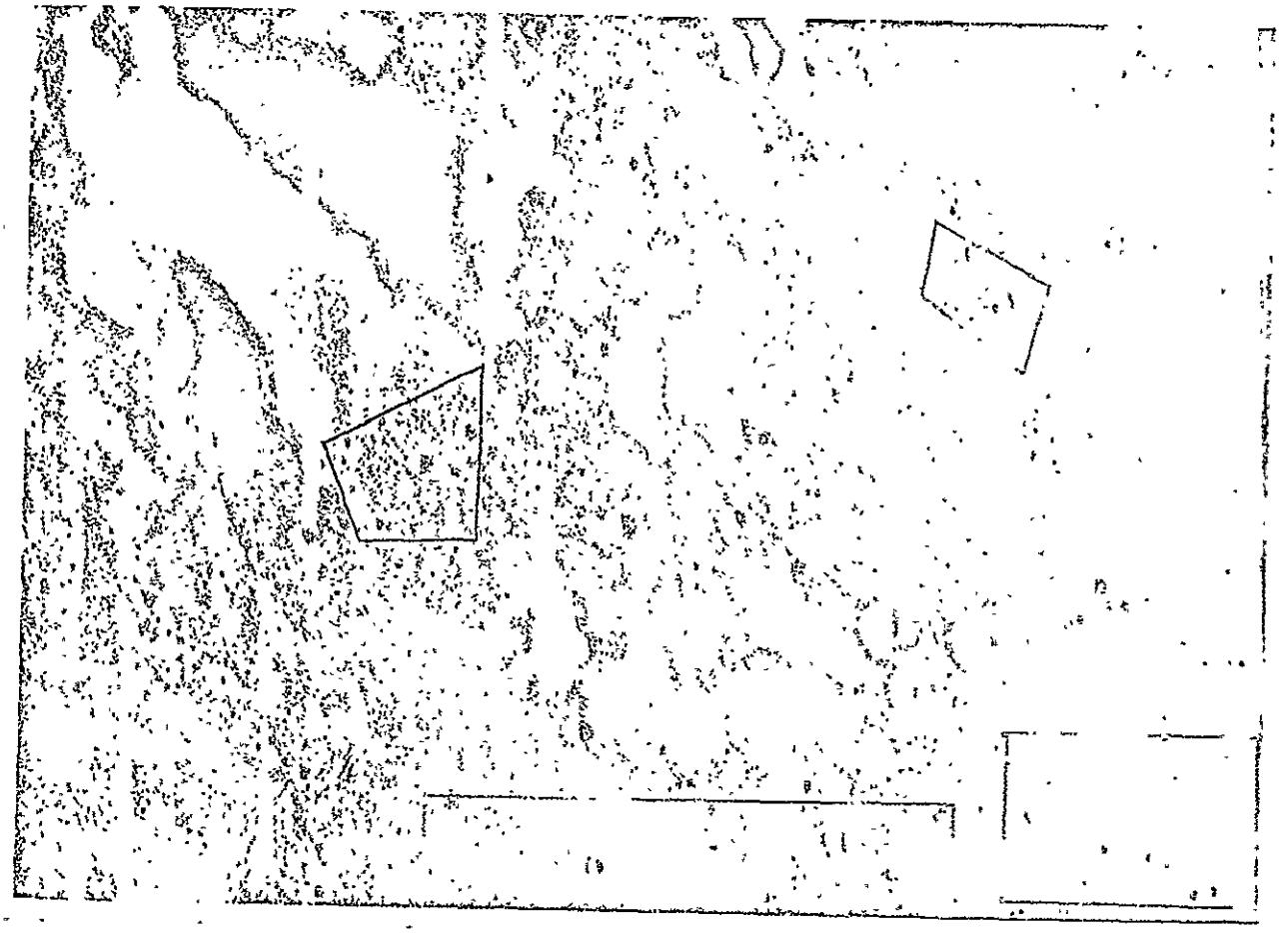

Figures 24a and b. Measurement region on the ejecta region of a secondary cluster of Copernicus.

(a) LO V 137M (b) LO V 137H2.

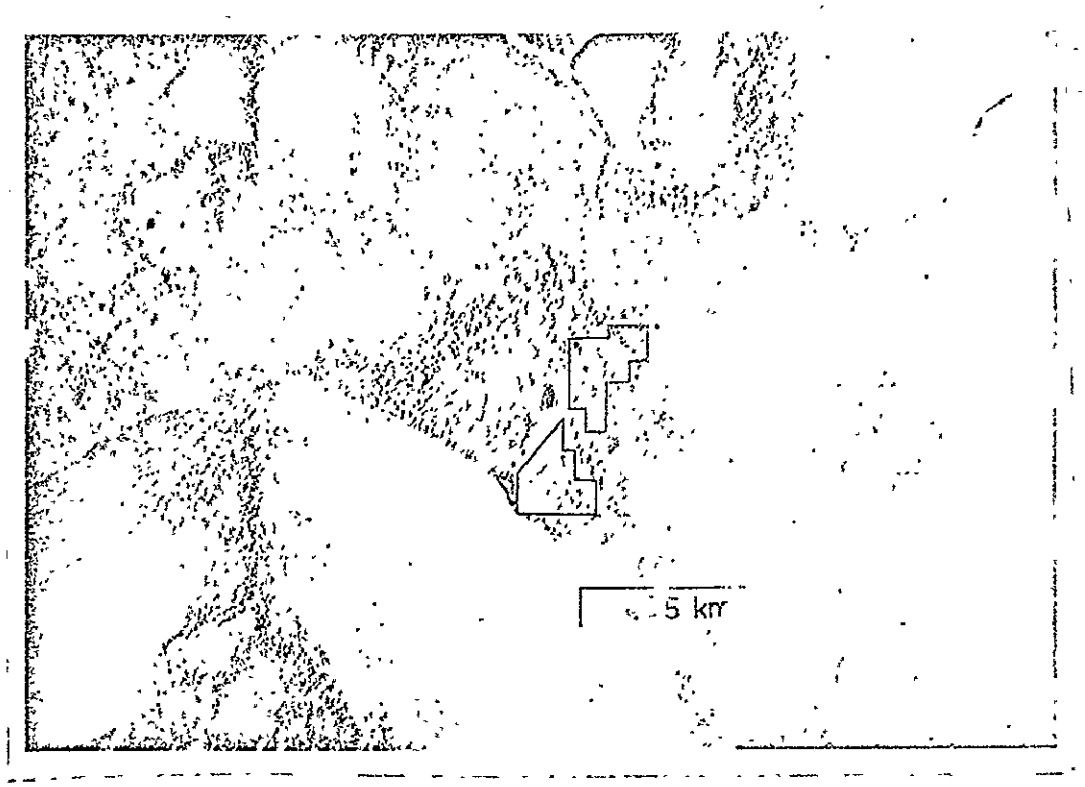

Figure 25. Surroundings of the Apollo 17 landing site in the Taurus Littrow valley. The measurement surfaces in the Light Mantle region (left) and in the Central Cluster region (right) are included (P-17-2309)..

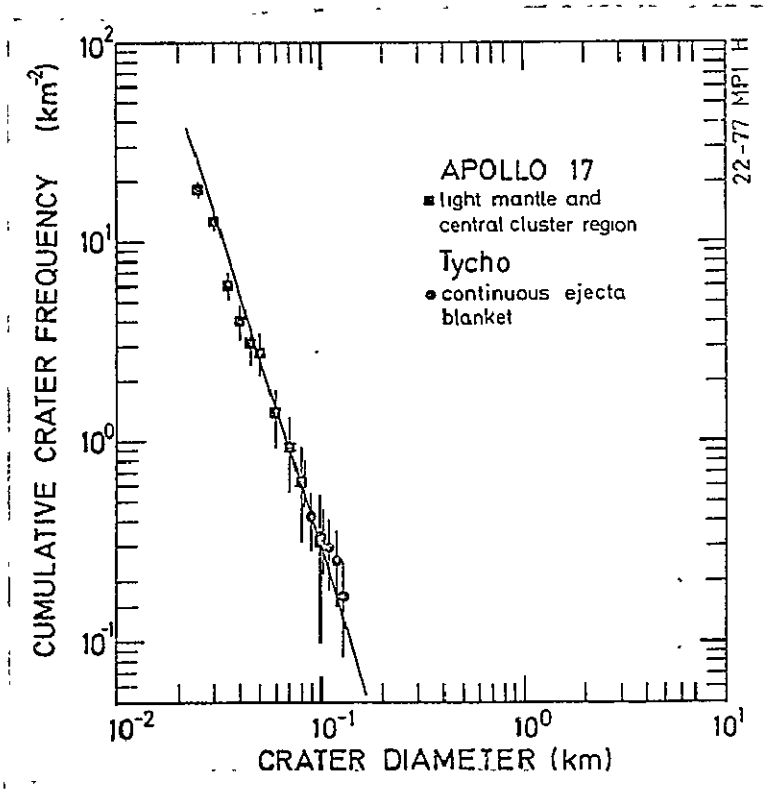

ORIGINAL PAGE IS
OF POOR QUALITY

Figure 26. Comparison of the Crater frequency distribution measured on the crater Tycho (solid line) and the structures in the Taurus Littrow valley (Light Mantle and Central Cluster region).

III. 3 DISCUSSION

a) Morphologic - stratographic classifications

The investigations discussed in Section 1 produced the following age sequence for the impact craters (from oldest to youngest): Copernicus, Kepler, Aristarchus, Tycho and North Ray. Except for North Ray, these impact structures have been dated relatively on the basis of morphologic-stratographic criteria (Hackman, 1962; Pohn and Offield, 1970; Wilhelms and McCauley, 1971). The resulting classifications agree with the results of this work.

The dating of large impact structures by means of the frequency of craters superimposed on them can, in principle, be used for every larger crater provided it is not too heavily eroded or covered by secondary craters. With this method a series of additional post-Mare impact craters were examined and their morphologic-stratographic classifications were checked. Previous results of these studies have been published somewhat (Neukum and König, 1976) and are here summarized briefly: for recent structures, as those investigated here, consistent results were obtained. Older craters, however, are frequently classified as being too young because the morphologic modification of a crater depends not only on its age, but also on its size: erosion effects change the appearance of a small crater much more than that of a large crater. Therefore, the morphologic classification tends to classify larger craters as more recent. Although attempts were made to include this effect (Offield and Pohn, 1970), apparently the size-dependence of the classification — particularly in the range of crater diameter $D > 8$ km — was accounted for only insufficiently.

/3

b) Chronology of the flux of impact bodies

The time course of the flux of impact bodies near the Earth more than three billion years ago is distinguished by an exponential decrease of $T_{1/2}$ = 140 million years (Neukum, et al., 1975a). Beginning from the crater frequencies determined in this work, the chronology of the flux — particularly during the past (1-3) x 10^9 years — can be determined more precisely than before (Neukum and König, 1976). Results from the crater size distributions on the Canadian shield* and the Apollo 12 and Apollo 15 landing sites** were also used for this.

The integral frequencies (for D = 1 km) of these objects compared to the corresponding radiometric age of the target surfaces are shown in Figure 27. Beginning from the data which were obtained for North Ray and whose assignment to a radiometric age is relatively reliable, integral crater frequencies were calculated under the assumption that the flux in the last 3 x 10^9 years had decreased exponentially. Here different half-life periods $T_{1/2}$ were considered ($T_{1/2} = \infty$ corresponds to constant flux). As we can see from Figure 27, a constant flux during the last 3 x 10^9 years reproduces the data obtained for North Ray, Tycho and the Apollo 12 and 15 landing sites quite well. A decreasing flow where $T_{1/2}$ = (100-200) million years during the last $\sim$ 800 million years, which was considered possible by Neukum and König (1976) can be excluded.

If one includes the data of the Canadian shield and that of the Copernicus Crater, then a time variation of the meteorite

---

* If we assume v_∞ = 15 km/s for data reduced to lunar conditions (see Neukum, et al., 1975a).

** Data taken from Neukum, et al., (1975a).

flux during the last 1 x 10^9 years is indicated. So for example, a flux during the last 1 x 10^9 years with a half-life time of about (0.5 - 1.0) x 10^9 years which has decreased exponentially, is compatible with the data. Even complicated models of flux chronology are possible (see Baldwin, 1971; Neukum, et al., 1975a; Neukum and König, 1976). Thus, for example the flux could have fallen off exponentially about 1 x 10^9 years ago and then increased, followed by a renewed decrease. A minimum impact rate occurring between ≈1 and 3 x 10^9 years ago could explain why no corresponding radiometric sample ages were found except for individual exceptions.

The data for Copernicus and the Canadian shield however should be considered less reliable: neither the geocentric velocities used to convert the Canadian crater to "lunar conditions" of impact body are assured, nor is the relationship between the Apollo 12 samples which were used for the dating of /33
Copernicus and the crater itself certain. Thus for absolute dating, younger lunar impact structures for which no radio-metric dating is available, can proceed from the assumption of a constant flux. Under this condition, there results for Aristarchus an age of (125-175) million years and for Kepler (625-1250) million years. Accordingly, for Copernicus one would obtain an age of (1010 - 1630) million years. If the assignment of the age of /34
Copernicus resulting from radiometric measurements of Apollo 12 samples is correct (i.e., if the flux was not constant) then the age of the younger crater Kepler would be limited to the range of (625-950) million years.

The relative and absolute ages of the craters examined are shown in Table 1.

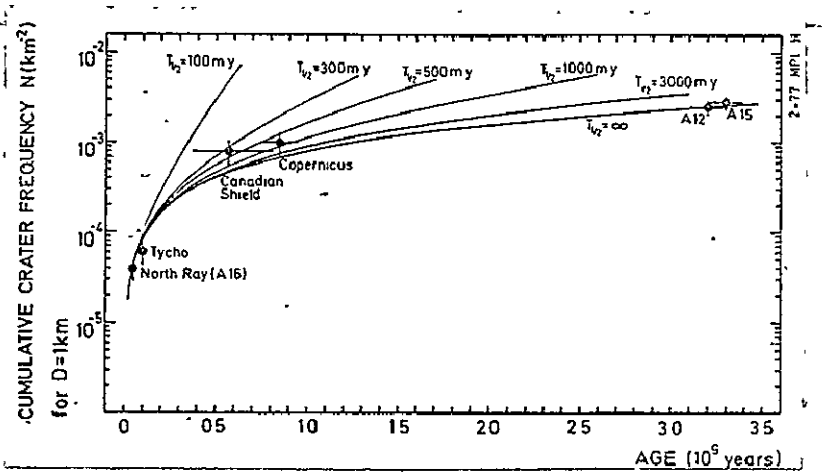

Figure 27. Lunar integral crater frequencies (for D = 1 km) as a function of the target age. The data from the Canadian plate were converted to lunar conditions.

TABLE 1. RELATIVE AND ABSOLUTE AGE OF THE CRATERS EXAMINED.

	Integral crater frequency N (km-2)	Age (10^6 years) (a)	(b)
Copernicus	$(1.0 \pm 0.3) \cdot 10^{-3}$	850 ± 100 (r)	1320 ± 310
Kepler	$(7.5 \pm 2.5) \cdot 10^{-4}$	790 ± 160	940 ± 310
Aristarchus	$(1.2 \pm 0.2) \cdot 10^{-4}$	150 ± 25	150 ± 25
Tycho	$(6.0 \pm 1.7) \cdot 10^{-5}$	96 ± 5 (r)	75 ± 20
North Ray	$(3.9 \pm 1.0) \cdot 10^{-5}$	48.9 ± 1.7 (r)	—

(a) Dating on the basis of the flux sequence considers the assignment of the radiometric crater age (r)

(b) Ages calculated under the assumption of a constant flux; there the radiometric age of North Ray was used as a calibration point.

Beginning from the known lunar impact rate for the last 10^9 years and the time constants of the crater size distribution, it is possible to determine the integral size distribution or the influx of interplanetary bodies of diameters of $10^{-4}\,m \lesssim d \lesssim 10^3\,m$ in the Earth-Moon vicinity during recent times. The data for particles having diameters in the μm- to the cm-range were obtained from investigations on lunar microcraters (Fechtig, et al., 1974) and meteor observations (Hawkins and Upton, 1958; Lundblad, 1967). For the range of $0.5\,m \lesssim d \lesssim 600\,m$, the size distribution of lunar craters was used. The determination of projectile diameter d from the crater diameter D is performed by relations of Hartmann (1965): $d = a\,\rho^{-k}\,D^{1.02}$, , where $k = 1/3.06$, the parameter "a" is a function of the impact velocity and ρ is the density of the projectile material. The inaccuracies in the quantities k and "a" are considered in the citations of error. The corresponding particle influx rates were determined under the assumption of constant flux, from the crater frequencies N and the radiometric crater ages t_i of North Ray and Tycho; the crater production rate ϕ was determined:

$\phi(D) = N(D, t_i)/t_i$. Two large crater diameters were extrapolated over the distribution curve. For the reduction of data of terrestrial craters (Canadian shield) the crater and target ages were considered (Neukum, et al., 1975a). The conversion of crater data occurs for projectile velocities $V_\infty = (10\text{-}20)$ km/s. In addition, an asteroid influx point calculated by Shoemaker and Helin (1976) for the Earth was used. The different gravitational field capture cross sections due to different gravity on the Moon and Earth were considered in the determination of influx values.

In Figure 28 the integral influx values per $m^2 10^6$ years are plotted against the corresponding particle diameters. The low data range of the influx curve is distinguished by dotted lines. The distribution curve of particle sizes exhibits regions — like

the distribution function of crater diameter — which show a nearly constant slope. This indicates that the impact bodies belong to populations which originated by the most different means; fragments of collisions of asteroids with other asteroids or with other heavenly bodies, or of origin on a comet. The asteroid point is somewhat high with respect to the lunar crater data. Note here that the diameter determinations used by Shoemaker and Helin are an average of about 50% higher than the values determined by other researchers (see Wetherill, 1976). Therefore, the asteroid influx point is uncertain.

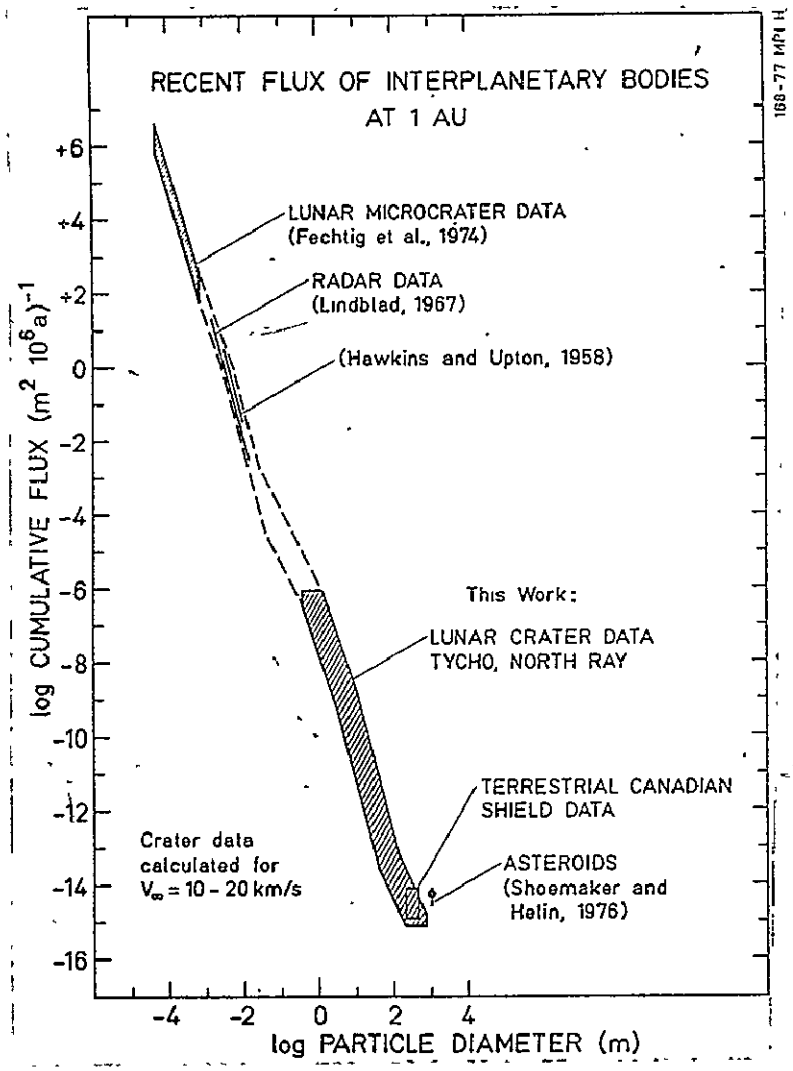

Figure 28. Integral flux of interplanetary bodies in an Earth-Moon system as a function of the particle size. The crater diameters were converted into projectile diameters.

IV. SECONDARY CRATERS ON THE MOON

/36

With the formation of impact craters, we always have the ejection of material called ejecta. This ejecta again produces craters or so-called secondary craters. On the Moon, their impact velocities are less than the flight velocity of 2.4 km/s. Large, fresh, impact structures are surrounded by pronounced systems of bright rays which are arranged either radially or tangentially to the edge of the initial crater and are connected genetically with the secondary craters (Oberbeck, 1871). Within the rays there are a series of crater chains which are produced by the impact of ejects (see Shoemaker, 1960). One such chain to the southeast of the Aristarchus crater is shown in Figure 29 (at different scales). As can be seen in Figure 29b, the secondary craters are distinguished from the primary craters because of their morphology, by a somewhat elliptical shape, lower crater depths, V-shaped structures and by their appearance in groups (Oberbeck and Morrison, 1973). These structures are eroded with increasing age and lose their relief in the course of time. Besides these secondary craters arranged in chains, there are disperse groups of round secondary craters (see Shoemaker, 1965), which are called clusters. They originate due to a form of ejecta particles with very similar flight paths (Shoemaker, 1965). Consequently, the impact velocities of ejecta particles which have produced a secondary crater cluster have not been very different. The impact angles were probably very steep since these craters are round. It is generally difficult to assign these structures to a primary crater.

IV. 1 Size distribution

/37

The secondary craters of younger impact structures are especially suitable for investigation since they are relatively little eroded. Below, measurements are discussed which were performed on the crater chains of Aristarchus. Kepler and

ORIGINAL PAGE
OF POOR QUALI

(a)

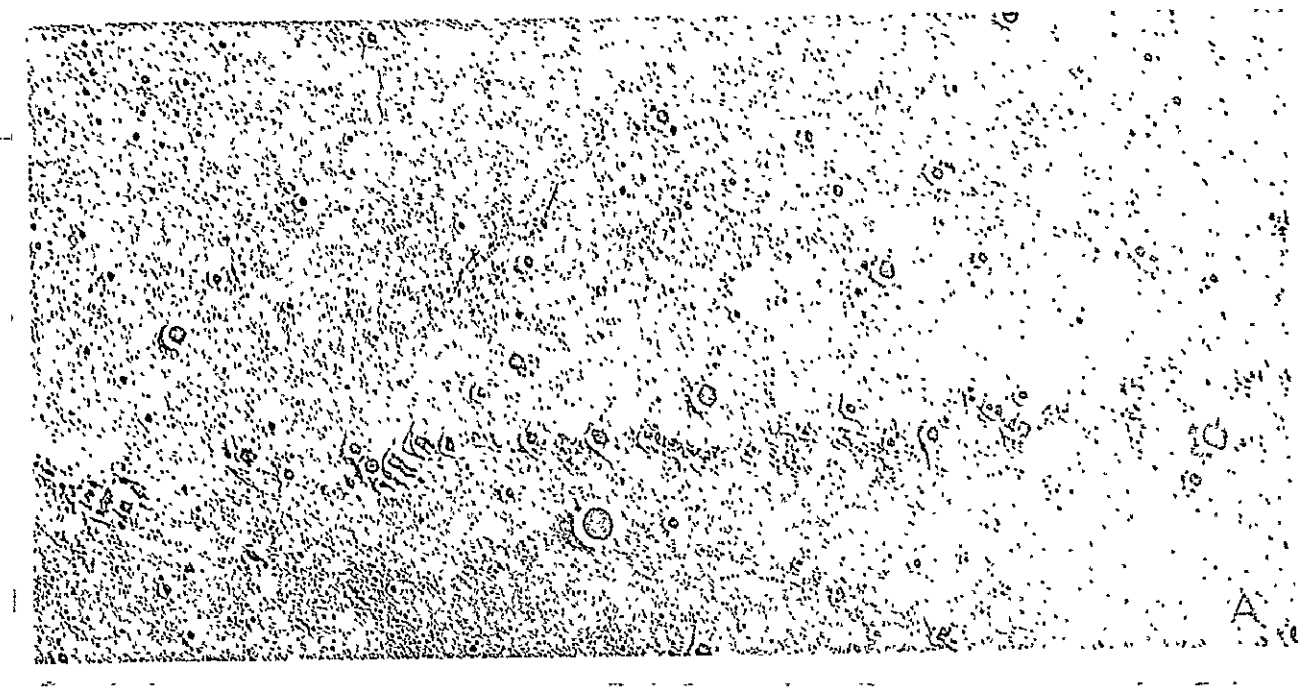

(b)

Figure 29 a and b. Ejecta region of the Aristarchus crater.

(a) Part of the bright ray system. Photo mosaic from LO IV 150H3 and 151H1.

(b) Section of a ray, which shows a part of the secondary crater chain. (AS 17-2930).

Copernicus* and on clusters in the vicinity of Aristarchus and Copernicus. In order to keep saturation effects from falsifying the crater size distribution (i.e., mutual blanketing or craters impacting the same spot) only those chains and cluster structures were investigated which exhibited a relatively low crater density. The investigations were performed in the diameter range of 250 m $\leq$ D $\leq$ 3500 m.

a) Empirical principle and evaluation

To measure the secondary craters, the same photographic material was used as already introduced in Chapter II 1a.

The distance of the secondary crater from the primary crater center was between 60 and 280 km (Aristarchus), at about 600 km (Kepler) and between 140 and 480 km (Copernicus). The secondary crater chain in Figure 29 was divided for the measurement into /38
sections, each of a primary crater radius length in order to be able to determine any variations with distance from the center of Aristarchus. Only the unequivocally identifiable craters connected with V-structures were included in the chain.

Figure 30 shows four of the examined clusters. All craters within the measurement surface delineated by the lines were included in the investigations.

Four points on the crater edge were measured. This was done, on the one hand, because the secondary structures, particularly those in the chains, are often not circular but elliptical; on the other hand, these craters often have an incomplete edge due to the

*. Partial use was made of the investigations of Oberbeck and Morrison (1973) in the identification of appropriate primary craters.

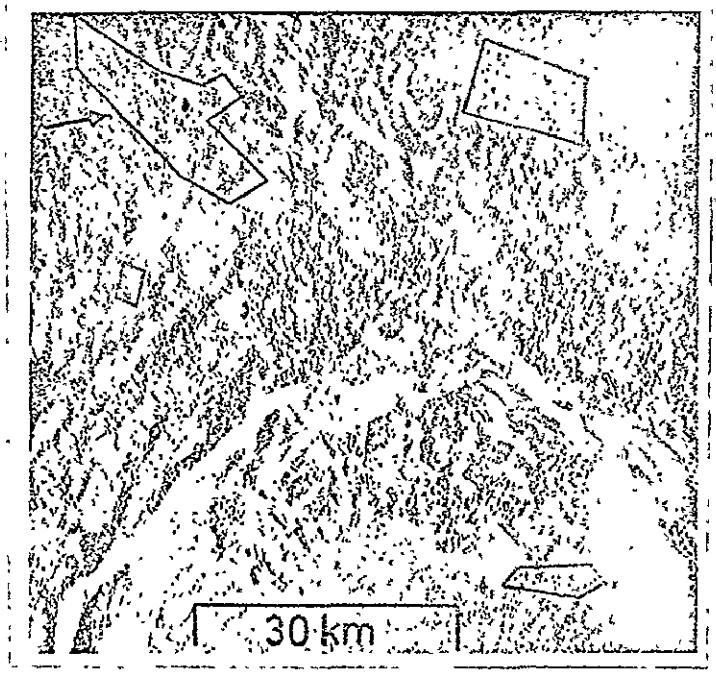

ORIGINAL PAGE IS
OF POOR QUALITY

Figure 30. Investigated cluster of secondary craters on Copernicus (LO V 157M).

subsequent impacts of nearby meteorites. The average diameter of the secondary craters was determined by drawing a calculated circle through the four measured crater edge points after the determination processes. The final evaluation was performed as in Section II 1b and c.

b) Results

Figures 31a and b show the integral size distribution of secondary craters in a section of a chain (in 11-12 crater radii distance) of Aristarchus (see Figure 29) and in a cluster, which is distinguished by an arrow in Figure 30. The shape of the distribution curves suggests a classification into two diameter intervals in which the data can be approximated by straight log-log diagrams. It was found that the measured size distributions of the secondary craters in clusters and chains follow a percentage

law in the range of small diameter of the form $N \sim D^{-\alpha}$ ($\alpha = 2.5 \pm 0.3$) and in the range of larger craters a percentage law $N \sim D^{-\beta}$ ($\beta = 4 \pm 1$). From the similarities of the size distribution in secondary crater chains and clusters, one can conclude that the ejecta producing them originate in the primary crater formation by the same process. The transition between the flat and the steep branch of the distribution curve appears constant as shown in Figure 31. In this transition zone, we can define at about a breakoff point D_A: the data of the crater of diameters $D < D_A$ lie on the flat branch of the distribution curve, the value where $D > D_A$ lie on the steep branch. Between the point D_A of a secondary crater distribution and the current largest crater diameter $\boxed{D^s_{max}}$ of a crater group there exists an equation. The correlation of these quantities is shown in Figure 32 where the D_A is plotted against the appropriate $\boxed{D^s_{max}}$ - values. From this one can see that at about 0.7 times the greatest craters D^s_{max}, the distribution curves of the secondary craters bend into the flat branch. /40

If one compares the size of a secondary crater in the Copernicus and Aristarchus -chain (Figure 32), then one sees that the larter crater Copernicus in general also produced larger secondary craters. This correlation between primary crater size and average secondary crater diameter was observed even in the investigations of chain craters of other primary crater distribution fields. However, no correlation of the average standard crater size could be ascertained in the chains with the distance from the primary crater.

It is probable that for the average diameter of a secondary crater in clusters, analogous equations exist as for the chain craters. However, these structures were formed by ejecta which itself was created in a similar manner. But since the assignment of clusters to primary craters is often not unequivocal, the relations in this case cannot be checked.

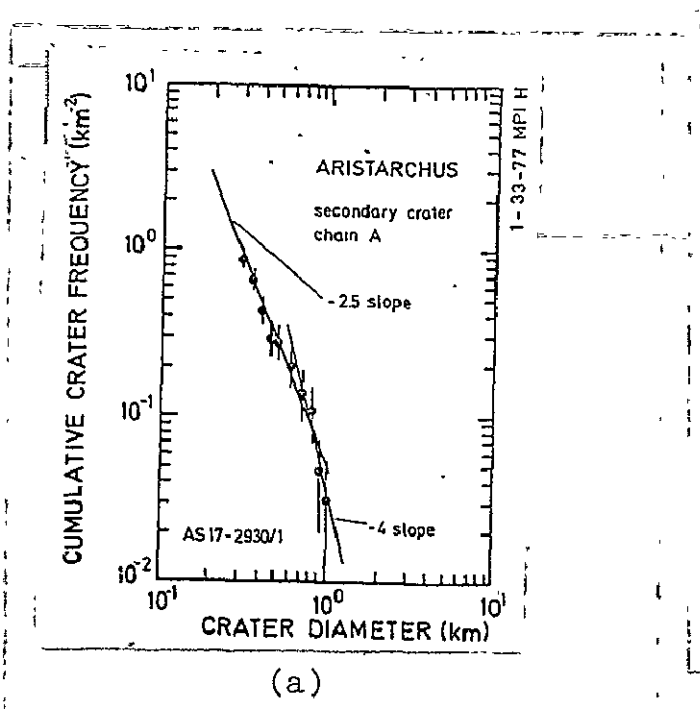

(a)

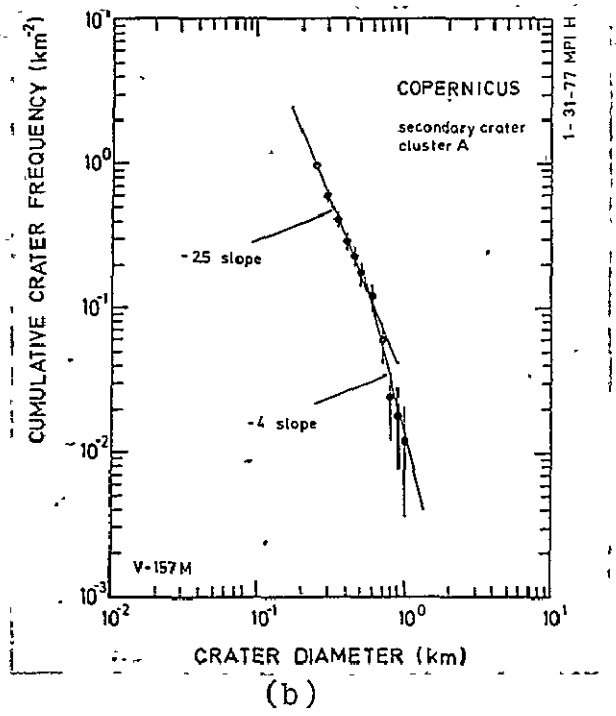

(b)

Figures 31a and b: Integral size distribution of secondary craters:

a) In a section (in 11-12 crater radii distance) of the chain shown in Figure 29 which lies in a ray of the Aristarchus crater.

b) Of a cluster on the continuous ejecta cover of the Copernicus crater which is distinguished by an arrow in Figure 30.

Two straight lines of slope -2.5 and -4 (in the log-log plot) are plotted by the measurement distributions.

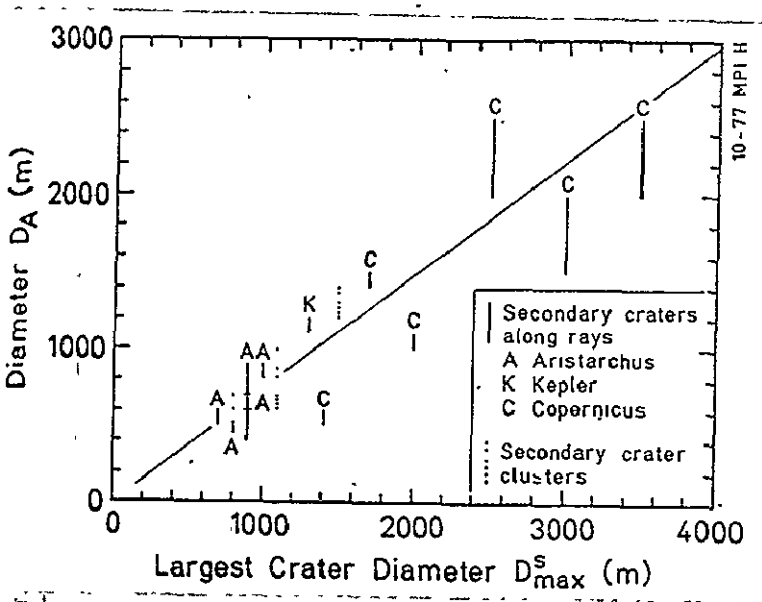

Figure 32. Correlation between the diameter D_A and the current greatest diameter D^s_{max} of a secondary crater group.

IV. 2 Discussion

It was prviously assumed that the integral size distribution of secondary craters follow a percentage law of constant exponents -3.5 (Soderblom, et al., 1974) to -4 (Shoemaker, 1965). The flattening off of the distribution curve at smaller crater diameters was previously not observed. In the investigation of secondary craters which were formed by ejecta of the Sedan explosion crater, Shoemaker noted (1965) a bending in the size distribution but did not attribute this to an effect which was caused by the evaluation: the smaller secondary craters lay closely packed above the resolution limit of the photographs used and could therefore not be completely registered. /41

For the size distributions measured in this work the bending occurs in diameter ranges where quantitative measurements were made.

The destruction of smaller craters either by erosion or by subsequent formation of larger craters at a higher surface density of impact also causes a flattening off of the crater size distribution at smaller diameters. A significant influence of this process on the measured size distributions, however, is not possible.

- If erosion effects were significant, the size distribution of equally old secondary crater groups which lie along the same target material would have to bend off at the same diameters D_A. But this was not observed on the secondary crater chains found on Mare material, e.g., for example, on Copernicus (see Figure 32).

- Although the crater densities in the examined secondary crater groups in the range of $D < D_A$ lie near the frequency values,

the populations are in equilibrium in the creation-destruction cycle, however, in this range the exponents of the measured size distributions (about -2.5) are different from those of the equilibrium distribution (Exponent -2).

The results of this work show that the size distribution of the secondary craters can be described by a power law having diameter dependent exponents. The previously assumed power law for a constant exponent between -3.5 and -4 does not hold for the range of small crater diameter.

As already discussed, the velocity differences between the ejecta particles which have formed a cluster or a certain section of a secondary crater chain could not have been very large. According to the generally recognized scaling, the ratio of projectile diameter to the corresponding crater diameters is nearly constant at the same projectile velocities (see for example, Hartmann, 1965). This means that the measured secondary crater size distribution directly reflects the size distributions of the ejecta.

IV. 3 Comparison with the primary crater size distribution

The average impact velocity of meteorites on the surface of the Moon is about 15 km/s (Öpik, 1962). The velocities of the ejecta particles forming secondary craters is always less than the Moon impact velocity by 2.4 km/s. Therefore, a /42
meteorite produces on its impact on the Moon's surface, a minimum crater 3 times larger than one produced by an ejecta particle of the same mass. In order to be able to directly compare the crater size distributions of meteorites and ejecta, a velocity correction must be made. This is described as follows.

Between the diameter D of a crater and the energy E necessary for its formation, there is an equation $D \sim E^{k}$ which was determined on the basis of explosion experiments (e.g., Baldwin, 1963).

For a meteorite impacting at velocity v of mass m, therefore, we have $D \sim (1/2\ mv^2)^k$. For k, a value between 1/3 and 1/3.4 is used (Shoemaker, et al., 1962; Baldwin, 1963; Hartmann, 1965). Thus there results the diameter relationship $\gamma = D_1/D_2$ of the crater which was produced by the same projectiles at different impact velocities v_1 and v_2 to $\gamma = (v_1/v_2)^{2k}$. Since in this chapter examined secondary craters were produced at a minimum velocity of about 350 m/s on the basis of ballistic calculations (Overbeck and Morrison, 1973) there results for the diameter ratio D (secondary)/D (primary) $\approx$ 0.08. A more precise determination of γ is difficult since neither the impact velocities of ejecta nor those of meteorites on the Moon are known precisely.

For direct comparison of the size distribution of ejecta and meteorites, the standard distribution function (see Chapter II) is shown in Figure 33, shifted by a factor of $\gamma = 0.1$ to smaller diameters. For this diameter ratio there results the best possible agreement between two distributions: it turns out that the size distribution of a secondary craters agrees well with those of meteorites for diameters $D \geq D_A$. For diameters $D < D_A$, the ejecta size distribution function deviates from that of the primary impact bodies. This relationship is interpreted as a deficit occurrence: if — as is suggested by previous considerations — the size distribution of ejecta of the meteorites is very similar, then necessarily the size distribution of ejecta at the greater diameters reaches a limit due to the finite primary crater size.

As was also determined in our investigations, a correlation exists between the primary crater diameter and the diameters of its secondary craters (see, for example, Shoemaker, 1965). It generally makes no difference which process causes the primary crater (explosion, impact), so that one finds empirically that in the m-km diameter range, the greatest secondary crater is about ten times smaller than that of the primary crater (see Table 2).

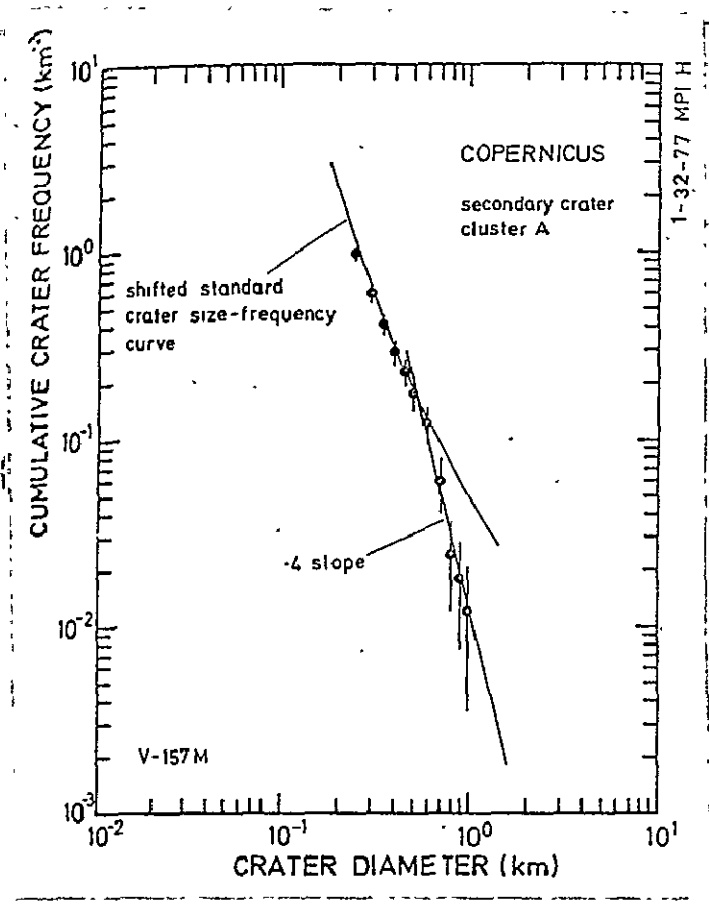

Figure 33. Secondary crater size distribution of a cluster on the continuous ejecta cover of Copernicus. A normal distribution function and a logarithmic line of the slope of -4 is drawn through the data. The standard distribution function was shifted by a factor of 10.

TABLE 2. RATIO OF THE LARTEST SECONDARY CRATER DIAMETER D_E TO THE PRIMARY CRATER DIAMETER D_p FOR LUNAR IMPACT AND TERRESTRIAL EXPLOSION CRATERS (DATA FROM SHOEMAKER, 1965); ROBERTS, 1964).

Crater	Crater type	D_p	D_E/D_p
Scooter	Explosion	104 m	0.12
Sedan	Explosion	366 m	0.08
Copernicus	Impact	92 km	0.09
Langrenus	Impact	132 km	0.05

The relation between the diameter D_A (where the distribution deviates) and the diameter D^2_{max} (of the largest crater of the secondary crater group under consideration) illustrates the deficit occurrence (Figure 32). The size distribution of ejecta deviates from the normal distribution because the size of secondary particles produced cannot be selected due to the primary impact, i.e., a deficit of large ejecta particles must occur. /43

It is conceded that at least some of the meteorites which reach the Earth-Moon system are collision fragments of larger bodies (see, for example, Wetherill, 1976). Therefore, it is not amazing that similarities exist between the size distribution of ejecta particles and of meteorite bodies, however, both types of bodies are created by collision processes. According to Dohnanyi (1969) one expects a power law having the exponent -2.4 for the integral diameter distribution of particles which were formed by collisions. The average secondary crater distributions have a similar exponent except for the deficit part. Since a normal distribution curve is composed of regions having different exponents, very probably the correlation of the ejecta distribution and the size distribution of the primary projectiles is given only for the size range examined.

IV. 4 The influence of secondary craters on primary crater distributions

It is not always possible to perform investigations on regions which meet all the criteria for selection described in Section II a, particularly the condition of minimum secondary crater mixing. Therefore, it is of interest to know in what crater size ranges a significant contamination by secondary craters should be expected, i.e., up to what crater diameter are measurements of primary crater distribution meaningful which will lead to reliable results.

The knowledge of the ejecta size distribution and thus of the size distribution of the secondary craters makes it possible to estimate the influence of intermingled secondary craters on primary crater populations. In Figure 34 the non-shifted primary crater size distribution function is approximated to the empirical data (dashed line). The secondary crater distribution seems to follow in the region of larger diameters, the primary crater distribution and at smaller diameters to bend off flat. The agreement occurs because the deficit branch of the measured secondary crater size distribution falls within the range of the normal distribution function examined in this work. This normal distribution function can be approximated by a power function having the exponent -4. The coincidence can be attributed to the diameter range alone where the measurements used here were performed. As was discussed in the previous section, this coincidence does not occur in the other diameter ranges. Therefore, in general there should result a noticeable contaminated size distribution. Its precise course cannot be predicted since it is dependent on the quantities of surface density and number of secondary crater groups contained.

In order to study this more precisely, different aged old regions were selected ($(0.130 \leq \tau_i \leq 3.5) \cdot 10^9$ years. Secondary craters were knowingly included in the measurement (Figure 35, closed symbols) and for comparison we tried to eliminate all secondary craters according to the criteria introduced in Section II 2 (Figure 35, open symbols).- Nearly all secondary craters (with the exception of several characteristic V-structures) were included in the measurement (Neukum, 1976) of the lava filling of Tsiolkovsky. For Copernicus, the secondary crater cluster in the northeast of the crater base (see Section III 1a), which was eliminated for the dating process, was included in the measurement; the same occurred for the continuous ejecta cover of Aristarchus in the northwest of the

crater. On the other regions (Oceanus Procellarum, Aristarchus), no unequivocal clusters were discovered, only variations in crater densities were noted which could be caused statistically. Here, too, the already mentioned elimination criteria of Oberbeck and Morrison (1973) were carefully applied. In all cases the measured distributions bent off from the primary crater distribution at a diameter D_s which is greater as the area under consideration is more heavily cratered, i.e., the older it is. This is illustrated on the example of the Oceanus Procellarum and the Tsiolkovsky empirical curve (Figure 36). For $D > D_s$ the measured crater size distribution follows the standard curve, for $D < D_s$ there results superelevated measured crater frequencies. In Figure 35 the integral crater frequencies N (for D = 1 km) of the regions investigated are plotted against the diameter D_s. The correlation between the age of the target and D_s can be seen: in older regions the contamination begins with larger craters instead of on recent ones. Moreover D_s depends on how careful the elimination of the discernable secondary craters is performed. To the right in Figure 35 the drawn line can generally be used as a dating line if an elimination of secondary craters is performed. For $D < D_s$, however, one should generally count on quantitative inclusion of secondary craters which can no longer be identified as such in this large region. One measurement performed on these diameter values ($D < D_s$) would lead — in accordance with the degree of contamination — to a very great age. In the case of the measured distributions entered in Figure 35, there would be a superelavation of up to a factor of about 2. Under consideration of this state of affairs, a maximum age can be estimated if appropriate caution is exercised. If, for example, a region which is older than ($\approx 1 \cdot 10^9$ years ($N \approx 1 \cdot 10^{-3}\,km^{-2}$, for D = 1 km) can be dated with high precision, then it is meaningful to measure only craters of diameters D > 400 m provided we are not dealing with particularly favorably arranged surfaces. For younger objects, about the age of Tycho, the minimum diameter $D \approx 40$–50 m follows from Figure 35.

/46

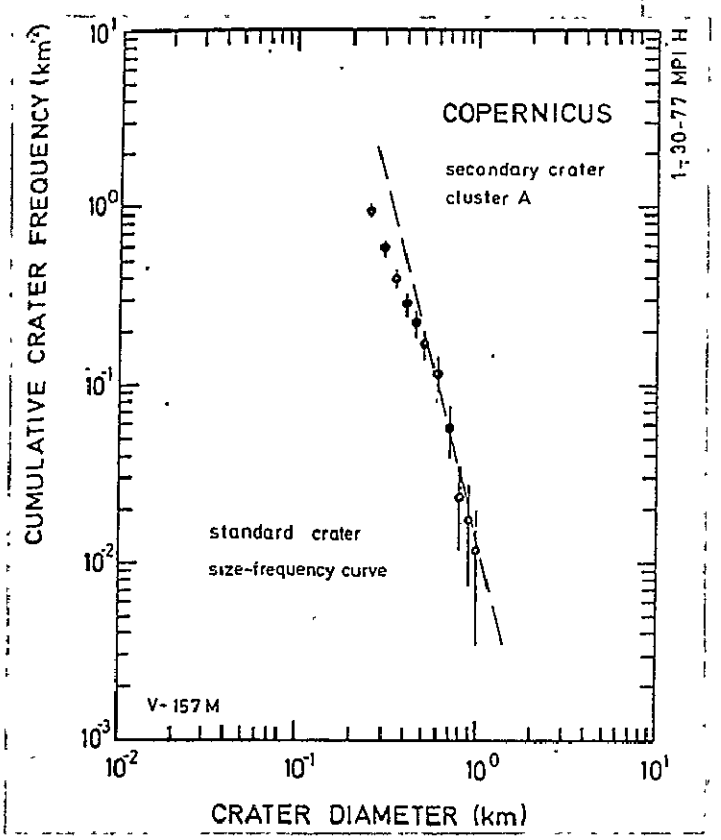

Figure 34. Measured secondary crater size distribution of a cluster on the continuous ejecta blanket of Copernicus. The primary crater size distribution function is drawn through the data.

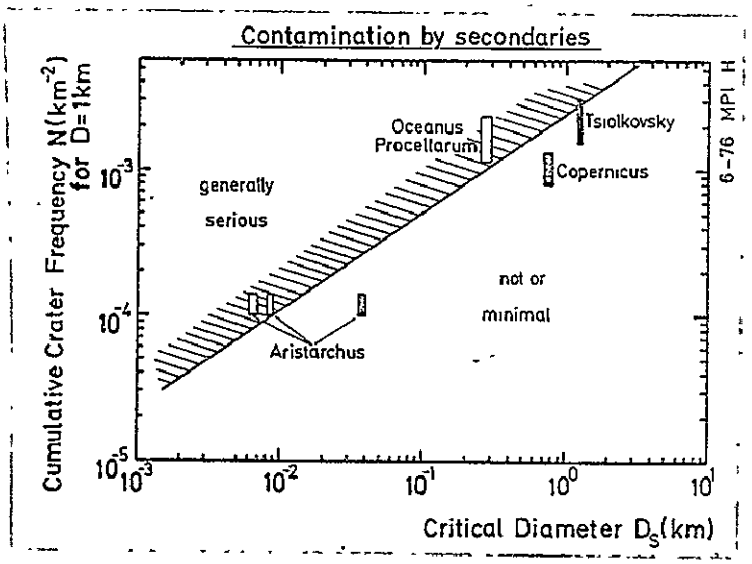

Figure 35. Influence of secondary craters on primary crater populations: the beginning of quantitative contamination by secondary craters shifts to the larger diameters as the age of the test region increases.

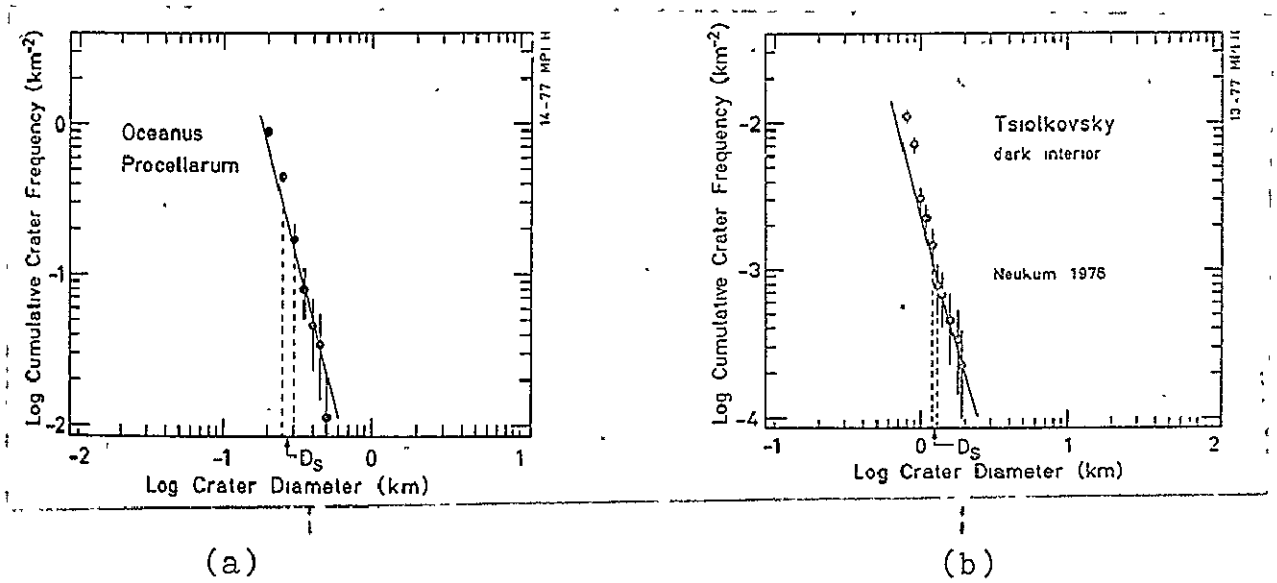

Figures 36 a,b. Measured crater size distributions which are superrelevated due to secondary crater contamination for diameters $D < D_S$.

a) Oceanus Procellarum b) Tsiolkovsky

The measurements performed on secondary crater groups (chains and clusters) permitted the estimation of the maximum superelevation of frequencies of primary craters due to inclusion /47 of secondary craters for regions of ages < 3.5×10^9 years in the range of $300\ m \lesssim D \lesssim 4\ km$. The absolute frequencies* in the secondary crater groups lie about an order of magnitude above the primary ones which determine the age of the region. The generally investigated surfaces are large compared to the number of surfaces covered by secondary crater groups which they contain (could contain). If primary and secondary craters are evaluated together on such regions, the resulting frequency lies less than a factor of 10 above the determination made on the basis of primary craters alone. Older calculations of the contamination of primary crater populations by secondary craters deviates from these estimations. They proceed from too steep a secondary crater distribution curve which was extrapolated to smaller

* The datum level is the region surrounded by the straight lines enveloping the crater group (see Figure 30).

crater diameters (Shoemaker, 1965). On the basis of the uncorrected starting distribution of secondary craters, the superrelevations determined in the Mare regions of more than one order of magnitude are certainly too high. Gault (1970) arrived at similar conclusions, however, his were based on other considerations.

V. EXPERIMENTALLY PRODUCED SECONDARY IMPACTS /48

V. 1 Experimental description and evaluation processes

In this chapter, impact experiments and investigations of the ejection of secondary particles are described. The results — particularly the size distribution of ejecta — are compared with the corresponding data of other authors and agreement and differences are illustrated which exists for the ejection phenomenon of large lunar craters.

a) Apparatus used

The impact experiments to produce secondary particles were performed with the small gas cannon of the Ernst-Mach-Institute in Freiburg. There, projectiles of up to 2.5 mm diameter can be accelerated to velocities of up to $\approx$ 5 km/s. A description of the operation of the small gas cannon is found, for example, in Schneider (1972). Impact experiments with projectiles of known mass and velocity were performed on the 2MV van de Graaff-accelerator in Heidelberg and using the small gas cannon to calibrate the secondary impact structures. The dust accelerator is described in detail in a series of papers (e.g., Rudolph, 1969; Neukum, 1969). There (electrically conducting) particles of masses between 10^{-9} and 10^{-15} g were accelerated to velocities between 1 and 60 km/s by electrostatic means. A raster electron microscope (stereoscan) was used to search, measure and photograph impact structures produced by the accelerator. Its resolution was at about 500 Å. It is powered by a 20 kv acceleration

voltage. By using a Si(Li) semiconductor detector (resolution limit: 160 eV) connected to the stereoscan, the energy spectrum of the characteristic X-ray excitement of the primary electron beam on the target was recorded in the range of 1-10 keV; thus the chemical composition of the target structures was qualitatively determined in the micro-region. The spectra were plotted by the recording equipment.

b) Experiments

Impact experiments were performed using the light gas cannon; these are described below. A steel ball of mass 1.4×10^{-2} g was fired at a velocity of 4.1 km/s at a fine grain basalt target. During the penetration process, the target chamber was evacuated to a pressure of 1.5×10^{-4} torr in order to keep the interaction effects of small ejecta with residual gas molecules negligible.

In order to record ejected particles, 5 lead targets were arranged in a holder at a distance of 15 cm from the intended impact point. The construction is shown schematically in Figure 37. From this we see that the ejecta struck the target almost perpendicularly. Since the point of impact could not exactly be /49
localized in advance, the actual ejection and impact angles of the secondary particles were postcalculated.

c) Calibration experiments

The target material, lead, was selected because it is a suitable detector for particles having velocities less than 200 m/s. In order to keep a sufficiently smooth surface for scanning, the lead was milled. Then the targets were loaded with gold. This simplified the location of smaller, faster-moving

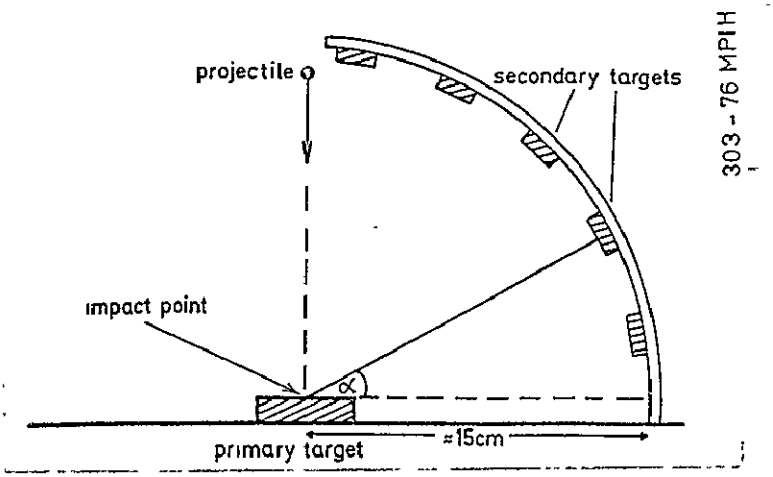

Figure 37. Schematic assembly of the experiment using the light gas cannon.

particles, particularly in the calibration experiments on the dust accelerator. The target surfaces were selected of a size such that the secondary particle density could be determined with sufficiently accurate statistics. Non-rolled lead targets were used for calibration of the light gas cannon.

Aluminum and gold-loaded glass balls of diameters between 0.5 and 20 μm were fired at lead targets at velocities between 200 m/s and 3 km/s to calibrate the dust accelerator. The supplemental impact experiments on the light/gas cannon were performed at velocities between 800 m/s and 2.5 km/s. Here, aluminum projectiles of 2.5 mm and glass projectiles of 2 mm diameter were used. There resulted impact structures whose morphology changed with increasing speed: the projectiles were reflected (I), remained embedded(II) or formed craters (III). Several examples for this are shown in Figure 38 a-h. In Table 3 the results of the calibration experiments are summarized. The D/d relationships shown there were calculated from the known average projectile masses and the determined diameters of the impact structures.

ORIGINAL PAGE IS
OF POOR QUALITY

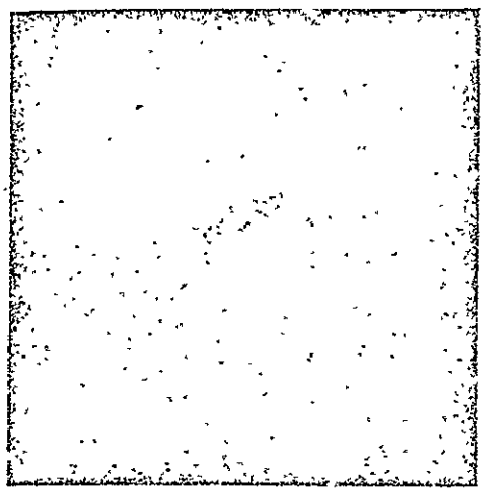

a: $\alpha = 42^{\circ}$; $\beta = 7000$;
v = 200 m/s; Glass, Al → Pb.

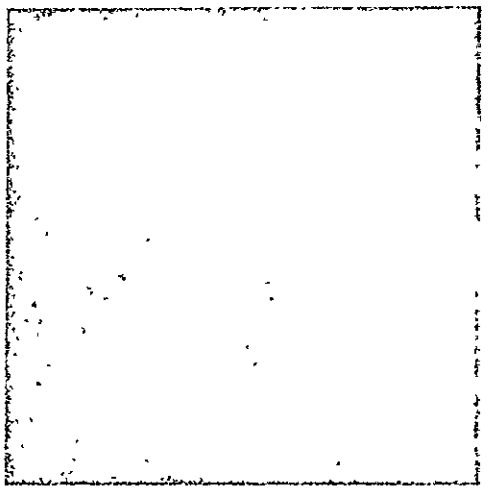

b: $\alpha = 0^{\circ}$; $\beta = 2800$;
v = 300 m/s; Glass → Pb.

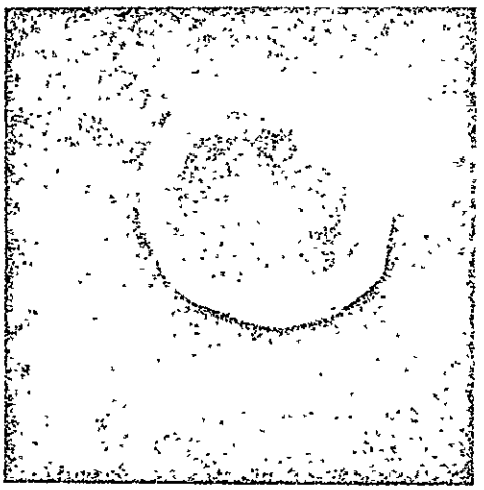

c: $\alpha = 31^{\circ}$; $\beta = 4900$;
v = 300 m/s; Al → Pb.

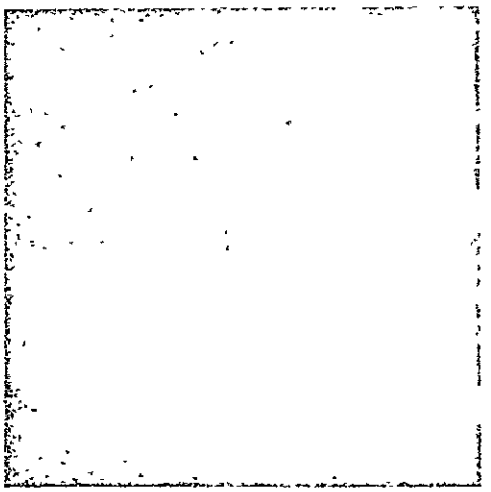

d: $\alpha = 10^{\circ}$; $\beta = 2100$;
v = 500 m/s; Glass → Pb.

Figure 38 a-h: Morphology of the impact structures for different projectile velocities v (α = angle of inclination during photograph of the target from the horizontal, β = magnification.

ORIGINAL PAGE IS
OF POOR QUALITY

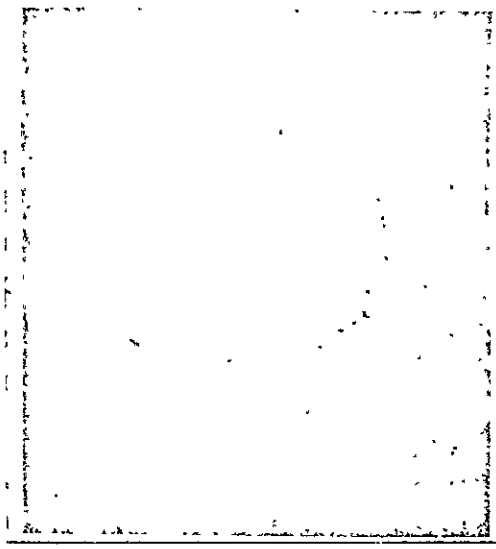

e: $\alpha = 40^{\circ}$; $\beta = 4000$;
v = 500 m/s; Al → Pb.

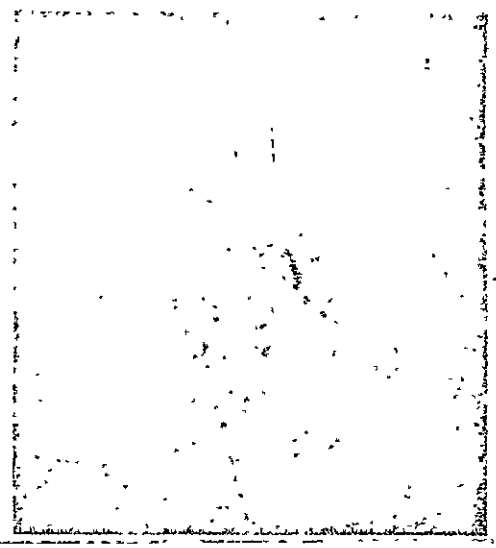

f: $\alpha = 45^{\circ}$; $\beta = 1200$
v = 1400 m/s; Al → Pb.

g: $\alpha = 45^{\circ}$; $\beta = 1250$;
v = 1400 m/s; Glas → Pb.

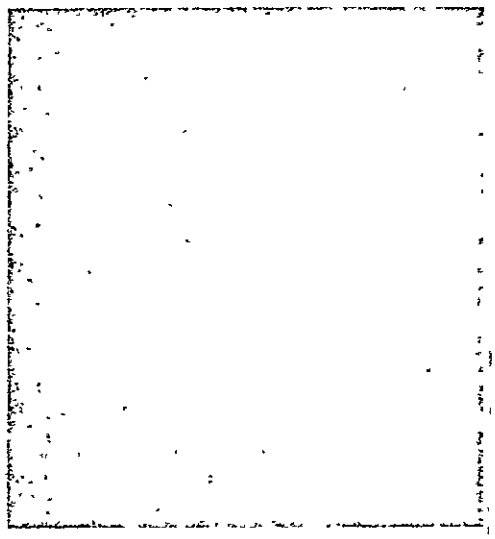

h: $\alpha = 21^{\circ}$; $\beta = 7000$;
v = 2000 m/s; Al → Pb.

Figure 38 (continued).

TABLE 3. RESULTS OF THE CALIBRATION EXPERIMENTS ON THE DUST ACCELERATOR AND ON THE LIGHT GAS CANNON

	Velocity m/s	Projectile composition*	Projectile	Morphology type	D/d**
(a)	200 m/s	Glass, Al	Reflected	I	0.4-0.7
(b)	300 m/s	Glass	Reflected	I	0.4-0.7
(c)	300 m/s	Al	Embedded	II	1.0
(d)	500 m/s	Glass	Embedded	II	1.0
(e)	500 m/s	Al	Embedded	II	1.0
(f)	1400 m/s	Al	Produces craters	II-III	2.8-3.0
(g)	1400 m/s	Glass	Produces craters	III	2.8-3.0
(h)	2000 m/s	Al	Produces craters	III	1.9-3.7
(i)	1400 m/s	Glass, Al	Produces craters	III	3.0
(j)	2000 m/s	Al	Produces craters	III	3.6

* (i), (j) Data from the mm projectiles
** D = diameter of impact structure; d = projectile diameter.

As we see from Table 3, below a velocity of 200 m/s only projectile reflections are observed. Deformations (I) in the target shown in Figures 38a and b occur in this. The diameter of these structures should decrease with decreasing velocities. Therefore, in the following we begin from a ratio $(D/d)_I = 0.4$ for conversions into projectile diameters. For impact velocities $\geq$ 2 km/s, craters occurred in which the projectile material covered the crater (Figure 39 g and h, Type III in Table 2). To convert the projectile diameters we set $(D/d)_{III} = 3.7$. For the embedded projectiles we assumed that $(D/d)_{II} = 1$. /53

d) Measurement principles and data reduction

The lead targets exposed in the light gas cannon were completely scanned by the stereoscan at 100 times resolution. About 5% of the surface was also scanned at various points on the target at 2000 times resolution. In two cases 4% of the surface was also scanned at 500 times resolution. In Figures 39 a-h, typical impact structures were shown which were produced by ejecta. These are deformations (Type I, Figure 39a and b) if the ejecta were reflected at the target. Figures 39 c-h show embedded ejected particles (Type II), whereas Figure 39 h is concerned with primary projectile material. Craters produced by ejecta (Type III) are found in Figure 39b, g and h.

The diameter of the impact structures was measured directly at the display screen of the equipment, sometimes the different diameters were determined for non-round structures. Here we always recorded which type (I, II or III) was present. The data were stored on punched cards and evaluated with a modified version of the program for lunar craters (see Section II 1c). The diameters of the impact structures were converted into particle diameters by the appropriate D/d-ratio. The integral frequencies of particle diameters were plotted for the different types.

V. 2 Size distribution of secondary particles

By using the measurement principles described in the previous section, it was possible to determine the size distribution of the ejected particles for different velocity intervals from the secondary impact structures. One difficulty in this was that the density of the impact structures on the target showed local variations. Therefore, even at greater magnifications, large surfaces had to be examined. Otherwise there would result statistically induced variations.

The measured size distributions are shown in Figure [40] a-e for the different ejected angles. From this results that the size distribution for the particles of different speed is nearly the same: $N(d,v) \sim f(v)d^{-\beta}$, where N is the integral frequency, d is the particle diameter and f(v) is a velocity function which describes the variation of absolute frequencies. An angle and particle size dependence $\beta = \beta(\alpha,d)$ exists, however, this is very weak: between $\alpha = 21°$ and $66°$, β varies on the average between -2 and -3.

V. 3 Angular- and velocity-dependence of ejected mass

The relative constance of size distribution makes possible a comparison of absolute frequencies for different ejection angles and speeds. As a reference value we use the particle diameter d = 100 µm. For the total frequency of all recorded /57
particles there resulted an increase with increasing ejection angle as shown in Figure 41. The same is also true for the particles sorted according to ejection velocities. Whereas the fast crater producing ejecta always represents less than 1% of the total number of particles, the percentage of the particles embedded in the target and reflecting from the target shifts in various angle ranges relative to each other. As can be seen in Figure 41,

the quantity of the Type I and II particles for $\alpha = 23°$ are comparable, for $\alpha = 54°$ the ejecta of Type II are even more frequent than the reflected particles by a factor of 3. For the other ejection angles, the reflected particles were recorded 2-4 times more frequent than the embedded particles. There results, then, that the ejecta generally are thrown out at low velocities where the percentage of the particles with $v \leq 200$ m/s is about (except for a factor of 4) equal to ejecta particles of average velocity (200 m/s $\leq v \leq$ 2000 m/s).

ORIGINAL PAGE IS
OF POOR QUALITY

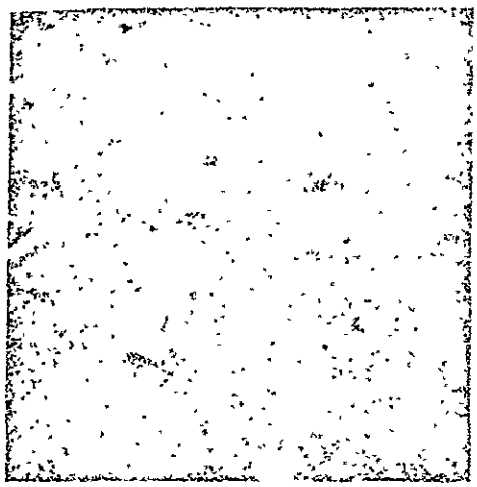

a: $\alpha = 0^{o}$; $\beta = 1400$.

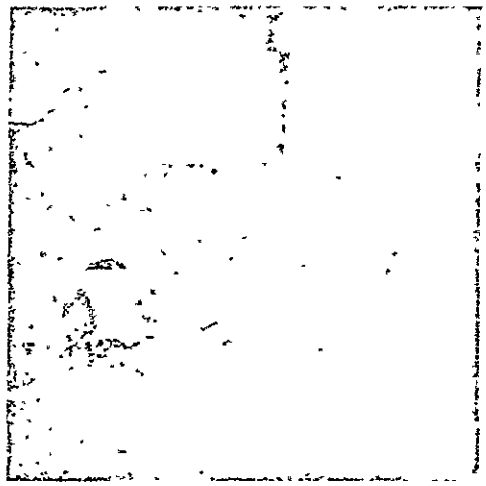

b: $\alpha = 0^{o}$; $\beta = 350$.

c: $\alpha = 0^{o}$; $\beta = 370$.

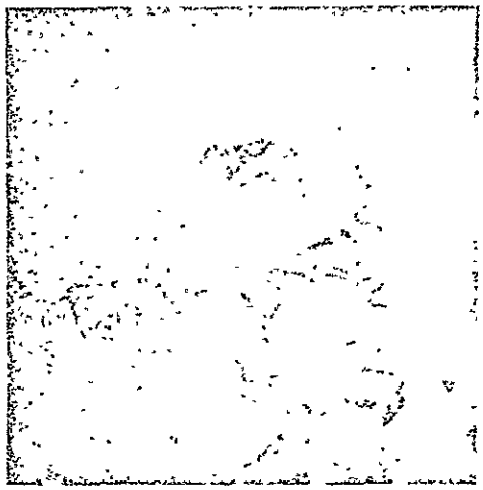

d: $\alpha = 0^{o}$; $\beta = 740$.

Figures 39 a-h: Impact structures produced by ejecta on the secondary target (α = angle of inclination, on photograph, of the target from the horizontal, β = the enlargement).

ORIGINAL PAGE IS
OF POOR QUALITY

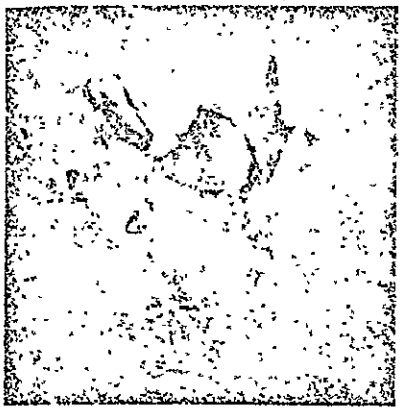

e: $\alpha = 0^{\circ}$; $\beta = 700$.

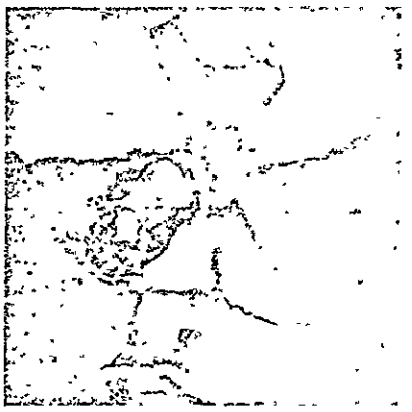

f: $\alpha = 0^{\circ}$; $\beta = 420$.

g: $\alpha = 0^{\circ}$; $\beta = 370$.

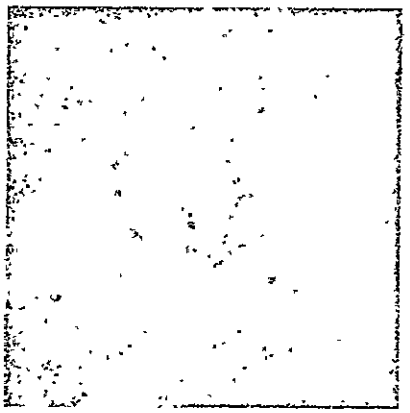

h: $\alpha = 40^{\circ}$; $\beta = 3500$.

Figure 39 a-h (Continued):

a)

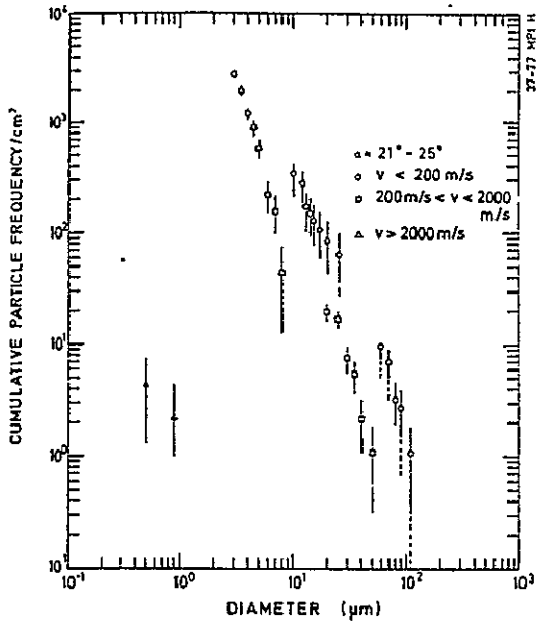

b)

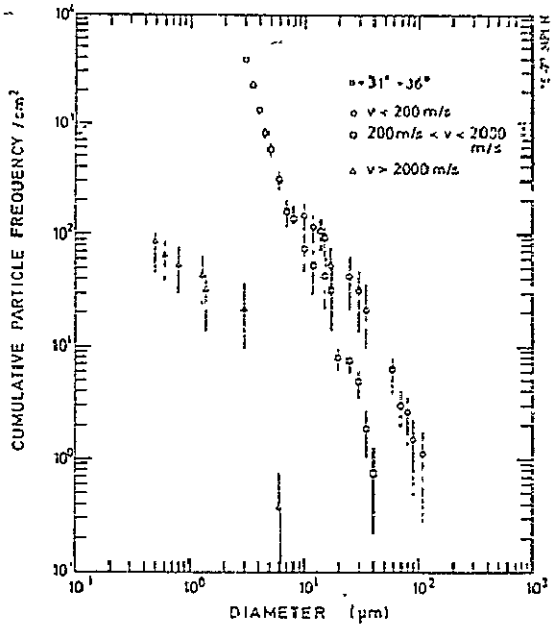

c)

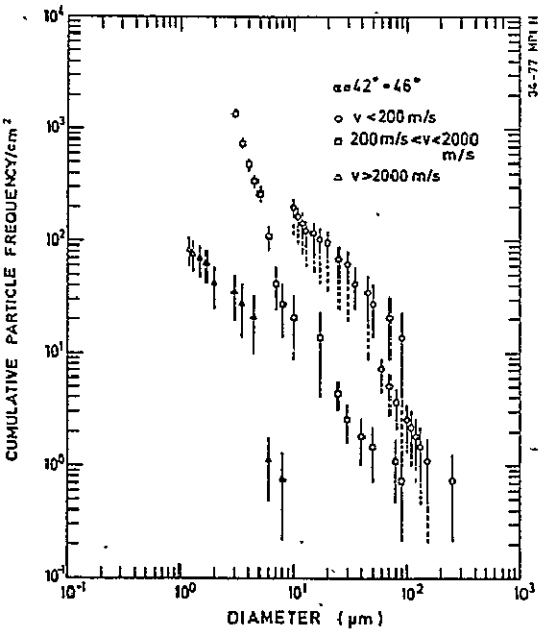

d)

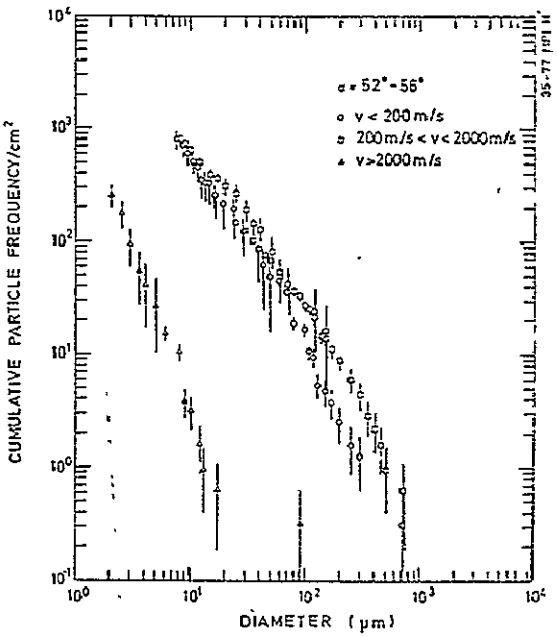

Figure 40 a-e. Measured integral frequency distribution of the ejecta diameter for ejection angles between 21° and 66° and different velocity intervals. For the case where particles were measured which could not be definitely classified, the points were given a lengthened (dashed line) error zone. Their elimination would lead to lower frequency values.

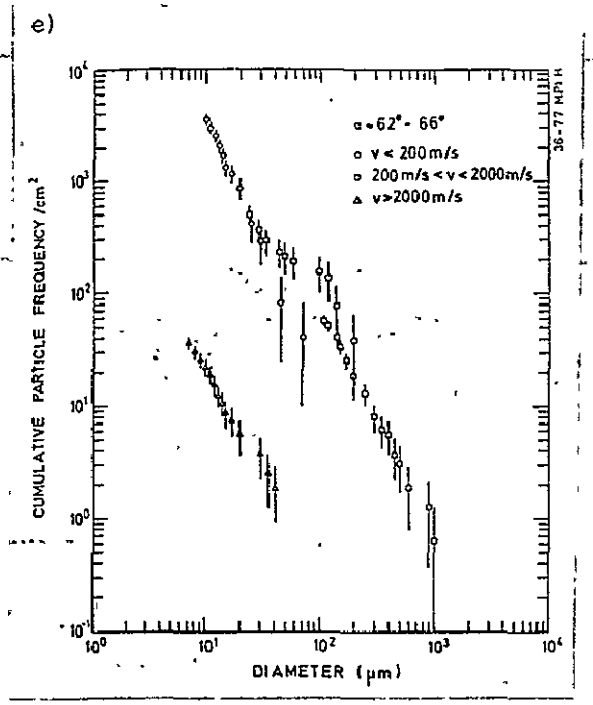

Figure 40 a-e (Continued)

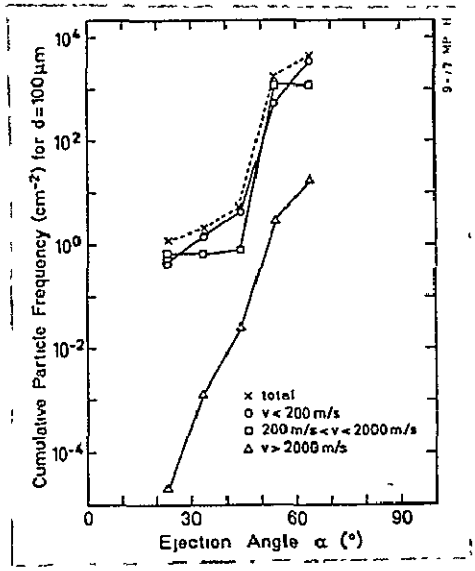

Figure 41. Frequency of ejected particles as a function of the ejection angle α for different ranges of ejection velocity.

/57

Particles from all three velocity ranges under consideration were recorded for each of the angle regions examined. The velocity steps, however, are very coarse. Therefore, only a qualitative statement can be made about the variations of ejection velocities of the ejecta as a function of the ejection angle. From Figure 41 we see that more than 99% of the ejecta is ejected at velocities below 2000 m/s. More than 50% of the particles registered at $\alpha \ll 25°$ and $50° < \alpha < 58°$ had velocities between 200 m/s and 2000 m/s. The majority of particles in the other angle ranges examined were slower than 200 m/s. /58

V. 4 Discussion

The experimental results obtained in the framework of this work agree quite well with the results of similar simulation experiments. Gault, et al., (1963) and Gault and Heitowit (1963) performed impact experiments using Basalt as the target material and the ejection was examined by time loop photography at high film rates. It turned out that the ejected mass increased with increasing angles and that the ejecta was usually emitted at velocities less than 500 m/s and $\alpha > 45°$. From the mass distribution of ejected particles determined by Gault, et al., there results an ejecta size distribution function of the form $N \sim d^{\beta}$, where $\beta \cong -2.4$. This exponent agrees with the data of this work.

The exponent in the distribution function is similar to that of the lunar ejecta in the (100 m - 1 km) range. This indicates similar (fragmentation) mechanisms in the origination of ejecta from cm-km craters. The steep deficit branch appearing for lunar secondary crater distributions was not observed in the distributions of experimentally-produced ejecta. The Spallation occurring on Basalt cratering may produce sufficient numbers of

large ejecta particles so that the deficit branch of the ejecta size distribution only occurs at diameters which are larger than the primary projectile diameter.

Other similarities in the ejection process which are found over orders of magnitude in the crater dimension exist in the average similarity of ejection velocities. For impact experiments on Basalt as well as for large lunar impacts, the main mass of ejecta is thrown out at velocities below 500 m/s. As is shown by the appearance of lunar secondary craters in clusters, many ejecta particles are apparently thrown out in groups (Shoemaker, 1960). This phenomenon was also observed in the experimental ejection studies: on the average the targets exhibit a homogeneous density of secondary impact structures. In this respect, we probably also see the appearance of preferred directions in the ejection which can occur due to weak zones in the target (Shoemaker, 1960).

Whereas the previously discussed ejection phenomena appear to be of a general nature, there is a series of dynamic processes /59 which depend greatly on target material, crater dimensions, crater shape, etc. Using the examples of the angle dependency of the ejection of different type craters, we discuss this phenomenon below.

Schneider (1975) obtained results which deviate from those of this work in an impact experiment on a glass target. He obtained a maximum density of secondary particles (where $v \geq 3$ km/s) for the ejection angle $\alpha \approx 25°$ and another maximum $\alpha \approx 60°$. This second maximum was also found by Eichhorn (1974) using light flash investigations (using primary targets made of metal). The deviations may be explained by the different (primary) target materials or may be caused by the different particle detection methods.

The ejection in sand occurs primarily between 30° and 50° (see Chao, 1974; Stoffler, et al., 1975); this is different than for a solid target where the main mass of ejecta is thrown out at steeper angles. The resulting ejection structures exhibit comparable uniformities with those of larger impacts: inverse stratography, radial intensity decreases (Stoffler, et al., 1975).

Particularly large explosion craters, like, for example, Sedan and Teapot Ess., show marked similarities with lunar impact craters. Their ejection structures somewhat follow the same uniformities and can therefore be included in the investigations of this project. However, in this we must note that the ejection phenomena depend on the depth of the detonating charge (Carlson and Jones, 1975). For the study of angle dependence of the ejection, therefore, younger terrestrial impact craters — for example, the Ries crater — should be preferred. With these craters, the lateral transport of ejecta seems to dominate at smaller ejection angles α (Chao, 1974). Shemaker (1960), also arrived at a similar result due to ballistics calculations which he performed on ejecta of the lunar crater Copernicus.

The preceding summary of several results of the ejection studies show that the mechanisms occurring in the formation of craters by no means proceed similarly for all structures. There are parameters which are apparently of a general nature (e.g. the size distribution function and the velocity of ejecta and ejection in clusters), as well as those which depend greatly on the projectile and target parameters (angle distribution of ejected mass).

VI. SUMMARY

Young lunar impact structures were investigated by using lunar orbiter, Apollo Metric and panorama photographs. Measurements on particularly homogeneous areas low in secondary craters made possible an expansion of primary crater distribution to small diameters. This is now sure for a range between 20 m $\leq$ D $\leq$ 20 km and this indicates that the size and velocity distribution of the impacting bodies in the last 3×10^9 years has been constant. A numerical approximation in the form of a 7th degree polynomial was obtained for the distribution. /60

For the north Ray crater which was dated with relative precision (49 million years) an integral crater frequency of $(3.9 \pm 1.0) \times 10^{-5} km^{-2}$ was determined for D = 1 km.

Investigations of the central cluster and of the light Mantle region in the Taurus Littrow valley — whose origination is attributed to impacts of ejecta from the crater Tycho — produced crater frequencies which agree with the values obtained for Tycho. By using radiation age determinations of appropriate Apollo 17 samples an absolute dating of Tycho can be performed. The comparison of crater frequencies and absolute ages of the areas investigated indicate that the flux of impacting bodies in the Earth-Moon system has been nearly constant in the last 3×10^9 years. The methods of relative dating by using crater statistics on the craters Copernicus, Aristarchus and Tycho, were applied to different target surfaces and non-contradictory results were obtained. The net resulting integral crater frequencies for D = 1 km are $(1.0 \pm 0.3) \times 10^{-3}$ km^{-2} (Copernicus), $(7.5 \pm 2.5) \times 10^{-4} km^{-2}$ (Kepler), $(1.2 \pm 0.2) \times 10^{-4}$ km^{-2} (Aristarchus) and $(6.0 \pm 1.7) \times 10^{-5}$ km^{-2} (Tycho). The age sequence agrees with the morphologic-stratographic classifications of these craters. Using the radiometric age of North Ray, Tycho and Copernicus, there results absolute ages for the craters

Aristarcus and Kepler of (150 ± 125) million years and (790 ± 160) million years, respectively.

Measurements on secondary craters of Aristarchus and Copernicus have shown that the size distribution of the ejecta produced — except for an explanable deficit percentage of larger particles — agrees with the size distribution of bodies producing primary craters. These measurements began from calculated average impact velocities. The influence of secondary craters on the populations of primary craters was examined and a correlation was obtained between relative age and the beginning of quantitative contamination by secondary craters.

Impact experiments performed on a light gas cannon and on a 2 MV-van de Graaff dust accelerator showed that over 99% of the ejecta produced in a Basalt crater has velocities less than 2 km/s in an angle range of $21° < \alpha < 66°$ and that the ejected /61 mass increased with increasing angle. The size distribution of the ejected particles generally follows a percentage law having constant exponent in the angle and velocity range examined ($v < 200$ m/s; $200 \leq v \leq 2000$ m/s; $v > 2000$ m/s). The results obtained were compared with those of other simulation experiments. It turns out that the mass and frequency distribution of ejecta as a function of the ejection angle appear greatly dependent on target material and crater size, whereas the size distribution function and the average velocity of ejecta vary only a little with the crater size.

REFERENCES

1. Albee, A.L., A.A. Chodos, R.F. Dymek, A.J. Gancarz, D.S. Goldman, D.A. Papanartassiou and G.J. Wasserburg. Dunite from the Lunar Highlands: Petrography, Deformational History, Rb-Sr age (abstract). In Lunar Science V, 3. The Lunar Science Institute, 1974, Houston.

2. Alexander, E.C., Jr., A. Bates, M.R. Coscio, Jr., J.C. Draggon, V.R. Murthy, R.O. Pepin and T.R. Venkatesan. K/Ar Dating of Lunar Soils II. Proc. Lunar Sci. Conf. 7th, 1976, pp. 625-648.

3. Allen, D.A. Infrared Studies of the Lunar Terrain. The Moon, Vol. 2, 1971, pp. 435-462.

4. Anderson, A.T. and E.R. Miller. Lunar Orbiter Photographic Supporting Data. NASA-GSFC NSSDC, May, 1971, 71-13.

5. Apollo 15 - Index of Mapping Camera and Panorama Photographs. NASA-MSC, January, 1972.

6. Apollo 16 - Index of Mapping and Panorama Photographs. NASA-MSC-07251, August, 1972.

7. Apollo 17 - Index of Mapping Camera and Panorama Camera Photographs. NASA-JSC-08640, November, 1973.

8. Apollo 15 - Lunar Photography Index Maps. NASA-MSB, March, 1972.

9. Apollo 16 - Lunar Photography Index Maps. NASA-MSB, October, 1972.

10. Apollo 17 - Lunar Photography Index Maps. NASA-MSB, November, 1973.

11. Apollo 16 - Traverses. NASA Lunar Photomap (1:25000), First Edition, Sh 78 D 2 S 2 (25), 1975.

12. Apollo 17 - Traverses. NASA Lunar Photomap (1:25000), First Edition Sh 43 D 1 S 2 (25), 1975.

13. Arvidson, R., R. Drozd, E. Guinness, C. Hohenberg, C. Morgan, R. Morrison and V. Oberbeck. Cosmic Ray Exposure Ages of Apollo 17 Samples and the Age of Tycho. Proc. Lunar Sci. Conf. 7th, 1976, pp. 2817 - 2832.

14. Baldwin, R.B. The Face of the Moon. University of Chicago Press, Chicago, Illinois, 1949.

15. Baldwin, R.B. The Measure of the Moon. University of Chicago Press. Chicago, Illinois (1963).

16. Baldwin, R.B. On the History of Lunar Impact Cratering. The Absolute Time Scale and the Origin of Plantesimals. Icarus, Vol. 14, 1971, pp. 36-52.

17. Bloch, M.R., H. Fechtig, W. Gentner, G. Neukum and E. Schneider. Meteorite Impact Craters, Crater Simulations and the Meteorite Flux in the Early Solar System. Proc. Lunar Sci..Conf. 2nd, 1971, pp. 2639 - 2652.

18. Boyce, J.M. Ages of Flow Units in the Lunar Nearside Maria Based on Lunar Orbiter IV Photographs. Proc. Lunar Sci. Conf. 7th, 1976, pp. 2717-2728.

19. Carlson, R.H. and W.A. Roberts. Mass Distribution and Throwout Studies. Project Sedan, PNE-217 F. The Boing Company, Seattle, Washington, May, 1963.

20. Carlson, R.H. and G.D. Jones. Distribution of Ejecta from Cratering Explosions in Soils. J. Geophys. Res. Vol. 70, 1975, pp. 1897 - 1910.

21. Carr, M.H. Geologic Map of the Mare Serenitatis Region of the Moon. U.S. Geol. Survey Misc. Geol. Inv. Map I-489, 1966.

22. Chao, E.C.T. Impact Cratering Models and their Application to Lunar Studies - a Geologist's View. Proc. Lunar Sci. Conf. 5th, 1974, pp. 35-52.

23. Dohnanyi, J.S. Collisional Model of Asteroids and their Debris. J. Geophys. Res., Vol. 74, 1969, pp. 2531-2554.

24. Doyle, F.J. Photogrammetric Analysis of Apollo 15 Records. NASA SP-289, 1972, p. 25.

25. Drozd, R.J., C.M. Hohenberg, C.J. Morgan and C. Ralston. Cosmic-Ray Exposure History of the Apollo 16 and other Lunar Sites. Lunar Surface Dynamics. Geochim. Cosmochim. Acta, Vol. 38, 1974, pp. 1625-1642.

26. Eberhardt, P., J. Geiss, J. Grögler and A. Stettler. How Old is the Crater Copernicus? The Moon, Vol. 8, 1973, pp. 104-114.

27. Eichhorn, G. Investigations of Light Emissions on High-Velocity Impacts. Dissertation, University of Heidelberg, 1974.

28. Fechtig, H., J. B. Hartung, K. Nagel and G. Neukum. Lunar Microcrater Studies, derived Meteoroid Fluxes and Comparison with Satellite-Borne Experiments. Proc. Lunar Sci. Conf. 5th, 1974, pp. 2463 - 2474.

29. Gault, D.E. and E.D. Heitowit. The Partition of Energy for Hypervelocity Impact Craters formed in Track. Symposium on Hypervelocity Impact, 6th, Cleveland, Ohio, April 30 - May 2, 1963. Proc., Vol. 2, Pt. 2, 1963, pp. 419-456.

30. Gault, D.E. Shoemaker, E.M. and H.J. Moore. Spray Ejected from the Lunar Surface by Meteoroid Impact. NASA Tech. Note D-1767, Washington D.C. 1963.

31. Gault, D.E. Saturation and Equilibrium Conditions for Impact Cratering on the Lunar Surface. Criteria and Implications. Radio Science, Vol. 5, 1970, pp. 273-291.

32. Gilbert, G.K. The Moon's Face. Bull. Phil. Soc. Wash., Vol. 12, 1893, p. 241.

33. Greeley, R. and D.E. Gault. Precision Size-Frequency Distributions of Craters for 12 Selected Areas of the Lunar Surface. The Moon, Vol. 2, 1970, pp. 10 - 77.

34. Greeley, R. and D.E. Gault. Endogenetic Craters Interpreted from Crater Counts on the Inner Wall of Copernicus. Science, Vol. 171, 1971, pp. 477-479.

35. Green, J. A Large-Scale Surface Pattern Associated with the Ejecta Blanket and Rays of Copernicus. J. Geophys. Research, Vol. 76, 1965, pp. 5719-5731.

36. Guest, J.E. Stratigraphy of Ejecta from the Lunar Crater Aristarchus. Geol. Soc. America Bull., Vol. 84, 1973, pp. 2873 - 2894.

37. Hackman, R.J. Geologic Map of the Kepler Region of the Moon. U.S. Geol. Survey Misc. Geol. Inv. Map I-355, 1962.

38. Hansen, Th. P. Guide to Lunar Orbiter Photographs. NASA SP-242, 1970.

39. Hartmann, W.K. Terrestrial and Lunar Flux of Large Meteorites in the Last Two Billion Years. Icarus, Vol. 4, 1965, pp. 157-165.

40. Hartmann, W.K. Lunar Crater Counts. VI: The Young Craters Tycho, Aristarchus and Copernicus. Commun. Lunar Planet. Lab. Ariz. No. 119, 1968, pp. 145-156.

41. Hartmann, W.K. Paleocratering of the Moon. Review of Post-Apollo Data. Astrophys. Space Sci., Vol. 17, 1972, pp. 48 - 64.

42. Hartmann, W.K. and C.A. Wood. Moon: Origin and Evolution of Multi-Ring Basins. The Moon, Vol. 3, 1971, pp. 3 - 78.

43. Hawkins, G.S. and E.K.L. Upton. The Influx Rate of Meteors in the Earth's Atmosphere. Astrophys. J., Vol. 128, 1958, pp. 727-735.

44. Howard, K.A. Avalanche Mode of Motion - Implication from Lunar Samples. Science, Vol. 180, 1973, pp. 1052 - 1055.

45. Jessberger, E.K., J.C. Huneke and G.J. Wasserburg. Evidence for a 4.5 Aeon Age of Plagioclase Clasts in a Lunar Highland Breccia. Nature, Vol. 248, 1974, pp. 199-202.

46. Kirsten, T. and P. Horn. Chronology of the Taurus Lithrow Region III - Aves of Mare Basalts and Highland Breccias and some Remarks about the Interpretation of Lunar Highland Rock Ages. Proc. Lunar Sci. Conf. 5th, 1974, pp. 1451 - 1475.

47. König, B. Investigations of Impact Structures on Planetary Surfaces. Diplomarbeit, University of Heidelberg, 1974.

48. König, B. and G. Neukum. Relative Ages of Eratosthenian and Copernican Craters. Published in: The Moon, 1977.

49. Kuiper, G.B. Proc. Nat. Acad. Sci., Vol. 40, 1954, p. 1096.

50. Lindblad, A.B. Luminosity Function of Sporadic Meteors and Extrapolation of the Influx Rate to the Micrometeorite Region. Smithson. Contrib. Astrophys., Vol. 11, 1967, pp. 171-180.

51. Lucchitta, B.K. Tycho and the Apollo 17 Landing Site (abstract). EOS (Trans. Amer. Geophys. Union), Vol. 56, 1975, p. 389.

52. Lucchitta, B.K. and A.G. Sanchez. Crater Studies in the Apollo 17 Region. Proc. Lunar Sci. Conf. 6th, 1975, pp. 2427 - 2441.

53. Marti, K., B.D. Lightner and T.W. Olson. Krypton-Xenon in the Lunar Samples and the Age of North Ray Crater. Proc. Lunar Sci. Conf. 4th, 1973, pp. 2037 -2048.

54. Moore, H.J. Missile Impact Craters (White Sands Missile Range, New Mexico) and Applications to Lunar Research. U.S. Geol. Survey Prof. Paper 812-B, B 1-43, 1976.

55. Muehlberger, W.R., R.M. Batson, E.A. Cernan, V.L. Freeman, M.H. Hait, H.E. Holt, K.A. Howard, E.D. Jackson, K.B. Larson, V.S. Reed, J.J. Rennilson, H.H. Schmitt, D.H. Scott, R.L. Sutton, D. Stuart-Alexander, G.A. Swann, N.J. Trask, G.E. Ulrich, H.G. Wilshire and E.W. Wolfe. Preliminary Geologic Investigation of the Apollo 17 Landing Site, 1973.

56. NASA Lunar Chart LAC 39, 1963.

57. NASA Lunar Topographic Map, Orbiter V-Site 48, 1972.

58. Neukum, G. Investigations of Projectile Material in Microcraters. Diplomarbeit, University of Heidelberg, 1969.

59. Neukum, G. Unpublished Data. 1976.

60. Neukum, G., B. König, H. Fechtig and D. Storzer. Cratering in the Earth-Moon System: Consequences for age Determination by Crater Counting. Proc. Lunar Sci. Conf. 6th, 1975a, pp. 2597-2620.

61. Neukum, G., B. König, and J. Arkani-Hamed. A Study of Lunar Impact Crater Size-Distributions. The Moon, Vol. 12, 1975b, pp. 201-229.

62. Neukum, G. and H. Dietzel. On the Development of the Crater Population on the Moon with Time under Meteoroid and Solar Wind Bombardment. Earth Planet. Sci. Letters, Vol. 12, 1971, pp. 59 - 66.

63. Neukum, G. and P. Horn. Effects of Lava Flows on Lunar Crater Populations. The Moon, Vol. 15, 1976, pp. 205-222.

64. Neukum, G. and B. König. Dating of Individual Lunar Craters. Proc. Lunar Sci. 7th, 1976, pp. 2867 - 2881.

65. Oberbeck, V.R. A Mechanism for the Production of Lunar Crater Rays. The Moon, Vol. 2, 1971, pp. 263-278.

66. Oberbeck, V.R. and R.H. Morrison. On the Formation of the Lunar Herringbone Pattern. Proc. Lunar Sci. Conf. 4th, 1973a, pp. 107 - 123.

67. Oberbeck, V.R. and R.H. Morrison. The Lunar Herringbone Pattern. In Apollo 17 Preliminary Sci. Report, NASA SP-330, 1973b, 32-15 to 32-29.

68. Oberbeck, V.R., F. Horz, R.H. Morrison, W.L. Quaide and D. E. Gault. On the Origin of the Lunar Smooth-Plains. The Moon, Vol. 12, 1975, pp. 19-54.

69. Offield, T.W. and H.A. Pohn. Lunar Crater Morphology and Relative Age Determination of Lunar Geologic Units. Part 2. Applications U.S. Geol. Survey Prof. Paper 700-C, C 163-C 169, 1970.

70. Öpik, E.J. Research on the Physical Theory of Meteor Phenomena. I: Theory of the Formation of Lunar Craters. II: The Possible Consequences of the Collisions of Meteors in Space. Acta et Comm. Univ. Tartuensis, XXX, 1, 1936.

71. Öpik, E.J. Surface Properties of the Moon. Progress in the Astronautical Sciences, Ed. S.F. Singer, Vol. 1, North-Holland Amsterdam, 1962, p. 219.

72. Pettengill, G.H. and T.W. Thompson. A Radar Study of the Lunar Crater Tycho at 3.8-cm and 70-cm Wavelengths. Icarus, Vol. 8, 1968, pp. 457-471.

73. Pohn, H.A. and T.W. Offield. Lunar Crater Morphology and Relative-Age Determination of Lunar Geologic Units - Part 1. Classification. U.S. Geol. Survey Prof. Paper, 700-C, C 153-C, 1970, p. 162

74. Roberts, W.A. Secondary Craters. Icarus, Vol. 3, 1964, pp. 348-364.

75. Rudolf, V. Investigations of Craters of Micro-Projectiles in the Velocity Range of 0.5 - 10 km/s. Z. f. Naturforschung, Vol. 24a, 1969, pp. 326-331.

76. Schneider, E. Micro-Craters on the Lunar Surface and their Simulation in the Laboratory. Dissertation, Universitat Heidelberg, 1972.

77. Schneider, E. Impact Ejecta Exceeding Lunar Escape Velocity. The Moon, Vol. 13, 1975, pp. 173-184.

78. Shoemaker, E.M. Ballistics of the Copernican Ray System. Proc. Lunar and Planetary Colloq., Vol. 2, No. 2, 1960.

79. Shoemaker, E.M., R.J. Hackman and R.E. Eggleton. Interplanetary Correlation of Geologic Time. Adv. Astronaut. Sci., Vol. 8, 1962, pp. 70-89.

80. Shoemaker, E.M. Preliminary Analysis of the Fine Structure of the Lunar Surface in Mare Cognitum. In "The Nature of the Lunar Surface", John Hopkins Press, Baltimore, 1965, pp. 23 - 77.

81. Shoemaker, E.M., R.M. Batson, A.L. Bean, C. Conrad, Jr., D.H. Dahlem, E.N. Goddard, M.H. Hart, K.B. Larson, G.G. Schaber, D.L. Schleicher, R.L. Sutton, G.A. Swann and A.C. Waters. Preliminary Geologic Investigation of the Apollo 12 Landing Site, Part A: Geology of the Apollo 12 Landing Site. In Apollo 12 Preliminary Sci. Report, NASA-SP-235, 1970, pp. 1-13 to 1 - 56.

82. Shoemaker, E.M. and E.F. Helin. Systematic Search for Planet Crossing Asteroids and the Estimation of Impact Crater on the Terrestrial Planets. NASA TM X-3364, 1976, pp. 18 - 22.

83. Silver, L.T. U-Th-Pb Isotopic Systems in Apollo 11 and 12 Regolith Materials and a Possible Age for the Copernicus Event. EOS (Trans. Am. Geophys. Union), Vol. 52, 1971, p. 534.

84. Soderblom, L.A. and L.A. Lebovsky. Technique for Rapid Determination of Relative Ages of Lunar Areas from Orbital Photography. J. Geophys. Res, Vol. 77, 1972, pp. 279-296.

85. Soderblom, L.A., C.D. Condit, R.A. West, B.M. Hermann and T.J. Kreidler. Martian Planetwide Crater Distributions: Implications for Geologic History and Surface Processes. Icarus, Vol. 22, 1974, pp. 239-263.

86. Stettler, A., P. Eberhardt, J. Geiss, N. Grögler and P. Maurer. ^{39}Ar-^{40}Ar Ages and ^{37}Ar-^{38}Ar Exposure Ages of Lunar Rocks. Proc. Lunar Sci. Conf. 4th, 1973, pp. 1865 - 1888.

87. Stoffler, D., D.E. Gault, J. Wedekind and G. Polkowski. Experimental Hypervelocity Impact into Quartz Sand. Distribution and Shock Metamorphism of Ejecta. J. Geophys. Res. 1975, Vol. 80, pp. 4062-4077.

88. Strom, R.G. and G. Fielder. Multiphase Development of the Lunar Crater Tycho. Nature, Vol. 217, 1968, pp. 611 - 615.

89. Tera, F., D.A. Papanastassiou and G.J. Wasserburg. Isotopic Evidence for a Terminal Lunar Cataclysm. Earth Planet. Sci. Lett., Vol. 22, 1974, pp. 1-21.

90. Trask, N.W. Size and Spatial Distribution of Craters Estimated from Ranger Photographs. Jet Propuls. Lab. Tech. Rep. 32-800, Pasadena, California, 1966, pp. 252 - 262.

91. Turner, G. 40Ar-39Ar Ages from the Lunar Maria. Earth Planet. Sci. Lett. Vol. 11, 1971, pp. 169 - 191.

92. Urey, H.C. The Planets. Yale University Press, New Haven, 1952.

93. Wetherill, G.W. Where do the Meteorites Come From? A Re-Evaluation of the Earth-Crossing Apollo Objects as Sources of Chondritic Meteorites. Geochim. Cosmochim. Cosmochim. Acta, Vol. 40, 1976, pp. 1297 - 1317.

94. Wilhelms, D.E. and J.F. McCauley. U.S. Geol. Survey Misc. Geol. Inv. Maps I-703, 1971.

95. Wolfe, E.W., B.K. Lucchitta, V.S. Reed, G.E. Ulrich and A.G. Sanchez. Geology of the Taurus-Littrow Valley Floor. Proc. Lunar Sci. Conf. 6th, 1975, pp. 2463-2482.

VIII. APPENDIX

The tables of measurement data are arranged according to the goal of the investigation. They are always assembled according to the same scheme. This is explained below:

Scheme of the Table

α			
β		γ	
δ		ε	
ζ	η	ϑ	
.	.	.	
.	.	.	
.	.	.	
.	.	.	
.	.	.	
.	.	.	
.	.	.	
.	.	.	

Explanation:*

- α Measurement region (particle type examined)
- β Terrain type (enlargement used)
- γ Picture number (n)** (target number)
- δ Total number of measured craters (impact structures)
- ε Surface [km^2] ([cm^2]()
- ζ Diameter [km] ([mm])
- η N(D) = number of craters (impact structures) of diameters $\geq$ D / surface.
- ϑ ΔN = error in N, which results from the statistic variation

---

* The designations in parenthesis are for the experimental data.

** Both picture numbers are cited for stereoscopic measurements.

- Expansion of the size distribution curve of primary impact craters on the Moon

Mare Serenitatis, Sulpicius Gallus- Region
Mare plain
AS 17-807/808
37
347

0.40	$1.07 \cdot 10^{-1}$	$1.76 \cdot 10^{-2}$
0.45	$6.64 \cdot 10^{-2}$	1.38
0.50	4.04	1.08
0.60	2.89	$9.13 \cdot 10^{-3}$
0.70	1.15	5.77
0.80	$5.77 \cdot 10^{-3}$	4.08
0.90	2.89	2.89

Mare region west of Delisle (total surface)
Mare plain
AS 15-2332/2333
29
117

0.25	$2.48 \cdot 10^{-1}$	$4.60 \cdot 10^{-2}$
0.30	1.28	3.31
0.35	$4.27 \cdot 10^{-2}$	1.91
0.45	2.56	1.48
0.50	1.71	1.21
0.60	$8.54 \cdot 10^{-3}$	$8.54 \cdot 10^{-3}$

Mare region west of Delisle (Eastern portion)
Mare plain
AS 15-2332/2333
20
18

0.17	$1.10 \cdot 10^{0}$	$2.45 \cdot 10^{-1}$
0.20	$6.03 \cdot 10^{-1}$	1.87
0.25	3.84	1.45
0.30	1.65	$9.50 \cdot 10^{-2}$

Investigation and dating of younger impact structures on the Moon.

Crater Copernicus
Continuous ejecta blanket
LO IV 121H2
22
8534

0.80	$2.58 \cdot 10^{-3}$	$5.50 \cdot 10^{-4}$
0.90	1.99	4.83
1.00	1.17	3.71
1.20	$8.20 \cdot 10^{-4}$	3.10
1.30	4.69	2.34
1.60	3.52	2.03
2.40	2.34	1.66
2.60	1.17	1.17

Crater Copernicus
Discontinuous ejecta cover
LO V 142H
LO V 143M
LO V 144M
18
846

0.45	$2.13 \cdot 10^{-2}$	$5.07 \cdot 10^{-3}$
0.50	1.66	4.43
0.60	1.06	3.55
0.80	$4.73 \cdot 10^{-3}$	2.37
0.90	2.37	1.67
1.10	1.18	1.18

Crater Copernicus
Crater base

3σ		LO V 150M 1891
0.5σ	$1.59 \cdot 10^{-2}$	$2.9\sigma \cdot 10^{-3}$
0.6σ	$9.52 \cdot 10^{-3}$	2.24
0.7σ	4.76	1.59
0.8σ	2.12	1.06
0.9σ	1.59	$9.16 \cdot 10^{-4}$
1.1σ	$5.29 \cdot 10^{-4}$	5.29

Crater Copernicus
Secondary crater cluster region

5		LO V 137M 94
0.35	$5.33 \cdot 10^{-2}$	$2.38 \cdot 10^{-2}$
0.45	4.26	2.13
0.5σ	3.2σ	1.85
0.7σ	2.13	1.51
1.00	1.07	1.07

Crater Copernicus
Secondary crater cluster region

16		LO V 137H2 6
0.12	$2.71 \cdot 10^{0}$	$6.78 \cdot 10^{-1}$
0.13	2.54	6.56
0.14	2.2σ	6.11
0.15	1.69	5.36
0.17	1.02	4.15
0.2σ	$3.39 \cdot 10^{-1}$	2.4σ

Crater Kepler
Ejecta cover

25		LO IV 138H1 LO IV 138H2 2008
0.45	$1.24 \cdot 10^{-2}$	$2.49 \cdot 10^{-3}$
0.5σ	1.05	2.28
0.6σ	$4.48 \cdot 10^{-3}$	1.49
0.7σ	3.98	1.41
0.8σ	2.99	1.22
0.9σ	1.49	$8.63 \cdot 10^{-4}$
1.00	$4.98 \cdot 10^{-4}$	4.98

Crater Aristarchus
Continuous ejecta cover

15		LO V 196H3 16
0.08	$9.5\sigma \cdot 10^{-1}$	$2.45 \cdot 10^{-1}$
0.09	6.97	2.1σ
0.1σ	5.07	1.79
0.11	3.8σ	1.55
0.12	2.53	1.27
0.13	1.9σ	1.1σ
0.15	1.27	$8.96 \cdot 10^{-2}$

C-2

Crater | Aristarchus
Continuous ejecta cover |

LO V 198M
LO V 201M
LO V 202M

148		1559
0.17	$9.49 \cdot 10^{-2}$	$7.80 \cdot 10^{-3}$
0.20	5.64	6.02
0.25	2.57	4.06
0.30	1.35	2.94
0.35	$6.41 \cdot 10^{-3}$	2.03
0.40	3.85	1.57
0.45	2.57	1.28
0.50	1.92	1.11
0.70	6.41	6.41

Crater | Aristarchus
Continuous ejecta cover |

LO V 201H2

79		9
0.040	$8.78 \cdot 10^{0}$	$9.87 \cdot 10^{-1}$
0.045	6.33	8.39
0.050	5.33	7.70
0.060	3.00	5.77
0.070	2.00	4.71
0.080	1.67	4.30
0.090	$6.66 \cdot 10^{-1}$	2.72
0.100	4.44	2.22
0.140	1.11	1.11

ORIGINAL PAGE IS
OF POOR QUALITY

Crater Aristarchus
Crater base

LO.V 197M
LO V 200M

5		185
0.20	$2.71 \cdot 10^{-2}$	$1.21 \cdot 10^{-2}$
0.25	2.17	1.08
0.30	1.62	$9.38 \cdot 10^{-3}$
0.45	1.08	7.66
0.60	$5.41 \cdot 10^{-3}$	5.41

Crater Aristarchus
Crater base

LO V 198H2
LO V 199H2

5		54
0.14	$9.19 \cdot 10^{-2}$	$4.11 \cdot 10^{-2}$
0.17	7.35	3.67
0.25	3.67	2 60
0 50	1.84	1.84

Crater Tycho
Continuous ejecta cover

LO V 125M
LO V 128H1
LO V 128H2

26		922
0.20	$2.82 \cdot 10^{-2}$	$5.53 \cdot 10^{-3}$
0 25	1.19	3.60
0.30	$8 67 \cdot 10^{-3}$	3.07
0.35	2.17	1.53
0.60	1.08	1.08

Crater / Tycho

Continuous ejecta cover / LO V 128H1

44 24

0.06	$1.81 \cdot 10^{0}$	$2.72 \cdot 10^{-1}$
0.07	1.27	2.29
0.08	6.16	1.59
0.09	4.11	1.30
0.10	3.29	1.16
0.11	2.88	1.09
0.12	2.46	1.01
0.13	1.64	$8.22 \cdot 10^{-2}$
0.25	$4.11 \cdot 10^{-2}$	4.11

Crater / Tycho

Discontinuous ejecta cover LO IV 112H2

6 19272

0.50	$3.11 \cdot 10^{-4}$	$1.27 \cdot 10^{-4}$
0.70	2.59	1.16
1.10	1.56	$8.99 \cdot 10^{-5}$
1.70	$1.04 \cdot 10^{-5}$	1.04

Crater / Tycho

Crater base / LO V 125M

3 1251

0.30	$3.75 \cdot 10^{-3}$	$2.16 \cdot 10^{-3}$
0.40	2.50	1.77
1.40	1.25	1.25

Crater / North Ray

Ejecta cover P16- 4558
P16- 4563

49 2

0.020	$2.58 \cdot 10^{1}$	$3.69 \cdot 10^{0}$
0.025	1.53	2.84
0.030	1.00	2.30
0.035	$6.33 \cdot 10^{0}$	1.83
0.040	3.16	1.29
0.090	$5.27 \cdot 10^{-1}$	$5.27 \cdot 10^{-1}$

Structures in the Taurus Littrow valley at the Apollo 17 landing site, light Mantle and Central Cluster region. / P17- 2313
P17- 2309

118 6

0.025	$1.85 \cdot 10^{1}$	$1.70 \cdot 10^{0}$
0.030	1.28	1.42
0.035	$6.10 \cdot 10^{0}$	$9.77 \cdot 10^{-1}$
0.040	4.07	7.97
0.045	3.13	6.99
0.050	2.81	6.63
0.060	1.41	4.69
0.070	$9.38 \cdot 10^{-1}$	3.83
0.080	6.26	3.13
0.100	3.13	2.21
0.110	1.56	1.56

ORIGINAL PAGE IS OF POOR QUALITY

Contamination of primary crater population by secondary craters

Crater Aristarchus
Continuous ejecta cover

		LO V 201M LO V 202M
107		1000
0.20	$1.07 \cdot 10^{-1}$	$1.03 \cdot 10^{-2}$
0.25	$4.10 \cdot 10^{-2}$	$6.40 \cdot 10^{-3}$
0.30	2.10	4.58
0.35	1.40	3.74
0.40	$5.00 \cdot 10^{-3}$	2.24
0.45	3.00	1.73
0.50	2.00	1.41
0.70	1.00	1.00

Crater Aristarchus
Crater wall/ejecta cover

		LO V 201H2
57		9
0.045	$6.33 \cdot 10^{0}$	$8.38 \cdot 10^{-1}$
0.050	5.33	7.70
0.060	3.00	5.77
0.070	2.00	4.71
0.080	1.67	4.30
0.090	$6.66 \cdot 10^{-1}$	2.72
0.100	4.44	2.22
0.140	1.11	1.11

Crater Aristarchus
Crater wall

		LO V 197H2
122		9
0.040	$1.39 \cdot 10^{+1}$	$1.26 \cdot 10^{0}$
0.045	$9.47 \cdot 10^{0}$	1.04
0.050	7.31	$9.13 \cdot 10^{-1}$
0.060	3.54	6.36
0.070	1.71	4.42
0.080	1.03	3.42
0.100	$5.71 \cdot 10^{-1}$	2.55
0.110	2.28	1.61
0.140	1.14	1.14

Crater Copernicus
Crater base

		LO V 150H
76		1891
0.40	$4.02 \cdot 10^{-2}$	$4.61 \cdot 10^{-3}$
0.45	2.80	3.85
0.50	2.17	3.39
0.60	1.22	2.54
0.70	$6.86 \cdot 10^{-3}$	1.91
0.80	2.64	1.18
0.90	2.12	1.06
1.10	$5.29 \cdot 10^{-4}$	$5.29 \cdot 10^{-4}$

ORIGINAL PAGE IS
OF POOR QUALITY

Oceanus Procellarum

Mare region		AS16- 2992 AS16- 2993
78		86
o.2o	$8.98 \cdot 1o^{-1}$	$1.o2 \cdot 1o^{-1}$
o.25	4.49	$7.19 \cdot 1o^{-2}$
o.3o	1.73	4.46
o.35	$8.o6 \cdot 1o^{-2}$	3.o5
o.4o	4.61	2.3o
o.45	3.46	1.99
o.5o	1.15	1.15

Aristarchus

Secondary crater chain		AS17- 2931 AS17- 2932
5o		33
o.35	$1.5o \cdot 1o^{o}$	$2.12 \cdot 1o^{-1}$
o.4o	1.23	1.92
o.45	$9.o1 \cdot 1o^{-1}$	1.65
o.5o	7.51	1.5o
o.6o	3.9o	1.o8
o.7o	$9.o1 \cdot 1o^{-2}$	$5.2o \cdot 1o^{-2}$
o.8o	6.o1	4.25

Aristarchus

Secondary crater chain (9-1o)		AS17- 293o AS17- 2931
53		37
o.3o	$1.45 \cdot 1o^{o}$	$1.99 \cdot 1o^{-1}$
o.35	$8.47 \cdot 1o^{-1}$	1.52
o.4o	5.47	1.22
o.45	4.65	1.13
o.5o	3.28	$9.47 \cdot 1o^{-2}$
o.6o	2.19	7.73
o.7o	1.37	6.11
o.8o	$5.47 \cdot 1o^{-2}$	3.86

ORIGINAL PAGE IS OF POOR QUALITY

Aristarchus
Secondary crater chain (10-11)

AS17- 293o
AS17- 2931

36		7o
o.35	$5.13 \cdot 10^{-1}$	$8.56 \cdot 10^{-2}$
o.4o	4.42	7.94
o.45	3.28	6.84
o.5o	2.85	6.38
o.6o	1.57	4.73
o.7o	$9.98 \cdot 10^{-2}$	3.77
o.8o	8.56	3.49
o.9o	4.28	2.47
1.oo	2.85	2.o2

Aristarchus
Secondary crater chain (11-12)

AS17- 293o
AS17- 2931

57		65
o.3o	$8.76 \cdot 10^{-1}$	$1.16 \cdot 10^{-1}$
o.35	6.6o	1.o1
o.4o	4.3o	$8.13 \cdot 10^{-2}$
o.45	2.92	6.7o
o.5o	2.76	6.52
o.6o	2.oo	5.54
o.7o	1.38	4.61
o.8o	1.o8	4.o6
o.9o	$4.61 \cdot 10^{-2}$	2.66
1.oo	3.o7	2.17

Aristarchus
Secondary crater chain (12-13)

AS17- 293o
AS17- 2931

95		77
o.17	$1.24 \cdot 10^{0}$	$1.27 \cdot 10^{-1}$
o.2o	$7.94 \cdot 10^{-1}$	1.o2
o.25	4.16	$7.36 \cdot 10^{-2}$
o.3o	2.21	5.36
o.35	1.17	3.9o
o.45	$3.9o \quad 10^{-2}$	2.25
o.5o	1.3o	1.3o

Aristarchus
Secondary crater chain (13-14)

AS17- 293o
AS17- 2931

56		6o
o.25	$9.32 \cdot 10^{-1}$	$1.25 \cdot 10^{-1}$
o.36	7.49	1.12
o.35	4.33	$8.49 \cdot 10^{-2}$
o.4o	3.5o	7.63
o.45	2.66	6.66
o.5o	1.5o	4.99
o.6o	$8.32 \cdot 10^{-2}$	3.72
o.7o	3.33	2.35
o.9o	1.66	1.66

ORIGINAL PAGE IS
OF POOR QUALITY

Aristarchus
Secondary crater chain (A)

		LO V 195M LO V 196M
26		3o
o.35	$8.81 \cdot 1o^{-1}$	$1.73 \cdot 1o^{-1}$
o.4o	7.45	1.59
o.45	5.o8	1.31
o.5o	4.4o	1.22
o.6o	2.71	$9.58 \cdot 1o^{-2}$
o.7o	2.o3	8.3o
o.9o	1.o2	5.87
1.oo	$3.39 \cdot 1o^{-2}$	3.39

Aristarchus
Secondary crater chain (B)

		LO V 195M LO V 196M
22		19
o.3o	$1.15 \cdot 1o^{o}$	$2.45 \cdot 1o^{-1}$
o.35	1.1o	2.39
o.4o	$7.31 \cdot 1o^{-1}$	1.95
o.45	5.75	1.73
o.5o	4.7o	1.57
o.6o	2.61	1.17
o.7o	1.57	$9.o5 \cdot 1o^{-2}$

Aristarchus
Secondary crater chain

		AS15- 1698 AS15- 1699
19		8
o.3o	$2.27 \cdot 1o^{o}$	$5.2o \cdot 1o^{-1}$
o.35	1.67	4.46
o.4o	1.o7	3.58
o.45	$8.35 \cdot 1o^{-1}$	3.16
o.5o	7.16	2.92
o.6o	3.58	2.o7
o.7o	2.39	1.69
o.9o	1.19	1.19

Kepler
Secondary crater chain

		AS15- 2489 AS15- 249o
7		2o
o.6o	$3.44 \cdot 1o^{-1}$	$1.3o \cdot 1o^{-1}$
o.7o	2.95	1.2o
o.9o	1.97	$9.83 \cdot 1o^{-2}$
1.1o	1.47	8.51
1.2o	$9.83 \cdot 1o^{-2}$	6.95
1.3o	4.91	4.91

ORIGINAL PAGE IS
OF POOR QUALITY

Copernicus
Secondary crater (A) chain
1o

AS15- 1698
AS15- 1699
1oo

0.9o	$9.98 \cdot 1o^{-2}$	$3.16 \cdot 1o^{-2}$
1.1o	8.99	3.oo
1.3o	7.99	2.82
1.4o	5.99	2.45
1.5o	3.99	2.oo
2.oo	2.oo	1.41
3.oo	$9.98 \cdot 1o^{-3}$	$9.98 \cdot 1o^{-3}$

Copernicus
Secondary crater (A) chain
14

LO IV 126H2
91

o.8o	$1.53 \cdot 1o^{-1}$	$4.1o \cdot 1o^{-2}$
o.9o	1.42	3.95
1.oo	1.2o	3.63
1.1o	1.1o	3.46
1.2o	$9.86 \cdot 1o^{-2}$	3.29
1.3o	8.76	3.1o
1.4o	7.67	2.9o
1.5o	5.48	2.45
1.7o	1.1o	1.1o

Copernicus
Secondary crater chain
32

LO IV 121H2
389

1.oo	$8.23 \cdot 1o^{-2}$	$1.46 \cdot 1o^{-2}$
1.1o	7.72	1.41
1.2o	6.94	1.34
1.3o	6.43	1.29
1.4o	5.4o	1.18
1.5o	4.63	1.o9
1.7o	3.34	$9.27 \cdot 1o^{-3}$
2.oo	2.31	7.72
2.5o	1.o3	5.14
3.5o	$2.57 \cdot 1o^{-3}$	2.57

Copernicus
Secondary crater (B) chain
77

AS15- 1698
AS15- 1699
133

o.35	$5.78 \cdot 1o^{-1}$	$6.59 \cdot 1o^{-2}$
o.4o	4.96	6.1o
o.45	4.28	5.67
o.5o	3.o8	4.81
o.6o	1.65	3.52
o.7o	1.o5	2.81
o.8o	$4.51 \cdot 1o^{-2}$	1.84
o.9o	1.5o	1.o6
1.4o	$7.51 \cdot 1o^{-3}$	$7.51 \cdot 1o^{-3}$

ORIGINAL PAGE IS
OF POOR QUALITY

Copernicus

Secondary crater/chain /		AS17- 2289 AS17- 2291
53		36o
o.7o	$1.47 \cdot 1o^{-1}$	$2.o2 \cdot 1o^{-2}$
o.8o	1.28	1.89
o.9o	1.o3	1.69
1.oo	$7.51 \cdot 1o^{-2}$	1.44
1.1o	5.56	1.24
1.2o	4.17	1.o8
1.3o	3.o6	$9.22 \cdot 1o^{-3}$
1.4o	2.78	8.79
1.5o	2.22	7.86
1.7o	1.39	6.22
2.oo	1.11	5.56

Copernicus

Secondary crater (B) chain /		LO IV 126H2
13		72
o.9o	$1.81 \cdot 1o^{-1}$	$5.o3 \cdot 1o^{-2}$
1.1o	1.53	4.63
1.2o	1.4o	4.41
1.3o	1.26	4.19
1.4o	1.12	3.95
1.7o	$9.77 \cdot 1o^{-2}$	3.69
2.oo	6.98	3.12
2.5o	1.4o	1.4o

Aristarchus

/Secondary crater cluster		AS17- 293o AS17- 2931
16		13
o.35	$1.25 \cdot 1o^{o}$	$3.12 \cdot 1o^{-1}$
o.45	$9.35 \cdot 1o^{-1}$	2.7o
o.5o	7.79	2.46
o.6o	5.45	2.o6
o.7o	3.12	1.56
o.8o	2.34	1.35
o.9o	$7.79 \cdot 1o^{-2}$	$7.79 \cdot 1o^{-2}$

Copernicus

/ Secondary crater cluster (A)		LO V 142M
41		161
o.35	$2.55 \cdot 1o^{-1}$	$3.99 \cdot 1o^{-2}$
o.4o	2.18	3.68
o.45	1.81	3.35
o.5o	1.43	2.99
o.6o	$7.47 \cdot 1o^{-2}$	2.16
o.7o	6.23	1.97
o.8o	3.74	1.52
o.9o	3.11	1.39
1.2o	2.49	1.25
1.4o	1.25	$8.8o \cdot 1o^{-3}$
1.5o	$6.23 \cdot 1o^{-3}$	6.23

ORIGINAL PAGE IS
OF POOR QUALITY

Copernicus
Secondary crater (B) LO V 142H
8 cluster 37

0.6o	$2.17 \cdot 1o^{-1}$	$7.68 \cdot 1o^{-2}$
0.7o	1.36	6.o7
0.8o	1.o9	5.43
1.oo	$5.43 \cdot 1o^{-2}$	3.84
1.1o	2.71	2.71

Copernicus
Secondary crater (A) LO V 157M
162 cluster 168

0.25	$9.63 \cdot 1o^{-1}$	$7.57 \cdot 1o^{-2}$
0.3o	5.89	5.92
0.35	4.o4	4.9o
0.4o	2.85	4.12
0.45	2.26	3.67
0.5o	1.72	3.2o
0.6o	1.19	2.66
0.7o	5.95	1.88
0.8o	2.38	1.19
0.9o	1.78	1.o3
1.oo	1.19	$8.41 \cdot 1o^{-3}$
1.1o	$5.95 \cdot 1o^{-3}$	5.95

ORIGINAL PAGE IS OF POOR QUALITY

Copernicus
Secondary crater (B) LO V 157M
92 cluster 99

0.2o	$9.34 \cdot 1o^{-1}$	$9.74 \cdot 1o^{-2}$
0.25	6.29	7.99
0.3o	3.65	6.o9
0.35	2.33	4.87
0.4o	2.o3	4.54
0.5o	1.52	3.93
0.6o	$9.14 \cdot 1o^{-2}$	3.o5
0.7o	5.o8	2.27
0.8o	2.o3	1.44

Copernicus
Secondary crater (C) LO V 157M
3o cluster 24

0.25	$1.24 \cdot 1o^{0}$	$2.27 \cdot 1o^{-1}$
0.3o	$9.12 \cdot 1o^{-1}$	1.95
0.35	6.64	1.66
0.4o	6.22	1.61
0.45	5.39	1.5o
0.5o	4.98	1.44
0.6o	2.9o	1.1o
0.7o	1.24	$7.18 \cdot 1o^{-2}$
0.8o	$8.29 \cdot 1o^{-2}$	5.87

Investigation of experimentally produced secondary particles

Type I

100		T 18
18		1.85
60	$9.37 \cdot 10^{0}$	$2.29 \cdot 10^{0}$
70	7.03	1.95
80	3.24	1.32
90	2.70	1.21
110	1.08	$7.64 \cdot 10^{-1}$
130	$5.41 \cdot 10^{-1}$	5.41

Type I

2000		T 18
48		0.05
4.5	$1.05 \cdot 10^{3}$	$1.52 \cdot 10^{2}$
5.0	$8.54 \cdot 10^{2}$	1.37
6.0	7.44	1.28
7.0	5.69	1.12
8.0	4.60	1.00
9.0	3.94	$9.29 \cdot 10^{1}$
10.0	3.50	8.76
12.0	2.85	7.89
13.0	1.75	6.19
14.0	1.53	5.79
15.0	1.31	5.36
17.0	1.09	4.90
20.0	$8.76 \cdot 10^{1}$	4.38
25.0	6.57	3.79
35.0	2.19	2.19

ORIGINAL PAGE IS
OF POOR QUALITY

Type II

100		T 18
36		1.85
20	$1.95 \cdot 10^{1}$	$3.24 \cdot 10^{0}$
25	1.68	3.01
30	$7.57 \cdot 10^{0}$	2.02
35	5.41	1.71
40	2.16	1.08
50	1.08	$7.64 \cdot 10^{-1}$
60	$5.41 \cdot 10^{-1}$	5.41

Type II

2000		T 18
126		0.05
3.0	$2.76 \cdot 10^{3}$	$2.46 \cdot 10^{2}$
3.5	1.95	2.07
4.0	1.20	1.62
4.5	$8.76 \cdot 10^{2}$	1.38
5.0	5.69	1.12
6.0	2.19	$6.92 \cdot 10^{1}$
7.0	1.53	5.79
8.0	$4.38 \cdot 10^{1}$	3.10
20.0	2.19	2.19

Type III

2000		T 18
2		0.05
0.5	$4.38 \cdot 10^{1}$	$3.10 \cdot 10^{1}$
0.9	2.19	2.19

Type I

100		T 19
17		2.67
60	$6.37 \cdot 10^{0}$	$1.54 \cdot 10^{0}$
70	3.00	1.06
80	2.62	$9.91 \cdot 10^{-1}$
90	1.50	7.49
110	1.12	6.49
150	$3.75 \cdot 10^{-1}$	3.75

Type I

2000		T 19
53		0.09
5	$5.62 \cdot 10^{2}$	$7.72 \cdot 10^{1}$
6	3.92	6.45
7	3.39	6.00
8	2.44	5.09
9	1.70	4.24
10	1.48	3.97
12	1.17	3.52
14	1.06	3.35
15	$9.54 \cdot 10^{1}$	3.18
17	5.30	2.37
25	4.24	2.12
30	3.18	1.84
35	2.12	1.50
60	1.06	1.06

ORIGINAL PAGE IS
OF POOR QUALITY

Type II

100		T 19
24		2.67
20	$8.99 \cdot 10^{0}$	$1.83 \cdot 10^{0}$
25	8.24	1.76
30	5.62	1.45
35	2.62	$9.91 \cdot 10^{-1}$
40	1.50	7.49
60	$3.75 \cdot 10^{-1}$	3.75

Type II

2000		T 19
361		0.09
3.0	$3.83 \cdot 10^{3}$	$2.61 \cdot 10^{1}$
3.5	2.26	1.55
4.0	1.33	1.19
4.5	$8.17 \cdot 10^{2}$	$9.31 \cdot 10^{0}$
5.0	5.73	7.79
6.0	3.08	5.71
7.0	1.59	4.11
8.0	1.38	3.82
10.0	$7.42 \cdot 10^{1}$	2.81
12.0	5.30	2.37
15.0	4.24	2.12
17.0	3.18	1.84
20.0	1.06	1.06

Type III

100		T 19
1		2.67
6	$3.75 \cdot 10^{-1}$	$3.75 \cdot 10^{-1}$

Type III

2000		T 19
8		0.09
0.5	$8.48 \cdot 10^{1}$	$3.00 \cdot 10^{1}$
0.6	6.36	2.60
0.8	5.30	2.37
1.3	4.24	2.12
1.4	3.18	1.84
3.0	2.12	1.50
5.0	1.06	1.06

Type I

100		T 20
20		2.74
60	$7.30 \cdot 10^{0}$	$1.63 \cdot 10^{0}$
70	5.11	1.37
80	3.65	1.15
100	2.55	9.66
110	2.19	$8.94 \cdot 10^{-1}$
120	1.82	8.16
130	1.46	7.30
150	1.09	6.32
250	$7.30 \cdot 10^{-1}$	5.16
350	3.65	3.65

ORIGINAL PAGE IS
OF POOR QUALITY

Type I

2000		T 20
73		0.15
5	$5.01 \cdot 10^{2}$	$5.86 \cdot 10^{1}$
6	3.77	5.09
7	3.16	4.65
8	2.61	4.23
9	2.26	3.94
10	1.99	3.69
11	1.65	3.36
12	1.44	3.14
13	1.23	2.91
15	1.17	2.83
17	1.03	2.66
20	$9.60 \cdot 10^{1}$	2.57
25	6.86	2.17
30	6.17	2.06
35	4.12	1.68
45	3.43	1.53
50	2.74	1.37
70	2.06	1.18
90	1.37	$9.70 \cdot 10^{0}$
300	$6.86 \cdot 10^{0}$	6.86

Type II

100		T 20
16		2.74
25	$5.84 \cdot 10^{0}$	2.30
30	2.92	1.63
40	1.82	$8.16 \cdot 10^{-1}$
50	1.46	7.30
80	1.09	6.32
90	7.30^{-}	5.16
250	3.65	3.65

Type II

2000		T 20
198		0.15
3.0	$1.36 \cdot 10^{3}$	$9.65 \cdot 10^{1}$
3.5	$7.41 \cdot 10^{2}$	7.13
4.0	4.80	5.74
4.5	3.43	4.85
5.0	2.67	4.28
6.0	1.10	2.74
7.0	$4.12 \cdot 10^{1}$	1.68
8.0	2.74	1.37
10.0	2.06	1.19
17.0	1.37	$9.70 \cdot 10^{0}$
20.0	$6.86 \cdot 10^{0}$	6.86

Type III

100		T 20
3		2.74
6	$1.09 \cdot 10^{0}$	$6.32 \cdot 10^{-1}$
8	$7.30 \cdot 10^{-1}$	5.16

Type III

2000		T 20
12		0.15
1.2	$8.23 \cdot 10^{1}$	$2.38 \cdot 10^{1}$
1.3	7.54	2.27
1.5	6.86	2.17
1.7	6.17	2.06
2.0	4.12	1.68
3.0	3.43	1.53
3.5	2.74	1.37
4.5	2.06	1.19
5.0	1.37	$9.70 \cdot 10^{0}$

Type I

2000		T 21
110		0.08
5	$1.31 \cdot 10^{3}$	$1.25 \cdot 10^{2}$
6	1.13	1.16
7	$9.52 \cdot 10^{2}$	1.06
8	8.10	$9.82 \cdot 10^{1}$
9	7.02	9.14
10	6.07	8.50
11	5.12	7.81
12	4.52	7.34
13	3.45	6.41
14	3.33	6.30
15	3.21	6.19
17	2.50	5.46
20	2.14	5.05
25	1.90	4.76
30	1.19	3.76
40	8.33	3.15
45	5.95	2.66
50	4.76	2.38
60	2.38	1.68
80	1.19	1.19

Type I

1oo		T 21
143		3.18
6o	$4.5o \cdot 1o^{1}$	$3.76 \cdot 1o^{o}$
7o	3.55	3.34
8o	1.89	2.44
1oo	1.67	2.29
11o	1.o7	1.83
12o	$9.43 \cdot 1o^{o}$	1.72
13o	5.35	1.3o
15o	4.72	1.22
17o	3.77	1.o9
2oo	2.52	$8.89 \cdot 1o^{-1}$
25o	1.57	7.o3
3oo	1.26	6.29
5oo	$9.43 \cdot 1o^{-1}$	5.45
7oo	3.14	3.14

Type II

1oo		T 21
276		3.18
4o	$8.68 \cdot 1o^{1}$	$5.22 \cdot 1o^{o}$
45	7.48	4.85
5o	6.82	4.61
6o	5.31	4.o9
7o	4.21	3.64
8o	3.58	3.36
9o	3.24	3.19
1oo	2.67	2.9o
11o	2.48	2.8o
12o	2.o8	2.55
14o	1.45	2.13
15o	1.38	2.o9
17o	1.1o	1.86
2oo	$8.81 \cdot 1o^{o}$	1.66
25o	5.97	1.37
3oo	4.4o	1.18
35o	2.83	$9.43 \cdot 1o^{-1}$
4oo	2.2o	8.32
45o	1.57	7.o3
5oo	$9.43 \cdot 1o^{-1}$	5.45
7oo	6.29	4.45

ORIGINAL PAGE IS
OF POOR QUALITY

Type II

500		T 21
22		0.05
17	$3.55 \cdot 10^{2}$	$5.35 \cdot 10^{1}$
20	3.07	4.97
25	2.66	4.63
30	1.94	3.95
335	1.45	3.42
40	1.29	3.23
50	$8.07 \cdot 10^{1}$	2.55
60	4.84	1.98
70	4.03	1.80
120	2.42	1.40
150	1.61	1.14
170	2.10	2.10

Type III

100		T 21
48		3.18
6	$1.51 \cdot 10^{1}$	$2.18 \cdot 10^{0}$
8	1.04	1.81
9	$3.77 \cdot 10^{0}$	1.09
10	3.14	$9.94 \cdot 10^{-1}$
12	1.57	7.03
13	$9.43 \cdot 10^{-1}$	5.45
17	6.29	4.45
90	3.14	3.14

ORIGINAL PAGE IS OF POOR QUALITY

Type III

500		T 21
20		0.12
2.0	$1.61 \cdot 10^{2}$	$3.61 \cdot 10^{1}$
2.5	1.13	3.02
3.0	$5.65 \cdot 10^{1}$	2.13
3.5	3.23	1.61
4.0	2.42	1.41
5.0	1.61	1.14
6.0	$8.07 \cdot 10^{0}$	$8.07 \cdot 10^{0}$

Type I

2000		T 22
86		0.02
10	$3.52 \cdot 10^{3}$	$3.80 \cdot 10^{2}$
11	2.95	3.47
12	2.54	3.22
13	2.05	2.90
14	1.68	2.62
15	1.31	2.32
17	1.15	2.17
20	$8.60 \cdot 10^{2}$	1.88
25	4.10	1.29
30	2.87	1.08
45	$8.19 \cdot 10^{1}$	$5.79 \cdot 10^{1}$
70	4.10	4.10

Type II

100		T 22
93		1.65
110	$5.64 \cdot 10^{1}$	$5.84 \cdot 10^{0}$
120	5.03	5.52
140	4.00	4.92
150	3.27	4.45
170	2.48	3.88
200	1.82	3.32
250	1.27	2.78
300	$7.88 \cdot 10^{0}$	2.19
350	6.06	1.92
400	5.45	1.82
450	3.64	1.48
500	3.03	1.36
600	1.82	1.05
900	1.21	$8.57 \cdot 10^{-1}$
1100	$6.06 \cdot 10^{-1}$	6.06

Type III

100		T 22
59		1.65
7	$3.58 \cdot 10^{1}$	$4.66 \cdot 10^{0}$
8	2.97	4.24
9	2.48	3.88
10	2.18	3.64
11	1.88	3.37
12	1.52	3.03
13	1.21	2.71
14	1.03	2.50
15	$8.48 \cdot 10^{0}$	2.27
17	7.27	2.10
20	5.45	1.82
30	3.64	1.48
35	2.42	1.21
40	1.82	1.05
50	1.21	$8.57 \cdot 10^{-1}$

ORIGINAL PAGE IS
OF POOR QUALITY

The work presented here was performed at the Max-Planck Institute for nuclear physics under excellent working conditions. It was supported by a stipendum from the graduate research fund. For this, thanks go to Dr. P. Brix and Dr. U. Schmidt-Rohr as directors of this institute.

The investigations were suggested by Dr. H. Fechtig. I would like to express my thanks to him for his valuable support and help.

Dr. T. Kirsten is due my gratitude for co-editing this report.

Performance of the experiments on the light gas cannon of the Ernst-Mach Institute in Freiburg were made possible by Dr. Reichenbach, Dr. Stilp, Mr. Gotting and Dr. Schneider.

Numerous fruitful discussions were conducted with Dr. Neukum, Dr. Nagel and Dr. W. Kratschmer. Cooperation with my colleagues G. Braun, B. Dalmann, Dr. G. Eichhorn, Dr. E. Grün, Dr. J. Kissel and N. Pailer was excellent.

In the preparation and performance of the experiments I was aided by Mr. H. Hub, Mrs. M. Leistner, Mrs. S. Papp, Mr. G. Schäfer, Miss B. Schray, Mr. B. Schuhrer, Mrs. Seitz-Kruljac, Mrs. V. Traumer, Mr. H. Voth, Mr. H. Weber and Mr. W. Weiss.

I would like to express my sincere gratitude to all these persons at this point. Without their personal involvement the completion of this work in this present form would not have been possible.